

**UNIVERSITY OF KWAZULU-NATAL**



**THE C-BAND ALL SKY SURVEY  
COMMISSIONING AND DATA ANALYSIS**

by

**Heiko Martin Heilgendorff**

Submitted in fulfilment of the academic requirements for the degree of  
Doctor of Philosophy (Science)

in the School of Mathematics, Statistics, and Computer Science,  
University of KwaZulu-Natal

Durban

September, 2017

As the candidate's supervisor I have approved this thesis for submission.

Signed: ..... Name: ..... Date: .....

The financial assistance of the National Research Foundation (NRF) towards this research is hereby acknowledged. Opinions expressed and conclusions arrived at, are those of the author and are not necessarily to be attributed to the NRF.

*For my family.*

# Abstract

The C-Band All Sky Survey (C-BASS) is a ground based radio survey that scans the entire sky in Stokes I, Q and U at a central frequency of 5 GHz with a 1 GHz bandwidth and an angular resolution of  $0.73^\circ$ . The experiment consists of two telescopes, one at Owens Valley Radio Observatory in California and the other at the SKA support base in Klerefontein, South Africa. The primary aim of this experiment is to produce high fidelity maps of the entire sky in Stokes I, Q and U. These maps will be used by CMB experiments for the removal of Galactic foreground radiation, via component separation, and will provide vital aid in the search for the primordial CMB *B*-mode polarized signal. C-BASS also aims to probe the Galactic magnetic field using synchrotron radiation and will search for new areas of anomalous microwave emission.

In this thesis, I present the contribution that I have made to the C-BASS experiment. I contributed to C-BASS instrumentation development by working extensively on the commissioning of the southern telescope; in particular, I developed an optical pointing system and refined the automated analysis process. I contributed to the development of the C-BASS data analysis pipeline for both the northern and southern telescopes, with the development of a new RFI flagging method, work on map making techniques and convergence, and self-consistency tests.

The northern survey is complete and data analysis is at an advanced stage. The southern instrument is undergoing commissioning on site and will soon begin survey operations. My contributions to the project have improved the processed data quality in both surveys and will aid in the successful completion of the southern survey.

# Acknowledgements

The last few years have certainly been a journey of discovery. I have travelled to places I never dreamed I would see and done things I could never have imagined! I would like to thank Cynthia and Jon for your expert guidance, open and friendly advice, and the excellent example you set in pursuing your work with passion and dedication. Thank you for sharing your love of science, whiskey, and great beer! To the rest of the UKZN C-BASS team, Moumita and Johannes, thanks for accompanying me on this journey—it wouldn't have been the same without you.

Oxford will always have a special place in my heart, and all the more so for the time spent with Mike, Angela, Jamie, Richard, Alex, Boon, Jazz, and of course, Luke and Amanda. Thanks for the warm welcome, the invaluable knowledge, the great experiences, and the many evenings spent chatting over a pint.

Charles and Stephen deserve special mention for sharing your expertise with me on site. I am truly indebted to you for your help and guidance early on, and I really enjoyed the time that I spent with you.

Sizwe and your technical team in Klerefontein, thank you for the many hours you have put in for us, sometimes late, sometimes early and sometimes even over the weekend. Every request was met with professionalism and enthusiasm and I know I speak for the entire C-BASS collaboration in thanking you for your invaluable contribution. I would also like to thank the SKA for providing me with the funds, the tools, and the opportunity to conduct my research and to

continue learning.

Finally, and most importantly, I would like to thank my family for your enduring love and support. Dad, you fostered a fascination with science and the stars with all our long talks—long may they continue. Matt and Rich, this is as much your fault as it is his—thanks for your calm reassurance and always standing by me. Jax, you are my everything, and I truly could not have done this without you.

# Preface

The work described in this thesis was carried out in the School of Mathematics, Statistics, and Computer Science, University of KwaZulu-Natal from October 2013 to September 2017. This dissertation was completed under the supervision of Dr H. C. Chiang, with co-supervision by Prof J. L. Sievers.

This study represents original work by the author and has not been submitted in any form for any degree or diploma to any other tertiary institution. Where use was made of the work of others it has been duly acknowledged in the text.

# Declaration of Non-Plagiarism

I, **Heiko Martin Heilgendorff** declare that

1. The research reported in this thesis, except where otherwise indicated, is my original research.
2. This thesis has not been submitted for any degree or examination at any other university.
3. This thesis does not contain other persons' data, pictures, graphs or other information, unless specifically acknowledged as being sourced from other persons.
4. This thesis does not contain other persons' writing, unless specifically acknowledged as being sourced from other researchers. Where other written sources have been quoted, then:
  - (a) Their words have been re-written but the general information attributed to them has been referenced.
  - (b) Where their exact words have been used, then their writing has been placed in italics and inside quotation marks, and referenced.
5. This thesis does not contain text, graphics or tables copied and pasted from the Internet, unless specifically acknowledged, and the source being detailed in the thesis and in the References sections.

Signed in Westville, KwaZulu-Natal: ..... Date: .....

# Contents

|   |           |
|---|-----------|
| <b>Abstract</b>   | <b>i</b>  |
| <b>Acknowledgments</b>                                      | <b>ii</b> |
| <b>Preface</b>  | <b>iv</b> |
| <b>Declaration of Non-Plagiarism</b>                        | <b>v</b>  |
| <b>List of Tables</b>                                       | <b>ix</b> |
| <b>List of Figures</b>                                      | <b>x</b>  |
| <b>1 A Review of Modern Cosmology</b>                       | <b>1</b>  |
| 1.1 A Timeline of the Universe . . . . .                    | 3         |
| 1.2 A Brief Summary of Modern Cosmology . . . . .           | 5         |
| 1.2.1 The Cosmic Microwave Background . . . . .             | 9         |
| 1.2.1.1 CMB Polarization . . . . .                          | 12        |
| 1.2.2 A Brief Summary of Contemporary Experiments . . . . . | 15        |
| 1.3 Galactic Foreground Emission . . . . .                  | 17        |
| 1.3.1 Free-Free Emission . . . . .                          | 18        |
| 1.3.2 Synchrotron Emission . . . . .                        | 19        |
| 1.3.3 Thermal Dust Emission . . . . .                       | 20        |
| 1.3.4 Anomalous Microwave Emission . . . . .                | 21        |

|          |   |           |
|----------|---|-----------|
| 1.3.5    | Point Sources and Confusion Noise . . . . .                           | 22        |
| 1.3.6    | Galactic Foreground Removal Techniques . . . . .                      | 22        |
| 1.4      | Thesis Overview . . . . .   | 23        |
| <b>2</b> | <b>The C-Band All Sky Survey</b>                                      | <b>25</b> |
| 2.1      | The C-Band All Sky Survey . . . . .                                   | 25        |
| 2.1.1    | Science Goals . . . . .   | 28        |
| 2.1.2    | Survey Requirements . . . . .   | 28        |
| 2.2      | C-BASS Optics . . . . .   | 32        |
| 2.3      | The C-BASS Receiver . . . . .   | 35        |
| 2.3.1    | Cryogenic Front End . . . . .   | 37        |
| 2.3.2    | Total Intensity and Polarization Measurement . . . . .                | 38        |
| 2.3.2.1  | Continuous Comparison Radiometer . . . . .                            | 39        |
| 2.3.2.2  | Correlation Polarimeter . . . . .                                     | 42        |
| 2.3.3    | Back End Electronics . . . . .  | 42        |
| <b>3</b> | <b>Data Reduction and Low-level Time Stream Processing</b>            | <b>45</b> |
| 3.1      | The Time Stream Processing Pipeline . . . . .                         | 45        |
| 3.1.1    | Complex Gain Correction . . . . .                                     | 47        |
| 3.1.2    | 1.2 Hz Oscillation Removal . . . . .                                  | 47        |
| 3.1.3    | RFI Flagging . . . . .  | 48        |
| 3.1.3.1  | The Effect of the Ground Signal on the RFI Flagging Routine . . . . . | 68        |
| 3.1.4    | Pointing . . . . .  | 70        |
| 3.1.5    | Calibration . . . . .   | 71        |
| 3.1.6    | Time Stream Processing Pipeline Output . . . . .                      | 72        |
| 3.2      | Producing a Final Data Set . . . . .                                  | 72        |
| 3.3      | Future Work . . . . .   | 75        |
| <b>4</b> | <b>Map Making and Data Consistency Tests</b>                          | <b>77</b> |
| 4.1      | Map Making . . . . .  | 77        |

|          |  |            |
|----------|--|------------|
| 4.1.1    | Map Making with Ninkasi . . . . .                        | 79         |
| 4.1.2    | Map Making with DESCART . . . . .                        | 80         |
| 4.1.3    | Convergence Tests . . . . .                              | 82         |
| 4.2      | Data Consistency Tests . . . . .                         | 99         |
| 4.2.1    | Jackknife Results . . . . .                              | 99         |
| 4.2.1.1  | Interleaved Months Test . . . . .                        | 100        |
| 4.2.1.2  | Diurnal Variations Test . . . . .                        | 105        |
| 4.2.1.3  | Signal Chain Test . . . . .                              | 110        |
| 4.2.1.4  | Azimuth Scan Direction Test . . . . .                    | 113        |
| 4.3      | Summary and Conclusions . . . . .                        | 116        |
| <b>5</b> | <b>Commissioning the Southern System</b>                 | <b>117</b> |
| 5.1      | Commissioning the Southern System . . . . .              | 117        |
| 5.1.1    | Commissioning C-BASS South Optics . . . . .              | 121        |
| 5.1.1.1  | Focusing the primary reflector . . . . .                 | 121        |
| 5.1.1.2  | Focusing the secondary reflector . . . . .               | 122        |
| 5.1.2    | Optical Pointing . . . . .                               | 124        |
| 5.1.2.1  | Physical Setup . . . . .                                 | 126        |
| 5.1.2.2  | Optical Pointing Strategy . . . . .                      | 129        |
| 5.1.2.3  | Optical Pointing Data Analysis . . . . .                 | 129        |
| 5.1.3    | Radio Pointing . . . . .                                 | 133        |
| 5.1.4    | The RFI Environment at Klerefontein . . . . .            | 134        |
| 5.1.5    | Investigating RFI Using the C-BASS Signal Band . . . . . | 140        |
| 5.2      | Summary and Conclusions . . . . .                        | 141        |
|          | <b>Bibliography</b>                                      | <b>143</b> |

# List of Tables

|     |   |     |
|-----|---|-----|
| 1.1 | Summary of Planck CMB parameter measurements. . . . .               | 12  |
| 1.2 | Overview of relevant CMB experiments. . . . .                       | 16  |
| 1.3 | Overview of contemporary Galactic foreground radio surveys. . . . . | 17  |
| 2.1 | Summary of northern and southern telescope parameters. . . . .      | 27  |
| 3.1 | Summary of RFI flagging percentages per month . . . . .             | 75  |
| 5.1 | Secondary reflector position settings . . . . .                     | 124 |
| 5.2 | Summary of the most persistent RFI sources . . . . .                | 135 |

# List of Figures

|     |   |    |
|-----|---|----|
| 1.1 | Theoretical CMB angular power spectrum . . . . .  | 11 |
| 1.2 | The quadrupole anisotropy . . . . .   | 13 |
| 1.3 | Polarization arising from scalar, vector, and tensor quadrupolar anisotropies . . . . .                   | 14 |
| 1.4 | Contribution of foreground contaminants as a function of frequency . . . . .                              | 18 |
| 2.1 | Photographs of the C-BASS telescopes on site . . . . .  | 27 |
| 2.2 | Time stream data from a typical Elevation 37 survey schedule . . . . .                                    | 31 |
| 2.3 | Schematics of the different optical configurations employed in the two C-BASS systems . . . . .           | 34 |
| 2.4 | Simplified schematic of the northern receiver . . . . .   | 36 |
| 2.5 | Simplified schematic of the southern receiver . . . . .   | 37 |
| 2.6 | Photographs of the C-BASS cryostat . . . . .  | 38 |
| 2.7 | Examples of a Dicke switch and a continuous-comparison radiometer architecture . . . . .                  | 41 |
| 2.8 | C-BASS south front end digital signal processing . . . . .  | 44 |
| 3.1 | Pipeline flow chart . . . . .   | 46 |
| 3.2 | Comparison between interpolation and nearest pixel method using maps with the same resolution . . . . .   | 50 |
| 3.3 | Comparison between interpolation and nearest pixel method using maps with different resolutions . . . . . | 52 |
| 3.4 | Map used to model the expected sky signal . . . . .   | 53 |

|      |   |    |
|------|---|----|
| 3.5  | Comparison between the expected TOD sky signal and the time ordered data for a typical survey schedule . . . . .                        | 56 |
| 3.6  | Skewness and kurtosis per scan before and after flagging for a typical survey schedule . . . . .  | 57 |
| 3.7  | Comparison between the expected TOD sky signal and the time ordered data for an azimuth scan featuring a large RFI event . . . . .      | 59 |
| 3.8  | Histograms of the residual of the data and the fitted expected sky signal before and after RFI flagging . . . . .                       | 60 |
| 3.9  | Comparison between the expected TOD sky signal and the time ordered data for an azimuth scan featuring a small RFI event . . . . .      | 61 |
| 3.10 | Histograms of the residuals before and after RFI flagging for a scan with a small RFI event. . . . .                                    | 61 |
| 3.11 | Comparison between the expected TOD sky signal and the time ordered data for an azimuth scan featuring a very large RFI event . . . . . | 62 |
| 3.12 | Mollweide projection maps of a single survey schedule before and after RFI flagging . . . . .   | 63 |
| 3.13 | Mollweide projection maps of an entire day before and after RFI flagging . . . .  | 64 |
| 3.14 | Comparison between the new and old RFI flagging routines . . . . .  | 66 |
| 3.15 | Azimuth-Elevation plots with and without RFI flagging . . . . .   | 68 |
| 3.16 | Templates for ground contamination in Stokes I at the different survey elevations.  | 69 |
| 3.17 | Comparison of model fitting with and without accounting for ground contamination  | 70 |
| 3.18 | Percentage of RFI flagged per schedule for the full Elevation 37 data set . . . . .   | 74 |
| 3.19 | Percentage of RFI flagged per schedule for the curated Elevation 37 data set . . .  | 74 |
| 4.1  | Auto spectra for the six month input map and artificial signal in Stokes I. . . . .   | 84 |
| 4.2  | Input maps for the first Ninkasi runs of each series in Stokes I . . . . .  | 85 |
| 4.3  | Input maps for several Ninkasi runs in Stokes I . . . . .   | 87 |
| 4.4  | Auto spectra of the residuals after selected Ninkasi runs and the injected artificial signal in Stokes I . . . . .                      | 90 |

|      |   |     |
|------|---|-----|
| 4.5  | Cross correlation between the residuals and the injected artificial signal in Stokes I  | 91  |
| 4.6  | Auto spectra for the input map and artificial signal in Stokes Q and U. . . . .   | 92  |
| 4.7  | Input maps for the first Ninkasi runs of each series in Stokes Q . . . . .  | 93  |
| 4.8  | Input maps for the first Ninkasi runs of each series in Stokes U . . . . .  | 94  |
| 4.9  | Input maps for several Ninkasi runs of each series in Stokes Q . . . . .  | 95  |
| 4.10 | Input maps for several Ninkasi runs of each series in Stokes U . . . . .  | 96  |
| 4.11 | Auto spectra of the residuals after each run and the injected artificial signal in<br>Stokes Q and U . . . . .  | 97  |
| 4.12 | Square root of the ratio between the auto spectra of the residuals after each run,<br>and the auto spectrum of the injected artificial signal in Stokes Q and U . . . . . | 97  |
| 4.13 | Cross correlation between the residuals and the injected artificial signal in Stokes<br>Q and U . . . . .   | 98  |
| 4.14 | Ratio between the cross correlated signal and the auto spectrum of the injected<br>artificial signal in Stokes Q and U . . . . .  | 98  |
| 4.15 | Ninkasi output maps of the interleaved months jackknife of the full data set for<br>Stokes I, Q and U . . . . .   | 102 |
| 4.16 | Power spectra of the interleaved months jackknife for the full data set in Stokes<br>I, Q and U . . . . .   | 103 |
| 4.17 | Ninkasi output maps of the interleaved months jackknife for data with less than<br>60 % RFI flagged for Stokes I, Q and U . . . . .                                       | 106 |
| 4.18 | Power spectra of the interleaved months jackknife for data with less than 60 %<br>RFI flagged, in Stokes I, Q and U . . . . .   | 107 |
| 4.19 | Ninkasi output maps of the day and night jackknife in Stokes I, Q and U . . . . .   | 108 |
| 4.20 | Power spectra of the day and night jackknife in Stokes I, Q and U . . . . .   | 109 |
| 4.21 | Ninkasi ouput maps of the signal chain jackknife for Stokes I, Q and U . . . . .  | 111 |
| 4.22 | Power spectra of the signal chain jackknife in Stokes I, Q and U . . . . .  | 112 |
| 4.23 | Ninkasi output maps of the scan direction jackknife for Stokes I, Q and U . . . . .   | 114 |
| 4.24 | Power spectra of the scan direction jackknife in Stokes I, Q and U . . . . .  | 115 |

|      |  |     |
|------|--|-----|
| 5.1  | Map of 3G signal coverage in South Africa, showing the location of Klerefontein                            | 118 |
| 5.2  | Commissioning C-BASS South . . . . .   | 119 |
| 5.3  | Receiver test rig . . . . .  | 120 |
| 5.4  | Photograph of the C-BASS dish showing photogrammetry markers . . . . .                                     | 122 |
| 5.5  | Photograph of the C-BASS receiver, mounted on the dish, with part of its covering removed . . . . .        | 123 |
| 5.6  | Beam maps of moon rasters, showing the results of the secondary reflector positional adjustments . . . . . | 125 |
| 5.7  | Protective enclosure and camera mount assembly . . . . .   | 127 |
| 5.8  | Photograph of the remote optical pointing control system. . . . .  | 127 |
| 5.9  | Schematic circuit diagram of the remote optical pointing control system. . . . .                           | 128 |
| 5.10 | Optical pointing FITS images . . . . .   | 131 |
| 5.11 | Example of the final output of the pointing model analysis . . . . .                                       | 133 |
| 5.12 | Fitting the azimuth and elevation position for a radio pointing cross. . . . .                             | 134 |
| 5.13 | Azimuth-Elevation plot of a full sky scan in channel 87 showing 4 ground sources                           | 136 |
| 5.14 | Azimuth-Elevation plot of a full sky scan in channel 87 showing 3 ground sources                           | 136 |
| 5.15 | Google Earth satellite image of the C-BASS site . . . . .  | 137 |
| 5.16 | Azimuth-Elevation plot of a full sky scan in channel 31 . . . . .  | 138 |
| 5.17 | Five consecutive channels highlighting the advantage of spectral resolution . . . . .                      | 139 |
| 5.18 | Average over channels 85 to 89, with and without channel excision . . . . .                                | 140 |
| 5.19 | RFI events detected across all channels in southern data . . . . .   | 141 |
| 5.20 | All sky map from the C-Band All Sky Survey . . . . .   | 142 |

# Chapter 1

## A Review of Modern Cosmology

Humanity has always had a fascination with the stars. For thousands of years, we have gazed at the heavens in wonder, finding a place for the universe—and our place in it—in our mythologies, our religions, and our science. In the early 1500s, Nicolaus Copernicus fundamentally altered our understanding of the universe by observing that the earth was not at its centre, as had been generally believed. Copernicus realised that the earth in fact revolved around the sun, and consequently believed that the sun itself was the centre of the universe. This idea, that our position in space is in no way special, forms the basis of the cosmological principle in which we assume that the universe is both isotropic and homogeneous on large scales. This means that, on large scales, every point in the universe is exactly the same as any other point, and that the universe looks the same in any direction. This idea, though it is also called the Copernican principle, did not develop immediately as a consequence of Copernicus' work. For example, while mapping out the disk structure of the Milky Way galaxy, the Herschels believed the solar system to be at its centre—a belief that remained prevalent until the early 1900s. The cosmological principle, though rooted in Copernicus' work, only came to light in the 1950s when we finally understood that there was absolutely nothing special about the Milky Way, or our place in it, or indeed its place in the universe. It is but one of many thousands of similar galaxies scattered throughout space, with no reason to be special other than the fact that it's the one we call home.

At the turn of the twentieth century, the dominant cosmological theory was that of a static universe, with an infinite number of stars, distributed throughout an infinite space, over an infinite time. This theory remained popular until the late 1920s when advances in telescope design and the discovery of the period-luminosity relationship provided irrefutable evidence that the universe was expanding. In the early 1900s, Henrietta Leavitt, working at the Harvard College Observatory, began looking at the luminosity of Cepheid variables in the Magellanic Clouds. She soon realised that there was a direct relationship between the luminosity and pulsation period of a Cepheid (Leavitt and Pickering, 1912). This discovery of the period-luminosity relationship led to the development of a technique that uses sources of known luminosity, now called standard candles, as distance calibrators.

While it was not known at the time, the universe is anything but static. Galaxies are moving with tremendous velocities and, as the universe is expanding, these galaxies are generally moving away from each other. The cosmological principle is upheld in this scenario as the universe is expanding in every direction and thus galaxies are moving away from each other from every point of view. The velocity, due to cosmological expansion, of a receding galaxy can be measured by its redshift, which is a shift in the frequency of radiation emitted from the galaxy. This frequency shift is the result of photons losing energy as they move through expanding space. The shift is measured as follows:

$$z = \frac{\lambda_{obs} - \lambda_{em}}{\lambda_{em}}, \quad (1.1)$$

where  $\lambda_{obs}$  is the observed frequency, and  $\lambda_{em}$  is the emitted frequency. The velocity of the galaxy can then be determined using the speed of light  $c$  in  $v = zc$ . Vesto Slipher first used this technique to measure the velocity of a galaxy in 1912 and Edwin Hubble combined this technique and the standard candle distance calibrator technique to measure the velocity of galaxies at various distances (Hubble, 1929). He found that there was a roughly linear relation between a galaxy's velocity  $\vec{v}$  and its distance  $\vec{r}$  from the observer. This is the now famous Hubble's law:

$$\vec{v} = H_0 \vec{r}. \quad (1.2)$$

$H_0$  is the Hubble constant, which he estimated at the time to be 500 km/s/Mpc, while modern

estimates are of order 70 km/s/Mpc. This evidence of an expanding universe comprehensively disproved the static universe model and as such, a new cosmological theory was required. The Steady State universe and the Big Bang theory soon emerged as the major contenders for the cosmological crown. The Steady State cosmology adhered to the cosmological principle in an expanding universe by keeping the density of matter constant with the continuous creation of new matter. This theory was popular in the mid 1900s but has generally been abandoned in light of evidence that strongly supports the hot Big Bang model.

Unknown to Hubble, a Belgian priest named Georges Lemaître, guided by Einstein's general theory of relativity (Einstein, 1916), had predicted an expanding universe in 1927, two years before Hubble's discovery. He published his theory in a Belgian journal (Lemaître, 1927) that was not widely circulated outside that country and it was not translated into English until 1931 (Lemaître, 1931a). This work prompted Lemaître to consider that a universe that is expanding in time must have begun with a finite point. In a letter to *Nature* (Lemaître, 1931b), he considered that as the universe expands, the energy, which remains constant, must be discretized into more and more quanta. Conversely, moving backwards in time, the energy would be packaged into fewer and fewer quanta until a single 'unique atom', containing the entire mass of the universe, remained. This theory of a unique singularity providing a beginning for time and space came to be known as the Big Bang theory.

## **1.1 A Timeline of the Universe According to the Expanding Hot Big Bang Cosmology**

In our current understanding of cosmology, the universe was created 13.8 billion years ago in an event called 'the Big Bang' and has been expanding and cooling ever since. During the early years of the universe, the primordial plasma was so highly energised that photons could not escape the photon-baryon fluid. After about 380 000 years of expansion and cooling, the universe entered a period of recombination, where protons, neutrons and electrons eventually were cool

enough to form neutral hydrogen (Zel'dovich et al., 1969). This led to a reduction in the number of free electrons, allowing photons and electrons to decouple and providing us with an image of the surface of last scattering. These ancient photons are known as the cosmic microwave background (CMB) and provide a powerful probe of cosmology. This background radiation was predicted by Ralph Alpher and Robert Herman in 1948 while making a case for the hot Big Bang. They estimated the background thermal radiation, a relic of the enormous temperatures in the early universe, to be 5 K (Alpher and Herman, 1948).

While the CMB had been predicted with remarkable accuracy, its discovery was completely accidental. In 1964, Arno Penzias and Robert Wilson were testing a Dicke radiometer at Bell Telephone Laboratories in New Jersey. Their instrument, meant for radio astronomy and satellite communication, appeared to have a problem as it was picking up a constant background signal consistent with a perfect blackbody measuring 3.5 K, which seemed to be coming from all directions. After exhausting all possible options for the source of this radiation, including pigeon droppings, they finally concluded that this 'excess radiation' was coming from the universe itself (Penzias and Wilson, 1965). At the same time, a team at Princeton University led by Robert Dicke was in the process of attempting to measure the CMB using their own Dicke radiometer (Peebles et al., 2009). After hearing about Penzias and Wilson's discovery, they quickly concluded that Penzias and Wilson had indeed found the signal that they themselves were searching for (Dicke et al., 1965). Penzias and Wilson received the Nobel Prize for the landmark discovery that placed the hot Big Bang cosmological model at the forefront of modern cosmology. The discovery of the CMB spawned a new era in observational cosmology, allowing astronomers to observe the surface of last scattering, a snapshot of the universe as it was when matter and photons decoupled.

The decoupling of photons and matter led to the dark ages, when the universe became transparent. This lasted about 150 million years. Over time, the gravitational collapse of higher density regions of neutral hydrogen began to form ionized structure, igniting the first stars in an era known as the epoch of reionization. The universe continued to develop structure as the high

density regions grew denser, forming stars and galaxies, which in turn formed galaxy clusters and superclusters. This growth of structure is an ongoing process and is a consequence of events that occurred in the immediate aftermath of the Big Bang.

## 1.2 A Brief Summary of Modern Cosmology

At the heart of modern cosmology lies the Friedmann-Lemaître-Robertson-Walker (FLRW) metric, named after the people who independently derived the same model during the 1920s and 30s (Friedmann, 1922). This metric is an exact solution to the Einstein field equations and describes a homogeneous, isotropic, expanding or contracting universe. The FLRW metric is as follows:

$$-c^2 ds^2 = -c^2 dt^2 + a^2(t) \left[ \frac{dr^2}{1 - kr^2} + r^2 (d\theta^2 + \sin^2 \theta d\phi^2) \right], \quad (1.3)$$

where  $k \in \{-1, 0, 1\}$  indicates negative, zero, and positive curvature, and  $a$  is the time-dependent scale factor, which describes the expansion of the universe. The redshift,  $z$ , due to the expansion of the universe can be described in terms of scale factor:

$$1 + z = \frac{a_0}{a(t)}, \quad (1.4)$$

where  $a_0$  is the scale factor of the current epoch, and  $a(t)$  is the scale factor of the time when the photons being measured were emitted. Einstein's field equations and the FLRW metric can be used to derive the first and second Friedmann equations:

$$\left(\frac{\dot{a}}{a}\right)^2 = \frac{8\pi G}{3}\rho - \frac{kc^2}{a^2} + \frac{\Lambda c^2}{3}, \quad (1.5)$$

which describes the expansion of the universe, and:

$$\frac{\ddot{a}}{a} = \frac{1}{3} \left[ \Lambda c^2 - 4\pi G \left( \rho + \frac{3p}{c^2} \right) \right], \quad (1.6)$$

which describes the acceleration of the scale factor. In these equations,  $\Lambda$  represents the cosmological constant,  $p$  is pressure,  $c$  is the speed of light in a vacuum,  $\rho$  is the density of matter plus radiation, and  $G$  is Newton's gravitational constant. These equations describe the interaction of a homogeneous fluid and spacetime curvature and can be applied to the evolution of the universe

on the largest scales. The equation of state for a perfect fluid can be written as  $p = w\rho c^2$ , where  $w$  is some constant. If we assume a flat universe ( $k = 0$ ) and a cosmological constant of zero, we can derive the following equation for the scale factor:

$$a(t) = a_0 t^{\frac{2}{3(w+1)}} \quad (1.7)$$

where  $w = 1/3$  indicates a radiation dominated universe, with the scale factor increasing as  $a(t) \propto t^{1/2}$ , and  $w = 0$  indicates a matter dominated universe, with the scale factor increasing as  $a(t) \propto t^{2/3}$ . This shows that the universe has undergone phase transitions as different energy forms have dominated the evolution of the scale factor.

Current observations suggest that the universe is very close to the critical density required for a flat universe with curvature  $k = 0$ . From the Friedmann equations, the critical density required for a flat universe is

$$\rho_c = \frac{3H^2}{8\pi G}, \quad (1.8)$$

where  $H \equiv \dot{a}/a$  is the Hubble parameter, a measure of the expansion rate of the universe as seen in Equation 1.2. A universe with an energy density greater than the critical energy density would eventually collapse in on itself, while a lower energy density would result in permanent expansion. A universe with critical energy density would remain perfectly balanced between these two outcomes.

While a flat universe requires the total energy density to be very close to the critical energy density, baryonic matter has been found to only contribute about 5 % to the total energy budget. In the 1980s, the possibility of a ‘cold dark matter’ contribution to the energy budget was considered (Blumenthal et al., 1984) and this has now been shown to contribute about 25 % (Planck Collaboration et al., 2015c). Soon after, the concept of a cosmological constant was revisited (Krauss and Turner, 1995), and the inclusion of  $\Lambda$  resulted in better fits to the data (Peebles (1984); Vittorio and Silk (1985); Efstathiou et al. (1990)), with the cosmological constant—attributed to the vacuum energy density or ‘dark energy’—contributing the remaining 70 % of

the required energy in the universe. It must be noted that when Einstein originally used the parameter  $\Lambda$  in his field equations, its purpose was to balance forces in a static universe. It is now used to represent the vacuum energy density, or dark energy, and is known as the cosmological constant. The evidence for the existence of dark energy is corroborated by observations of distant supernovae which indicate that the universe is expanding at an accelerated rate (Riess et al. (1998); Perlmutter et al. (1999)), amongst other such observations, and also by the fact that the exclusion of  $\Lambda$  in calculations of the age of the universe result in estimations that fall short of the age of some globular clusters (Krauss and Turner, 1995).

Cosmological models attempt to improve our understanding of the evolution of the universe using various parameters. Cosmological observations measure and constrain these parameters, thereby supporting or eliminating the cosmological models. Such parameters include the various density parameters,  $\Omega_b$ ,  $\Omega_{CDM}$ ,  $\Omega_\Lambda$ , and  $\Omega_k$ —representing ordinary matter, cold dark matter, dark energy, and curvature respectively—the Hubble parameter  $H$ , the adiabatic density perturbation amplitude  $A$  and spectral index  $n$ , and the reionization optical depth  $\tau$ . In 1992, the Cosmic Background Explorer (COBE) satellite made the historic detection of anisotropies in the Cosmic Microwave Background (CMB) (Smoot et al., 1992). Subsequent investigations of the CMB anisotropy put an end to a variety of models and the  $\Lambda$  cold dark matter ( $\Lambda$ CDM) model began to emerge as the standard cosmological model (Scott, 2006). The  $\Lambda$ CDM model is the simplest model that provides a good account of the existence and structure of the CMB, the large-scale structure of the universe, the accelerating expansion of the universe, and can be extended to include cosmological inflation.

Measurements of the CMB have shown incredible uniformity in temperature over the entire sky. This is particularly remarkable considering that the finite speed of light means that the opposite poles of the sky could never have been causally connected. This is known as the horizon problem. Another peculiar coincidence is known as the flatness problem. The current density of the universe is observed to be very close to the critical value for a flat universe. This suggests that the density of the early universe must have been *incredibly* close to the critical density. Adher-

ence to the Copernican principle, where nothing is special, makes scientists very nervous when numbers are conveniently close to a special case, and so cosmologists question the coincidence of a number that is so fine-tuned. Consider the first Friedmann equation, and for simplicity, let us ignore the cosmological constant:

$$H^2 = \frac{8\pi G}{3}\rho - \frac{kc^2}{a^2}. \quad (1.9)$$

This can be rearranged to

$$\frac{3a^2}{8\pi G}H^2 = \rho a^2 - \frac{3kc^2}{8\pi G} \quad (1.10)$$

and simplified to

$$(\Omega^{-1} - 1)\rho a^2 = -\frac{3kc^2}{8\pi G} \quad (1.11)$$

using Equation 1.8 and the dimensionless density parameter  $\Omega \equiv \frac{\rho}{\rho_c}$ . The right hand side of this equation is a constant, which means that the left hand side must also remain constant as the universe evolves. The term  $\rho a^2$  had to decrease by many orders of magnitude from the early universe to now, and with current measurements of  $\Omega \approx 1.0$ , the above equation indicates that the density parameter must have been very finely tuned.

A further problem with the Big Bang theory is called the magnetic monopole problem. The conditions in the early universe should have produced a proliferation of magnetic monopoles, and yet not a single one has ever been detected. These problems, amongst others, suggest that the standard hot Big Bang ( $\Lambda$ CDM) cosmology may still require some modification. One such modification is the idea of cosmic inflation. Alan Guth postulated the theory of inflation when trying to explain the extremely low density of magnetic monopoles in the present day. There are now several variations of this theory, but the fundamental proposal is that the universe went through a period of rapid, exponential expansion in the first moments after the Big Bang. In addition to solving the monopole problem, Guth soon realized that cosmic inflation would also resolve the horizon and flatness problems (Guth, 1981).

### 1.2.1 The Cosmic Microwave Background

The thermal spectrum of the cosmic microwave background is an incredibly close approximation to that of a perfect blackbody. The motion of the earth relative to the cosmic microwave background induces a non-cosmological anisotropy in the measured CMB signal at the microkelvin level. Once this has been accounted for, one has to measure to the microkelvin level before one finds any inconsistency in the CMB temperature. These anisotropies in the CMB temperature provide an excellent probe for many cosmological parameters as they encode a wealth of information about the early universe (White et al. (1994); Hu et al. (1997); Hu and Dodelson (2002); Scott and Smoot (2010)). CMB anisotropies were predicted by Sachs and Wolfe in 1967 when they theorized that fluctuations in the gravitational potential of the primordial plasma would have been imprinted on the CMB at large angular scales (Sachs and Wolfe, 1967). First measured by the Cosmic Background Explorer Digital Microwave Radiometer (COBE DMR) (Smoot et al. (1990); Smoot et al. (1992)), anisotropies in the cosmic microwave background have become an intense area of study. Projects like the Wilkinson Microwave Anisotropy Probe (WMAP) (Bennett et al., 2013) and Planck (Planck Collaboration et al., 2016a) have probed the CMB in both temperature and polarization over a range of frequencies and angular scales to provide constraints on the cosmological parameters with unprecedented accuracy (Hinshaw et al. (2013); Planck Collaboration et al. (2016a)). Table 1.2 lists the important properties of a range of prominent large-area CMB experiments.

The CMB temperature anisotropies in a sky map, represented by  $\Delta T(\hat{n})$ , where  $\hat{n}$  is a unit direction vector, can be decomposed using spherical harmonics according to

$$\Delta T(\hat{n}) = \sum_{\ell=1}^{\infty} \sum_{m=-\ell}^{\ell} a_{\ell m} Y_{\ell m}(\hat{n}), \quad (1.12)$$

with

$$a_{\ell m} = \int d\Omega_n \Delta T(\hat{n}) Y_{\ell m}^*(\hat{n}), \quad (1.13)$$

where  $Y_{\ell m}(\hat{n})$  are the spherical harmonic functions evaluated in the direction  $\hat{n}$ . If the distribution

of CMB anisotropy is Gaussian, then each  $a_{\ell m}$  is an independent Gaussian deviate, with

$$\langle a_{\ell m} \rangle = 0, \quad (1.14)$$

and

$$\langle a_{\ell m} a_{\ell' m'}^* \rangle = \delta_{\ell \ell'} \delta_{m m'} C_{\ell}, \quad (1.15)$$

where  $\langle a_{\ell m} a_{\ell' m'}^* \rangle$  implies an average over the statistical ensemble and  $\delta$  is the Kronecker symbol. The angular power spectrum,  $C_{\ell}$ , represents the variance in power in a given  $\ell$ -mode, and is given by

$$C_{\ell} = \frac{1}{2\ell + 1} \sum_{m=-\ell}^{\ell} |a_{\ell m}|^2. \quad (1.16)$$

CMB anisotropies can be predicted with remarkable precision because the underlying physics that generated them is well understood. Figure 1.1 is a plot of the theoretical CMB power spectrum, taken from (Scott, 2006). The structure of the power spectrum can be split into four regions, as shown in the figure, each dominated by a specific phenomenon. The large scale anisotropy ( $\ell < 100$ ) is caused by the Sachs-Wolfe effect (Sachs and Wolfe, 1967), an imprint of the initial conditions caused by a gravitational redshift of the CMB photons at the so-called ‘surface of last scattering’, and the integrated Sachs-Wolfe effect, which involves gravitational redshift along the line of sight.

The small scale ( $\ell > 100$ ) anisotropies are a result of acoustic oscillations in the primordial fluid (Hu and White (1996); Huterer and Turner (2001)). These sound waves were caused by perturbations in the gravitational potential leading to overdense and underdense regions in the primordial fluid (Silk (1968); Sunyaev and Zeldovich (1970); Bond and Efstathiou (1984); Bond and Efstathiou (1987); Holtzman (1989); Peebles et al. (2009)). This cycle of compression and rarefaction of the primordial fluid was imprinted onto the CMB power spectrum as small scale anisotropies, with the first peak ( $\ell \sim 200$ ) corresponding to the mode caught in its first compression by recombination (Hu and Dodelson, 2002) and subsequent peaks corresponding to other modes in the cycle. The first experiments to resolve the first peak of the CMB temperature power spectrum were the balloon-borne experiments BOOMERANG (de Bernardis et al., 2000) and

MAXIMA-1 (Hanany et al., 2000). Incidentally, these primordial density fluctuations are responsible for the large scale structure we see in the universe today.

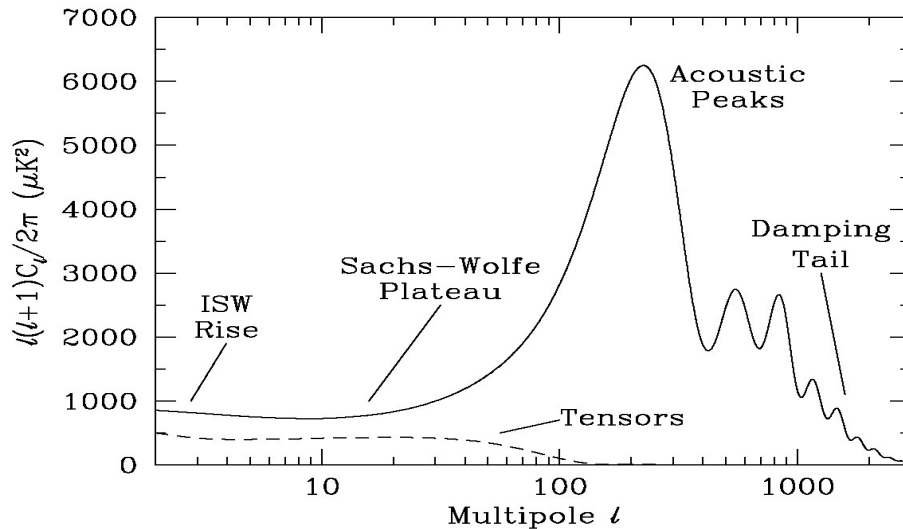


**Figure 1.1:** This plot shows the theoretical CMB angular power spectrum, and highlights the spatially dependent CMB temperature anisotropy as a function of the spherical harmonic multipole moment  $\ell$ . Image taken from Scott (2006).

The CMB anisotropies have been measured to very high precision by numerous experiments. The most recent measurements from the Planck satellite found the temperature and polarization spectra of the CMB to be consistent with the standard spatially-flat 6-parameter  $\Lambda$ CDM cosmology with a power law spectrum of adiabatic scalar perturbations (Planck Collaboration et al., 2015c). By combining their full-mission temperature and lensing data, they were able to place constraints on the Hubble constant  $H_0$ , matter density  $\Omega_m$  and tilted scalar spectral index  $n_s^*$ , consistent with their 2013 analysis (Planck Collaboration et al., 2014c), but with improved accuracy. They also placed improved constraints on the reionization optical depth  $\tau$ , spatial curvature  $\Omega_k$ , and placed an upper limit on the tensor-to-scalar ratio  $r^\dagger$ . Table 1.1 is a summary of the latest Planck CMB parameter measurements, taken from Planck Collaboration et al. (2015c).

\*Describes the scale-dependence of primordial density fluctuations

†Parametrization of the amplitude of gravitational waves.

**Table 1.1:** *Summary of Planck CMB parameter measurements.*

| Cosmological Parameter | Measured Value                                      |
|------------------------|---|
| $H_0$                  | $(67.8 \pm 0.9) \text{ km s}^{-1} \text{ Mpc}^{-1}$ |
| $\Omega_m$             | $0.308 \pm 0.012$                                   |
| $ \Omega_k $           | $< 0.005$   |
| $n_s$                  | $0.968 \pm 0.006$                                   |
| $\tau$                 | $0.066 \pm 0.016$                                   |
| $r$                    | $< 0.11$  |

### 1.2.1.1 CMB Polarization

The polarized CMB signal provides a direct probe of the universe at the time of recombination. This is because CMB polarization is a direct result of the CMB photons scattering off the primordial fluid during recombination and escaping, providing an image of the surface of last scattering. Polarization measurements enhance the precision of cosmological parameter estimation associated with acoustic oscillations and act as a consistency check for the interpretation of the acoustic peaks. They also provide unique probes of inflation as their origin from the surface of last scattering allows us to investigate correlations on scales larger than the causal horizon at recombination. In addition, the polarization carries directional information (in the tensor field), which provides a means of isolating the gravitational waves predicted by inflation models.

Rees (1968) was the first to predict that the CMB was polarized when he considered that radiation undergoing multiple Thomson scatterings in an anisotropic environment, such as the primordial fluid before recombination, would become linearly polarized. This linear polarization is the result of a quadrupole anisotropy at the surface of last scattering caused by scalar, vector or tensor perturbations in the primordial fluid. Consider a case of Thomson scattering between two photons and an electron as illustrated in Figure 1.2. The photon approaching the electron from an underdense region, indicated in the figure by the thick blue lines, will excite the electron, causing it to oscillate both vertically and in the direction of the observer. The photon approach-

ing the electron from an overdense region, indicated by thin red lines, will cause the electron to oscillate both horizontally and in the direction of the observer. The observer, unable to detect the oscillation towards and away from himself, will instead see the electron oscillating vertically and horizontally. In the case of an isotropic medium, these oscillations will have equal magnitude and there will be no polarization, but in the case of an anisotropic medium, linear polarization will occur in favour of the higher energy photon.

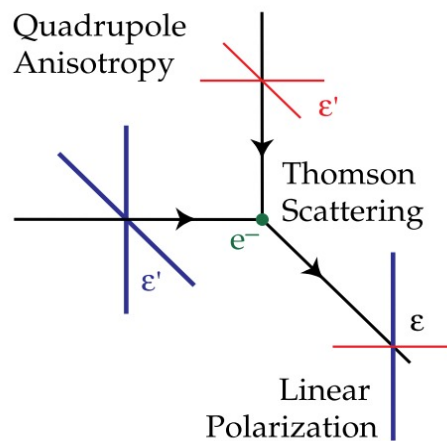


**Figure 1.2:** *The quadrupole anisotropy resulting from the Thomson scattering of CMB photons. Image taken from Hu and White (1997).*

We can use the Stokes parameters to describe the polarization of the CMB, however, these are co-ordinate dependent and depend on the orientation relative to the observer. In order to avoid this, we describe CMB polarization in a set of two co-ordinate independent, orthogonal components called  $E$ -mode for the curl-free ‘electric’ component and  $B$ -mode for the divergence-free ‘magnetic’ component of polarization. The quadrupolar anisotropies in the primordial fluid, which gave rise to the polarization in the CMB signal, were created by scalar, vector, and tensor perturbations.  $E$ -mode polarization is symmetric about the direction of travel and is a result of both symmetric scalar perturbations and asymmetric tensor perturbations in the primordial plasma.  $B$ -mode polarization is chiral, exhibiting handedness, and carries directional informa-

tion.  $B$ -mode polarization is the result of asymmetric tensor perturbations only, however, gravitational lensing can cause a switch in polarization from  $E$ -mode to  $B$ -mode. This phenomenon was first detected in 2013 by the South Pole Telescope (Hanson et al., 2013) and measured independently by the POLARBEAR experiment (Ade et al., 2014). The difference between  $E$ - and  $B$ -mode polarization is shown in Figure 1.3. Vector perturbations were subdominant at the time of recombination, when the CMB signal was generated, and as such the polarized CMB signal is dominated by scalar and tensor perturbations (Baumann et al., 2009).

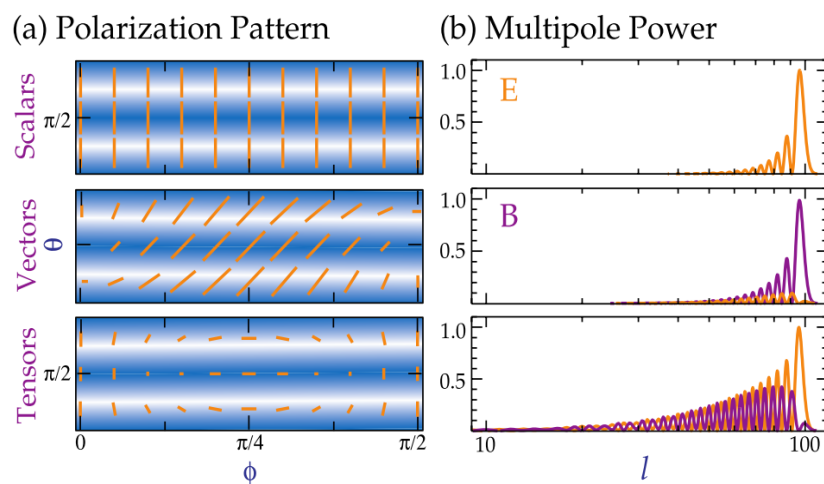


**Figure 1.3:** Examples of  $E$ - and  $B$ -mode polarization arising from scalar, vector, and tensor quadrupolar anisotropies. Image taken from Hu and White (1997).

Current experiments are trying to find evidence for new science beyond the standard  $\Lambda$ CDM model and one of the most exciting prospects is the attempt to constrain  $r$  (the ratio of tensor to scalar amplitude fluctuations). The simplest models of inflation predict the existence of gravitational waves (tensor fluctuations), which induce a  $B$ -mode polarization into the CMB (Kamionkowski et al., 1997, Seljak and Zaldarriaga, 1997). Projects like the Background Imaging of Cosmic Extragalactic Polarization (BICEP2) (Nguyen et al., 2008) and the Keck Array (Staniszewski et al., 2012) are interrogating the CMB in search of a  $B$ -mode polarized signal and while they have yet to make a  $B$ -mode detection, they are placing upper bounds on the value of  $r$ . BICEP2 did in fact claim to have made a  $B$ -mode detection but it was later found that foreground

dust emission was responsible for the detected signal (BICEP2 Collaboration et al., 2014). The discovery of  $B$ -mode polarization in the CMB would be as powerful a validation of the theory of inflation as the discovery of the CMB was for the Big Bang.

One of the biggest challenges facing CMB  $B$ -mode experiments is that the signal is buried in Galactic foreground radiation. For example, though BICEP2 searched one of the cleanest parts of the sky, it was limited by foreground radiation, meaning that Galactic foreground radiation is a problem that cannot be avoided. The primary contributors to Galactic foreground radiation are synchrotron and dust emission, with synchrotron dominating at frequencies below 70 GHz and thermal dust dominating at higher frequencies. Other contributors include anomalous microwave emission and free-free emission, though these are expected to be largely unpolarized and should therefore be subdominant contaminants for CMB polarimeter experiments. Techniques like foreground component separation allow astronomers to remove the foreground contaminant signals by combining their data sets with others that have specifically measured Galactic foregrounds. For example, the Planck Collaboration applied this technique by combining their temperature data with WMAP 9-year sky maps (Bennett et al., 2013) and the Haslam et al 408 MHz map (Haslam et al., 1981). They found that they were limited by internal degeneracies at low frequencies between synchrotron, spinning dust, and free-free radiation and that they required additional observations from low frequency experiments to break these degeneracies (Planck Collaboration et al., 2015a). One such low frequency experiment is the C-Band All Sky Survey (C-BASS).

### 1.2.2 A Brief Summary of Contemporary Experiments

Table 1.2 provides an overview of some of the latest large-area CMB surveys. The surveys in this table are satellite-borne and cover the entire sky with angular resolutions smaller than the C-BASS beam. Other projects that probe the CMB include balloon-borne experiments such as the E and B Experiment (EBEX) (Oxley et al., 2004) and SPIDER (MacTavish et al., 2008), and ground based experiments such as the Atacama Cosmology Telescope (ACT) (Louis et al., 2017), the Cosmology Large Angular Scale Surveyor (CLASS) (Harrington et al., 2016), the

Background Imaging of Cosmic Extragalactic Polarization (BICEP 1,2,3), the Keck Array, POLARBEAR, and the South Pole Telescope (SPT). Data from C-BASS will aid these and other CMB experiments in the removal of Galactic foreground radiation.

C-BASS is an experiment designed to aid these CMB experiments by placing constraints on the Galactic synchrotron component of the foreground signal. Table 1.3 provides an overview of C-BASS and other contemporary foreground experiments. A well known low frequency survey is the 408 MHz Haslam survey. The data from this survey, even though it is affected by systematics, has proved useful in CMB component separation. Many attempts have been made to reduce the effect of systematics in Haslam data, most recently by Remazeilles et al. (2015). The Villa Elisa (Testori et al., 2008) and the Dominion Radio Astrophysical Observatory (DRAO) 26 m (Wolleben et al., 2006) surveys provide information on the polarized foreground signal at 1.4 GHz, but unfortunately low frequency polarization is strongly affected by Faraday rotation. The depolarizing effect of Faraday rotation can be estimated, given enough data at different frequencies (Taylor et al., 2009). Data from other low frequency polarization surveys, such as the S-band Parkes All Sky Survey (S-PASS) (Carretti, 2010), along with data from C-BASS should enable us to account for the depolarizing effect of Faraday rotation, providing more accurate constraints on the low frequency synchrotron foreground emission component. A large area survey between C-BASS and WMAP is the Q-U-I JOint TENERIFE (QUIJOTE) CMB experiment (Génova-Santos et al., 2015a), which at 10–40 GHz, will provide constraints of the AME foreground component.

**Table 1.2:** *Overview of relevant CMB experiments.*

| Survey     | Frequency [GHz] | FWHM [arcmin] | Declination Coverage | Stokes | Sensitivity      | Reference                           |
|------------|-----------------|---------------|----------------------|--------|------------------|-------------------------------------|
| WMAP       | 22.8–94         | 49–15         | All Sky              | IQU    | 4 $\mu$ K        | Bennett et al. (2013)               |
| Planck LFI | 28.4–70         | 32–13         | All Sky              | IQU    | 3 $\mu$ K        | Planck Collaboration et al. (2016a) |
| Planck HFI | 100–353         | 10–5          | All Sky              | IQU    | 0.2–0.5 $\mu$ K  | Planck Collaboration et al. (2016a) |
| Planck HFI | 545, 857        | 5             | All Sky              | I      | 0.4, 0.8 $\mu$ K | Planck Collaboration et al. (2016a) |

**Table 1.3:** *Overview of contemporary Galactic foreground radio surveys.*

| Survey      | Frequency [GHz] | FWHM [arcmin] | Declination Coverage | Stokes | Sensitivity | Reference                     |
|-------------|-----------------|---------------|----------------------|--------|-------------|-------------------------------|
| Haslam      | 0.408           | 51            | All Sky              | I      | 1 K         | Haslam et al. (1981)          |
| DRAO (26 m) | 1.4             | 36            | $> -29^\circ$        | QU     | 12 mK       | Wolleben et al. (2006)        |
| Vila Elisa  | 1.4             | 35.4          | $< +10^\circ$        | IQU    | 9 mK        | Testori et al. (2008)         |
| S-PASS      | 2.3             | 9             | $< 0^\circ$          | IQU    | 0.1 mK      | Carretti (2010)               |
| C-BASS      | 4.5–5.5         | 44            | All Sky              | IQU    | 0.1 mK      | King et al. (2014)            |
| QUIJOTE     | 10–40           | $\approx 60$  | $> 0^\circ$          | IQU    | 25 $\mu$ K  | G enova-Santos et al. (2015a) |

### 1.3 Galactic Foreground Emission

Studies of the CMB are severely affected by the presence of Galactic foreground radiation, which can be several orders of magnitude brighter than the polarized CMB signal. This radiation, together with other unwanted foreground signals from extra-Galactic sources, is a common contaminant in CMB data and must be addressed in order to accurately measure the CMB signal. Galactic foreground signals arise from several emission mechanisms and occur at different frequencies. They are also not uniformly distributed across the sky. Of particular interest to C-BASS are the ‘low’ frequency diffuse foreground signals, below 100 GHz, where free-free, thermal dust, anomalous microwave emission (AME) and synchrotron radiation dominate. Figure 1.4, taken from (Planck Collaboration et al., 2015a), provides an overview of the main foreground components with brightness temperature RMS as a function of frequency being evaluated over 93 % of the sky in temperature (top panel), and 73 % of the sky in polarization. This plot highlights the frequency dependence of each foreground component, with thermal dust dominating at higher frequencies and synchrotron dominating at lower frequencies. It is this frequency dependence that allows us to model each foreground signal as an independent component and enables us to accurately extract the CMB signal from the foreground dominated data. It is particularly important to note that the polarized CMB signal (bottom panel of Figure 1.4) is completely obscured by foreground radiation, highlighting the need for accurate foreground removal. The total foreground signal has been well constrained by observations, but there is still uncertainty in how much each foreground component contributes to the overall signal, with different model assumptions greatly affecting the power contributed by each emission mechanism (Planck Collaboration et al., 2016c). More observations between 5 and 20 GHz are required to provide clarity on the

contributions from each foreground component and to break the current degeneracies in foreground models. We now examine each of the main foreground components in turn.

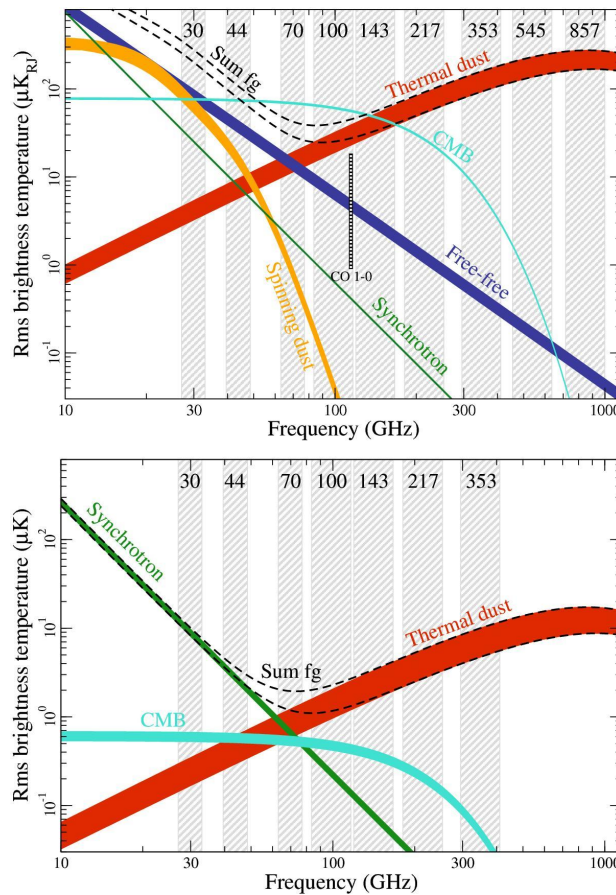


**Figure 1.4:** *Brightness temperature RMS as a function of frequency for different foreground components in temperature (top) and polarization (bottom). The dark bands indicate the frequencies observed by the Planck experiment. Image taken from Planck Collaboration et al. (2015a).*

### 1.3.1 Free-Free Emission

Free-free, or bremsstrahlung emission is radiation resulting from the acceleration of a charged particle in the Coulomb field of another charged particle, and, in the radio regime, typically emanates from regions of warm ionized hydrogen ( $T \approx 10^4$  K). The random nature in which the ionized particle interactions occur means that free-free radiation is unpolarized, and it has a spectral index in the optically thin regime of  $\beta = -2.1$  at GHz frequencies, steepening slightly

( $\Delta\beta < 0.05$ ) at higher frequencies (Rybicki and Lightman (1986); Draine (2011)). The free-free emission spectrum is very well defined by a simple power law,  $T = \nu^\beta$ , making it one of the most stable solutions for component separation analysis (Planck Collaboration et al., 2014a). It is, however, very difficult to measure as the signal is weaker across all frequencies than other foreground emission mechanisms (Smoot, 1998). Efforts have been made to constrain high-latitude free-free emission, using  $H_\alpha$  as a tracer, since both are related to the same ionized medium, (Dickinson et al. (2003); Finkbeiner (2003)), but this has not proved to be very accurate (Planck Collaboration et al., 2016c).

### 1.3.2 Synchrotron Emission

Synchrotron radiation is the dominant foreground at frequencies up to a few GHz (Lawson et al., 1987), and will be the foreground most constrained by C-BASS. Synchrotron emission arises from the spiralling of electrons and positrons around a magnetic field line. The relativistic leptons responsible for synchrotron radiation have two possible sources: supernova remnants and cosmic rays. The velocity change of these charged particles in the presence of a magnetic field results in polarized emission. It was predicted in the early 1900s by Schott (1912) and was first observed at the General Electric Synchrotron Accelerator by Elder et al. (1947). Astronomical synchrotron radiation was first detected from the source M87 by Burbidge (1956).

Synchrotron emission spectrum is usually described as a power law with brightness temperature  $T_B(\nu) \propto \nu^{\beta_S}$ . This is due to the power law distribution of relativistic electrons  $N(E) \propto E^{\beta_S+3}$ . However, this model is a poor fit over a large range of frequencies due to the range in synchrotron spectral index  $\beta_S$ . Synchrotron spectral index exhibits spatial variation across the sky, with maps of total intensity (Lawson et al. (1987); Reich and Reich (1988); Davies et al. (1996); Platania et al. (1998, 2003); Bennett et al. (2003); Dickinson et al. (2009); Gold et al. (2011)) and microwave polarization from WMAP (Fuskeland et al. (2014); Vidal et al. (2015)) showing variations in the range  $-3.3 < \beta < -2$ , steepening as the measurements move away from the Galactic plane. This is due to energy loss as the synchrotron particles propagate through the

Galaxy, and free-free emission. The current theory is that if the power law model is accurate, then two distinct spectral index regimes are required to best fit the data, and that there must be a break in the synchrotron spectral index, where it changes from flatter ( $\sim -2$ ) to steeper ( $\sim -3$ ) (Kogut, 2012). This is a major source of uncertainty in foreground component modelling, and C-BASS maps will add vital information in the quest to constrain the spectral index of synchrotron radiation over the entire sky.

Synchrotron radiation is highly polarized, with an intrinsic polarization of 70–75 %, oriented perpendicular to the projected magnetic field in the source region, and observed polarizations exceeding 30 %. The intrinsic polarization is reduced by the superposition of different magnetic field lines along the line of sight, as well as Faraday rotation. Faraday rotation is a frequency dependent rotation of the polarization angle of an electromagnetic wave propagating through a magnetic field. The effect of Faraday rotation decreases with increased frequency, and the effect on C-BASS measurements at 5 GHz should be negligible.

### 1.3.3 Thermal Dust Emission

Interstellar dust consists of nanometer-sized silicates, carbonaceous particles, and polycyclic aromatic hydrocarbons (PAHs). Thermal dust emission emanates from these interstellar dust grains when they absorb optical and UV radiation, begin to vibrate and heat up to temperatures of around 10–30 K, and re-emit photons in the microwave and far-infrared regimes (Draine, 2011). This is the dominant foreground emission mechanism at frequencies above 70 GHz. The thermal dust emission spectral energy distribution (SED) can be approximated with a modified black body spectrum, that is, a Planck spectrum  $B(\nu, T_D)$  multiplied by an emissivity  $\propto \nu^{\beta_D}$ . Planck Collaboration et al. (2015d) investigated the spectral indices of dust emission in both intensity and polarization. They used Planck 353 GHz Stokes I, Q and U maps as dust templates and cross-correlated them with Planck and WMAP data from 23 to 353 GHz, over 10 degree radius circular patches. They found that both indices remained remarkably constant over the sky, with mean values of  $1.59 \pm 0.02$  for polarization and  $1.51 \pm 0.01$  for intensity for a mean dust

temperature of 19.6 K. They also found that the mean SED increases with decreased frequency ( $\nu < 60$  GHz), for both intensity and polarization and attributed this to a correlation between the synchrotron and dust components. Dust emission is polarized due to the fact that dust particles are asymmetric, and have a preferred orientation along magnetic field lines. The maximum observed dust polarization fraction is 19.8 % Planck Collaboration et al. (2015b).

### 1.3.4 Anomalous Microwave Emission

Anomalous microwave emission was discovered by Leitch et al. (1997) when it was observed with the Ring5m experiment, a survey designed to detect CMB anisotropies at arcminute angular scales, based at OVRO. They detected excess emission in certain parts of the sky at 14.5 GHz that was not predicted by thermal dust and synchrotron models. There was a strong correlation between this excess emission and the 100  $\mu\text{m}$  far-infrared dust emission maps produced by the Infrared Astronomical Satellite (IRAS), suggesting that the anomalous emission was dust related. AME has been the subject of intense study (de Oliveira-Costa et al. (2004); Davies et al. (2006); Gold et al. (2011); Ghosh et al. (2012); Planck Collaboration et al. (2014b)).

The AME spectrum is most significant between 10–60 GHz, with a peaked spectrum that is rising at low frequencies, and falling steeply at high frequencies. The best example of AME comes from the Perseus molecular cloud (Watson et al. (2005); Planck Collaboration et al. (2011); Génova-Santos et al. (2015b)). The AME spectrum is spatially variable, with different clouds peaking at different frequencies (Planck Collaboration et al. (2016c, 2014b)). At low altitude, the superposition of different clouds with a range of peak frequencies could allow AME to mimic free-free or synchrotron spectra. This makes it difficult to separate the different foreground components, and is a major cause of uncertainty in component separation models. This, combined with the weakness of the signal, makes it very difficult to measure the AME polarization signal, although several measurements indicate that AME is weakly polarized to the level of a few percent (Mason et al. (2009); Dickinson et al. (2011); López-Caraballo et al. (2011); Rubiño-Martín et al. (2012); Hoang et al. (2013); Planck Collaboration et al. (2016c)).

The actual source of AME is still uncertain. The spectral index of the emission measured by the Ring5m experiment was flatter than expected and Leitch et al. (1997) believed that this flatter index was caused by the inclusion of some anomalous component, suggesting hot ( $\sim 10^6$  K) free-free emission and flat spectrum synchrotron as possible causes. Bennett et al. (2003) also suggested flat-spectrum synchrotron to be the likely cause, but the peaked spectrum and the close correlation with far-infrared templates makes this unlikely. Draine and Lazarian (1998a,b) suggested a ‘spinning dust’ model, in which an electric dipole on rotating dust particles would emit radiation at a frequency related to the rotational velocity. Later, Draine and Lazarian (1999) suggested another mechanism in which thermal vibrations in ferromagnetic dust particles induce a magnetic dipole emission.

### 1.3.5 Point Sources and Confusion Noise

The different types of Galactic foreground radiation discussed so far have been diffuse in nature as they arise from various regions within the Galaxy rather than specific sources. Extragalactic foreground radiation emanates from various point sources such as radio galaxies and other active galactic nuclei. Bright sources, such as the radio galaxy Cygnus A, are easily identified in survey maps. The rest contribute to the ‘confusion noise’, that is, the background noise within the beam size caused by the sum of sources that are too weak or numerous to be individually detected. Noise confusion is dependent on the normalised beam response, as well as the differential source distribution, so for a Gaussian beam with effective beam area  $A_e$ :

$$\sigma_c^2 = \frac{\lambda^2}{2A_e} \int_{S_{min}}^{S_{max}} S^2 \frac{dN}{dS} dS, \quad (1.17)$$

where  $N$  is the frequency dependent source count and  $S$  is the flux density. For C-BASS, we expect to be confusion limited in intensity, with an estimated confusion limit of  $\sim 0.9$  mK, but not in polarization as the fractional polarization of astronomical sources is very low, of order 3.5% (Battye et al., 2011).

### 1.3.6 Galactic Foreground Removal Techniques

Some astronomical signals are bright enough to be observed, even in the presence of Galactic foreground radiation. For example, early detections of  $EE$  and  $TE$  CMB polarization were made by measuring small patches of sky with low levels of foreground contamination (Readhead et al. (2004); Leitch et al. (2005); Barkats et al. (2005)). Other projects, like BICEP and Keck (BICEP2 Collaboration et al., 2016), also scanning small patches of sky with low levels of foreground contamination, have struggled in their quest to detect the gravitational  $B$ -mode signal because polarized emission from Galactic dust at high latitudes has proven to be higher than anticipated (Flauger et al. (2014); Mortonson and Seljak (2014); Planck Collaboration et al. (2016b, 2015b)). It is clear that any search for weak astronomical signals will require some form of Galactic foreground removal, and that, in turn requires more measurements of Galactic foregrounds at different frequencies, highlighting the importance of projects like C-BASS (Planck Collaboration et al. (2016c); Krachmalnicoff et al. (2016); Remazeilles et al. (2016)).

The different Galactic foreground mechanisms exhibit strong frequency dependence in their power spectra, while the CMB produces a near perfect blackbody spectrum. This information can be used to model the effects of the different emission mechanisms, allowing astronomers to remove them from their data. This can be done using a number of techniques, including template cleaning, blind component separation, and parameter estimation (Dunkley et al., 2009).

## 1.4 Thesis Overview

This thesis consists of five chapters. The first chapter provides a brief history of cosmological research, highlighting certain major discoveries and breakthroughs in the journey to our current understanding of Big Bang cosmology. This chapter also describes the current status of CMB observational cosmology and discusses the prevalence and emission mechanisms of Galactic foreground emission. This is done in an effort to illustrate how important data from the C-Band All Sky Survey (C-BASS) will be for removing foreground contamination from CMB

data. Chapter two introduces the C-BASS experiment. In this chapter I describe the goals and survey requirements of the project before giving a detailed description of the experiment itself. In chapter three, I describe the low-level time stream data analysis pipeline and provide a thorough description of the radio frequency interference (RFI) removal process, which represents a large part of my analysis work. Chapter four describes the map making process and contains results from data self-consistency tests. These tests show the state of systematic errors in our data and will be used to judge data quality. In Chapter five, I describe the commissioning of the southern instrument, as well as the RFI environment at Klerefontein. Finally, I provide some concluding remarks and indicate work to be done in the future.

# Chapter 2

## The C-Band All Sky Survey

In this chapter I will provide a general description of the C-Band All Sky Survey. I will discuss our science goals and how we intend to achieve them, as well as give details on the hardware of both instruments. I will focus particularly on the optical configuration and receiver design, describing both similarities and differences between the two instruments.

### 2.1 The C-Band All Sky Survey

The C-Band All Sky Survey (C-BASS) is a ground based radio telescope experiment that maps the entire sky in Stokes I, Q and U (King et al. (2010)). The survey is centred on 5 GHz with a 1 GHz bandwidth from 4.5 to 5.5 GHz, which is low enough to avoid Faraday rotation and high enough for maximal sensitivity to synchrotron radiation. The experiment consists of two telescopes, one based at the Owens Valley Radio Observatory (OVRO) in California and the other at the Square Kilometre Array (SKA) Support Base in Klerefontein, South Africa. The telescope at OVRO, referred to as the northern telescope, observed the sky from November 2012 until March 2015 and has now completed observations with data analysis at an advanced stage. The telescope in Klerefontein, referred to as the southern telescope, underwent receiver commissioning at the Hartebeesthoek Radio Astronomy Observatory (HartRAO), just outside Johannesburg, and was moved to site in May 2014. It has suffered a very long commissioning phase as a multitude of

different problems have delayed the commencement of science operations. During my PhD, I have been involved in commissioning work with the southern system, as well as data analysis with both the northern and southern system. My primary focus has been on identifying and removing man made radio frequency interference (RFI) in the northern data and characterising the RFI environment of the southern system. The following chapter contains a detailed description of both telescopes.

C-BASS consists of two similar telescopes, shown in Figure 2.1, with their key characteristics summarised in Table 2.1. The fundamental difference between the northern and the southern system is that the northern system has a fully analog receiver, while advances in digital technology allowed the southern receiver, designed and built several years later, to have a digital back end. This critical difference directly affected the manner in which RFI was treated in each system. The northern receiver, being fully analog, was forced to use notch filters to remove frequencies in which RFI was prevalent. Unfortunately, these notch filters reduced the northern bandwidth considerably from 1 GHz to 489 MHz. The southern receiver splits the data into 128 frequency channels using two FPGA ROACH boards, allowing all the RFI removal to be done in post-processing. Another notable difference between the two systems is the dish size and corresponding optical configuration. The northern dish is smaller, at 6.1 m in diameter, and is arranged in a Gregorian configuration. The size of the dish results in significant ground spillover, which is limited by absorbing baffles on the outer rim of the primary and secondary reflectors, and is also removed in post-processing. The larger southern dish, at 7.6 m in diameter, is under-illuminated (Holler et al. (2013)), eliminating the need for absorbing baffles, and has a Cassegrain configuration.

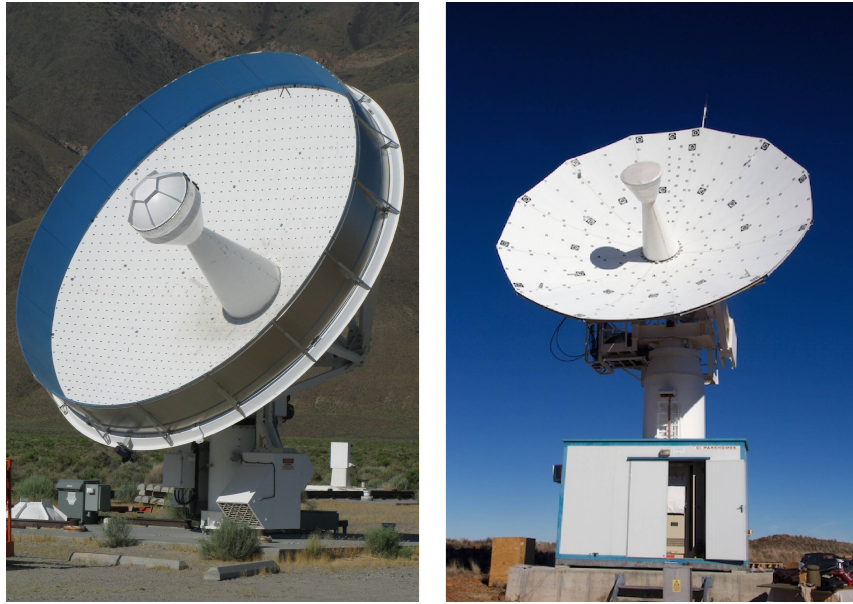


**Figure 2.1:** Photographs of the C-BASS telescopes on site, with the northern telescope on the left.

**Table 2.1:** Summary of northern and southern telescope parameters.

|                       | Northern System                | Southern System                  |
|-----------------------|--------------------------------|----------------------------------|
| Location              | Owens Valley Radio Observatory | SKA Support Base in Klerefontein |
| Bandwidth             | 4.5–5.5 GHz                    | 4.5–5.5 GHz                      |
| Back End              | Analog                         | Digital                          |
| Dish Diameter         | 6.1 m                          | 7.6 m                            |
| Optical Configuration | Gregorian                      | Cassegrain                       |
| Angular Resolution    | 0.73°                          | 0.73°                            |
| System Temperature    | 20.5 K                         | 22 K                             |
| Sensitivity           | 0.1 mK per beam                | 0.1 mK per beam                  |

### 2.1.1 Science Goals

The primary goal of the C-BASS experiment is to aid in the measurement of the polarized CMB signal (King et al. (2010)). This will be achieved with the production of high fidelity all-sky maps

of Galactic synchrotron emission in Stokes I, Q and U. These maps will be used by CMB experiments for Galactic foreground component separation and will provide a vital boost in the quest for the detection of primordial  $B$ -modes. The primary foreground contaminants are dust and synchrotron radiation, and while synchrotron radiation is dominant at frequencies below that of the CMB, its influence at higher frequencies cannot be ignored. In order to be able to detect the weak CMB  $B$ -mode signal, it must be separated from the foreground signal. This requires a more accurate measurement of the foreground signal than is currently available (Kogut et al. (2007), Gold et al. (2011), Macellari et al. (2011)). By accurately measuring the Galactic synchrotron signal at 5 GHz, C-BASS will provide a vital link between other low frequency foreground experiments like the 408 MHz Haslam experiment (Haslam et al. (1981)) and the 1.4 GHz Dominion Radio Astrophysical Observatory (DRAO) survey (Wolleben et al. (2006)), and dust foreground limited microwave frequency experiments like Wilkinson Microwave Anisotropy Probe (WMAP) 23 GHz maps (Page et al. (2007)). Secondary experiment goals include probing the Galactic magnetic field using synchrotron radiation and searching for new areas of anomalous microwave emission.

### 2.1.2 Survey Requirements

We wish to measure total intensity and linear polarization, producing a map of the entire sky with sensitivity on all scales from  $\ell \approx 300$  up to the dipole. As an interferometer is insensitive to scales larger than the antenna beam, the most feasible ground-based instrument with which to conduct this survey is a total power scanning telescope. C-BASS consists of two such telescopes and achieves full sky coverage by having one telescope in the northern hemisphere and another in the southern hemisphere. The decision was made to place the two telescopes at latitudes that allowed significant scan overlap in order to ensure that data from each could be calibrated to one another. Both receivers follow the same architecture, have identical cryogenic front ends, and are matched to have the same resolution and similar system temperatures. The details of their optics will be discussed in the next section.

The central frequency was chosen to be 5 GHz. The total intensity of the Galactic synchrotron signal increases with decreased frequency. This would suggest that anyone wishing to constrain this signal should measure as low a frequency as possible, however, we also wish to measure the linear polarization signal and this signal is affected by Faraday rotation at low frequencies. Multiple Faraday rotations along the line of sight could result in the depolarization of this signal. 5 GHz was chosen as a reasonable compromise for maximum total intensity and minimum depolarization.

The C-BASS receiver resolution was determined by need to be able to measure the Galactic synchrotron signal on angular scales relevant to the CMB  $B$ -mode signal, requiring a spherical harmonic multipole moment  $l \approx 300$ . With a central frequency of 5 GHz and a dish diameter of 6.1 m, the required angular resolution of  $0.73^\circ$  is determined by

$$\theta_{HPBW} \approx \frac{1.2\lambda}{D}. \quad (2.1)$$

We require a minimum 5-sigma detection in polarization over at least 90 % of the sky. In King et al. (2014) we estimated that the polarized intensity signal strength over 90 % of the sky was at least 0.5 mK, resulting in a required linear polarization sensitivity of  $\sim 0.1$  mK/beam. This estimation was achieved by interpolating between existing maps at 1.41 GHz (DRAO) and 23 GHz (WMAP). The sensitivity in intensity is expected to be confusion limited at  $\sim 1$  mK. We do not expect to be confusion limited in polarization as most sources are unpolarized and source polarization angles should be randomly distributed. The sensitivity is calculated using the radiometer equation

$$\sigma = \frac{T_{sys}}{\sqrt{\Delta\nu\tau}} \quad (2.2)$$

with an estimated system temperature  $T_{sys}$  of 22 K.

In order to achieve the desired sensitivity, our scanning strategy uses long continuous 360 degree azimuth sweeps of the sky at constant elevation. This allows each pixel of the final map to contain multiple sweeps in different directions. We scan at constant elevation to minimise the effect of ground spillover, which is a reasonably consistent function of azimuth and elevation, as

well as to reduce the effect of  $1/f$  noise caused by fluctuations in atmospheric water distribution as a function of elevation. Most scans are performed at a slew rate of 4 degrees per second. This is the highest speed that both antennas can comfortably achieve and a high slew rate reduces  $1/f$  noise. We employed a series of slew rates in different schedules to combat systematic effects such as mains frequency and 1.2 Hz microphonics caused by the cold head cycle frequency. To ensure a consistent slew rate over the entire azimuth scan, the antenna would slew at the required rate for a full 360 degrees before decelerating, halting and turning around. We thus have full sky coverage at consistent slew rates in both clockwise and anticlockwise directions. Sixty per cent of our scans have been conducted at an elevation equal to the latitude of the telescope site. This means that these scans always pass through the celestial poles, giving us a reference point in each scan that can be used to investigate signal drifts. These scans resulted in a very high hit count at the poles and the lower declination limit, but a low hit count elsewhere. To achieve a more even hit count distribution, we also scanned at elevations of 10, 30 and 40 degrees above the celestial pole. Survey schedules last between one and a half and two hours and run day and night, with sun and moon contamination addressed in post processing. A sky dip is performed at the beginning and end of every schedule to account for atmospheric opacity and calibration scans are performed on bright radio sources such as TauA and CasA in between survey schedules. Occasional house keeping schedules such as sky stares to monitor gain drifts, RFI scans, and pointing scans are performed at the observer's discretion. A plot of the time stream data from a typical Elevation 37 survey schedule, conducted at an elevation of 37 degrees, is shown in Figure 2.2. This figure shows the intensity data in the top panel, azimuth position in the middle panel, and elevation position in the bottom panel. Note the regular noise events in the intensity data which coincide with the telescope being positioned at the beginning of its azimuth scan, always when the telescope is about to scan from 0 to 360 degrees. Also note the sky dips at the beginning and end of the schedule, with an increase and then decrease in elevation and a corresponding decrease and then increase in the intensity while the azimuth remains constant at 0 or 360 degrees.

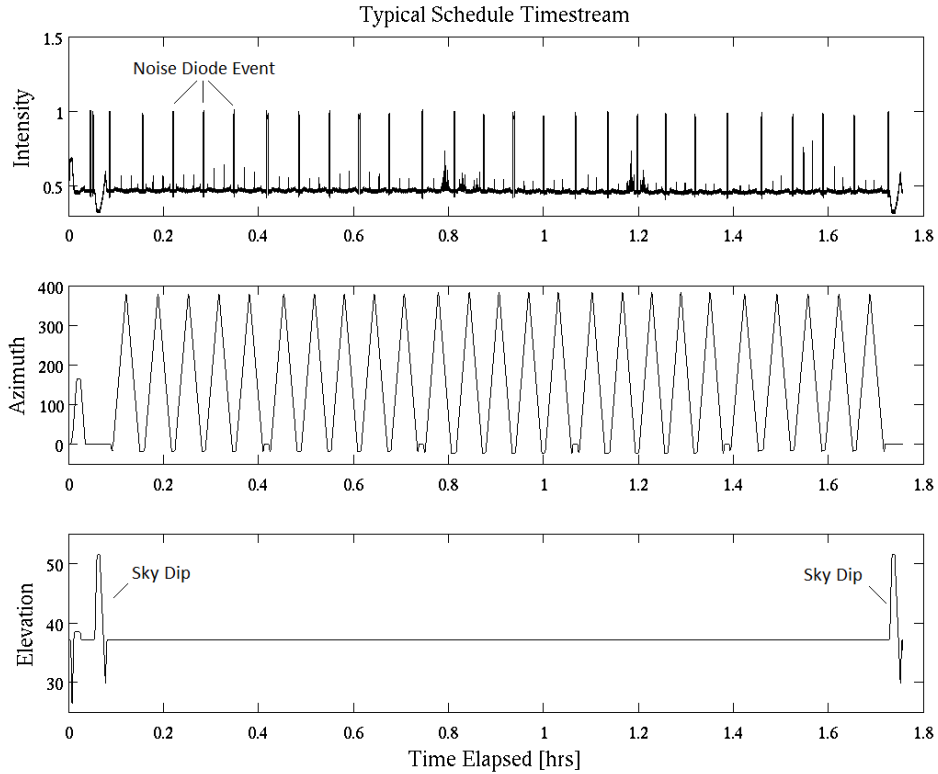


**Figure 2.2:** A plot of time stream data from a typical Elevation 37 survey schedule, with intensity in the top panel, azimuth in the middle panel, and elevation in the bottom panel. The regular spikes seen in the plot in the top panel are the noise diode events, while the spikes seen in the plot in the bottom panel are the sky dips.

## 2.2 C-BASS Optics

As stated previously, the C-BASS experiment consists of two similar receivers mounted on different antennas. The northern antenna was a 6.1 m diameter prototype for the NASA Deep Space Network (Imbriale and Abraham, 2004) and the southern antenna was a 7.6 m diameter low-earth-orbit telecommunications dish. Both antennas were donated to the project and as such were not designed specifically for C-BASS, having originally been designed for satellite communication. Both antennas had a focal ratio of  $f/D = 0.36$  but the effective focal ratio of the southern antenna is 0.46 as the primary reflector is under-illuminated with the feed only

illuminating the area of the northern primary reflector. Thus the secondary mirrors had to be specially designed for each receiver to ensure that the main beam patterns were the same for both telescopes up to the first null. Other optical requirements for the secondary mirror included low sidelobe and cross-polarization signal levels, and constant phase in the primary mirror aperture. This resulted in the secondary reflectors being completely different from one another with the northern system having a Gregorian configuration with a deep concave ellipsoidal secondary reflector and the southern system having a Cassegrain configuration with convex hyperboloidal secondary reflector.

The minimization of sidelobes is vital in a ground-based total-power scanning telescope as such instruments are vulnerable to contamination by scan-synchronous systematics in the time-ordered data. These spurious signals include ground reflections and geostationary man made radio frequency interference (RFI). The presence of scan-synchronous signals, introduced through antenna sidelobes and cross-polarization, would have a devastating impact on our efforts to produce high fidelity all sky maps. These signals are extremely difficult to identify and remove in post-processing and it was thus vital that the antenna itself minimized these signals as much as possible. This was achieved through three design features employed in the C-BASS telescopes: the feedhorn, the secondary reflector support struts, and very low edge illumination. The same feedhorn is used in both antennas, with the beam size matched by the secondary reflector. The corrugated feed horn was custom designed for suppressed sidelobe levels and low cross-polarization and consisted of a cosine-squared section and a cylindrical final section which was mounted directly onto the cryostat (Holler et al., 2013). The presence of support struts in the dish would have resulted in an increase in cross-polarization and an increase in scan-synchronous ground pickup. To counter this, the secondary mirror support structure was designed to work without support struts. Instead, a support structure in the form of a radio-transparent foam cone was used. Another option would have been to use an offset configuration, but this would have been expensive, especially since we already had the circularly symmetric dishes on hand. Finally, unwanted scan-synchronous signals can be introduced by signal spillover at both the primary and secondary mirror. This was limited in the northern system by placing absorbing baffles on both

reflectors, and in the southern system by under-illuminating the primary reflector to a high degree. Figure 2.3 is a schematic of the two optical configurations employed in the two C-BASS systems.

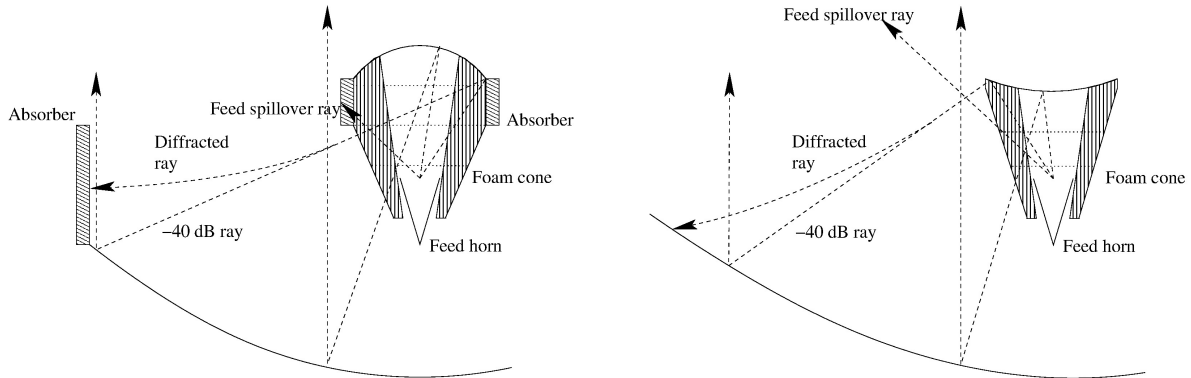


**Figure 2.3:** Schematic diagrams of the different optical configurations employed in the two C-BASS systems. The northern system, shown on the left, employed a Gregorian configuration while the southern system employed a Cassegrain configuration.

## 2.3 The C-BASS Receiver

The northern and southern receivers are very similar, resulting in a similar signal path in both instruments. The system is comprised of a cryogenic receiver, a warm radiometer and polarimeter, and a digital back end. In both systems we employ a continuous comparison architecture, where the sky signal is combined with a reference load signal to account for gain drifts in the signal path. In order to reduce the system temperature, the low noise amplifiers (LNAs) and pre-LNA components are cryogenically cooled. The signal enters the cryostat through the corrugated feed horn, mounted directly onto the cryostat body where a four probe orthomode transducer (OMT) detects linear polarization. The signal is passed via coaxial cables to a linear-to-circular converter (L2C) where it is converted into orthogonal circular polarizations  $E_R$  and  $E_L$ . Directional noise couplers are used to couple the left and right circularly polarized signal to that from a calibration noise source, in the form of a temperature stabilized reverse bias diode that produces an electron cascade with a broad band, flat, white noise spectrum. The polarized sky signals are

then combined with reference load signals  $E_{ref1}$  and  $E_{ref2}$ , generated from temperature stabilized matched loads, via a 180 degree hybrid. There are now four signals,  $(E_L \pm E_{ref1})/\sqrt{2}$  and  $(E_R \pm E_{ref2})/\sqrt{2}$ . These signals are then amplified and filtered before signal processing and measurement, which are implemented in separate ways by the different receivers. In the northern system, these signals are split into the radiometer and polarimeter branches of the signal chain, as shown in Figure 2.4, taken from King et al. (2014). In the southern system, the four signals pass through another stage of amplification and filtering before being down-converted and digitized, with the remaining processing taking place in the digital realm. Figure 2.5 is a simplified schematic of the southern C-BASS receiver taken from Copley (2013).

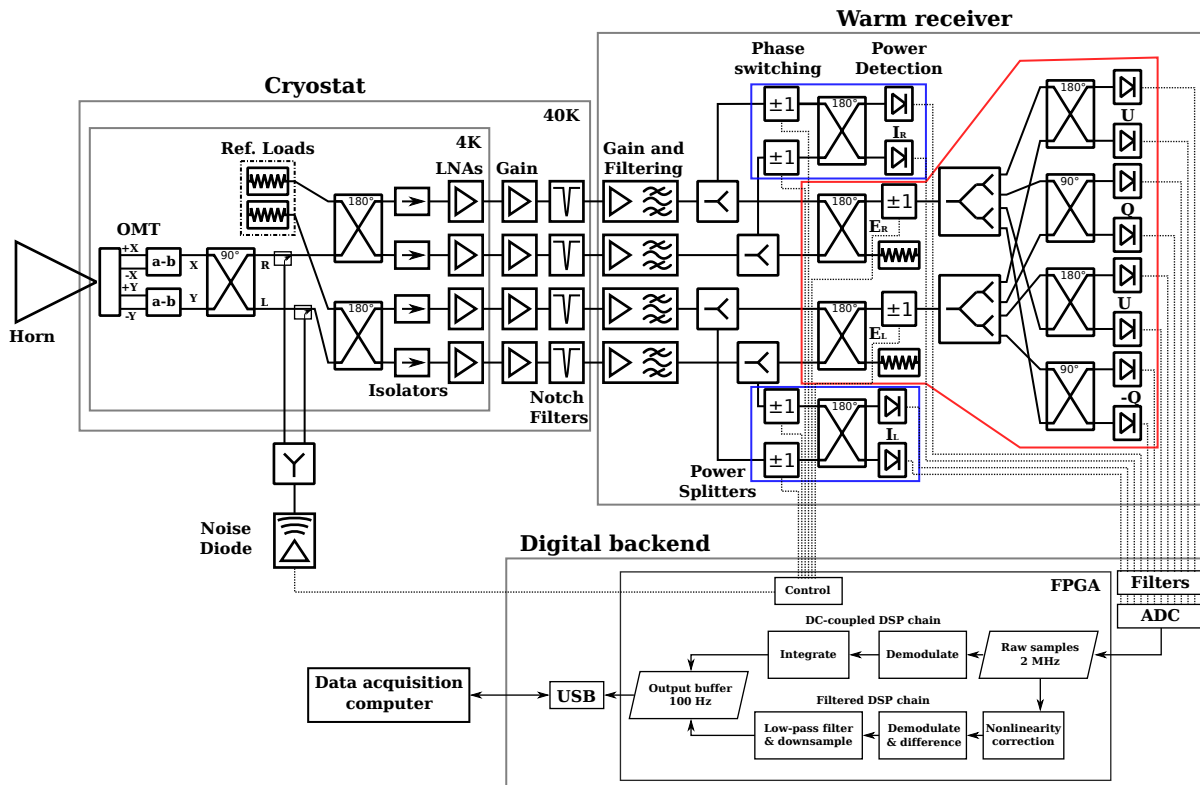


**Figure 2.4:** A simplified schematic diagram of the northern receiver showing the gain and filtering chains for the circular left (L) and right (R) polarized signals. The blue boxes show the intensity measurement (radiometer) and the red box shows the polarization measurement (correlation polarimeter). Taken from King et al. (2014).

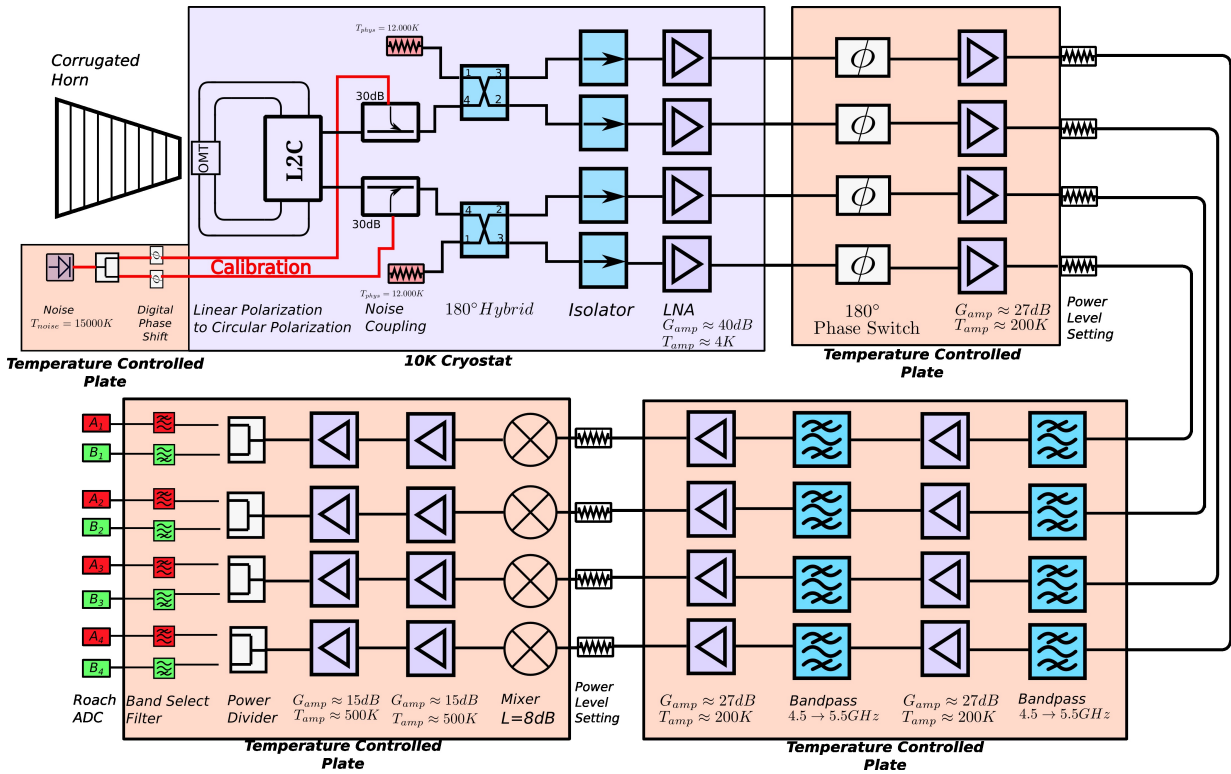


**Figure 2.5:** A simplified schematic diagram of the analog front end of the southern receiver showing the signal conditioning chain, as well as the down-conversion of the 1 GHz band into two 500 MHz bands, followed by analog to digital conversion. Taken from Copley (2013).

### 2.3.1 Cryogenic Front End

Both receivers use identical cylindrical cryostats with two-stage Gifford-McMahon coolers, but they have different cold heads with the northern receiver employing a Sumitomo Heavy Industries (SHI) SRDK-408D2 cold head with 4W of cooling at 4 K at its second stage, and the southern receiver using an Oxford Cryosystems Coolstar 6/30 providing 6 W of cooling at 10 K. The analog front end electronics, that is the OMT, L2C, noise diode RF couplers, 180 degree hybrids, reference cold load, and LNAs are mounted onto the second stage. Both receivers use LNF-LNC4.8A low noise amplifiers, which provide 40 dB of gain over 4–8 GHz with a noise temperature of 2–3 K. The 40 K second stage holds a second round of amplifiers and notch filters (northern system only) while the noise diode is mounted on the 300 K cryostat wall. Figure 2.6 shows photographs of the entire front end with the northern system shown on the left.



**Figure 2.6:** Photographs of the C-BASS cryostat, with the northern system on the left.

### 2.3.2 Total Intensity and Polarization Measurement

Both receivers are a combination of a continuous-comparison radiometer, measuring total intensity, and a correlation polarimeter, measuring linear polarization. The polarization state of an electromagnetic wave can be fully described using Stokes parameters. Stokes I characterises the total intensity, Stokes Q and U characterise linear polarization, and Stokes V characterises circular polarization. We measure Stokes I, Q and U by correlating left and right circular orthogonal modes. The Stokes parameters are related to left and right circular polarization electric fields by

$$I = E_L E_L^* + E_R E_R^* \quad (2.3)$$

$$Q = 2\text{Re}(E_L E_R^*) \quad (2.4)$$

$$U = -2\text{Im}(E_L E_R^*) \quad (2.5)$$

$$V = E_L E_L^* - E_R E_R^* \quad (2.6)$$

while for  $X$  and  $Y$  linear polarizations

$$I = E_X E_X^* + E_Y E_Y^* \quad (2.7)$$

$$Q = E_X E_X^* - E_Y E_Y^* \quad (2.8)$$

$$U = 2\text{Re}(E_X E_Y^*) \quad (2.9)$$

$$V = -2\text{Im}(E_X E_Y^*). \quad (2.10)$$

For pedagogical details, see Tinbergen (1996), amongst others.

With C-BASS, we wish to measure Stokes I, Q and U, that is, total intensity and linear polarization, but given that the polarized signal is extremely weak, it is prudent to perform the correlations shown in Equations 2.4 and 2.5, which are immune to amplifier  $1/f$  noise, as it is uncorrelated between amplifiers and therefore more sensitive than the differencing operations of Equations 2.8 and 2.9. Hence the conversion from linear to circular polarization in the signal chain.

### 2.3.2.1 Continuous Comparison Radiometer

In the C-BASS receiver, we implement a continuous comparison radiometer, shown in Figure 2.7 (b), for each of the two orthogonal circular polarizations. The continuous-comparison architecture allows one to account for gain variations in the signal chain while simultaneously measuring the sky signal. This is achieved by passing a known reference signal through the same gain chain as the sky signal and then comparing the sky and load signals afterwards. The signals are combined using a 180 degree hybrid which produces two new voltages with a 180 degree phase difference in the load voltage and are separated again after the gain stage with another 180 degree hybrid. The load signals for each polarization are provided by two temperature stabilized thermal loads,  $E_{ref1}$  and  $E_{ref2}$ . As the reference signals have been through the same gain fluctuations as the sky signal, we can difference the circular polarized signals and reference signals to find the true intensity measurement. The gain stabilized total intensity is thus

$$I = (E_L E_L^* - E_{ref1} E_{ref1}^*) + (E_R E_R^* - E_{ref2} E_{ref2}^*). \quad (2.11)$$

The continuous-comparison radiometer differs from the more conventional Dicke switch radiometer (Dicke, 1946), shown in Figure 2.7 (a), because a Dicke switch radiometer switches between the sky and a reference load, losing half its observing time. As such, the continuous-comparison radiometer achieves a factor of  $\sqrt{2}$  improvement in sensitivity.

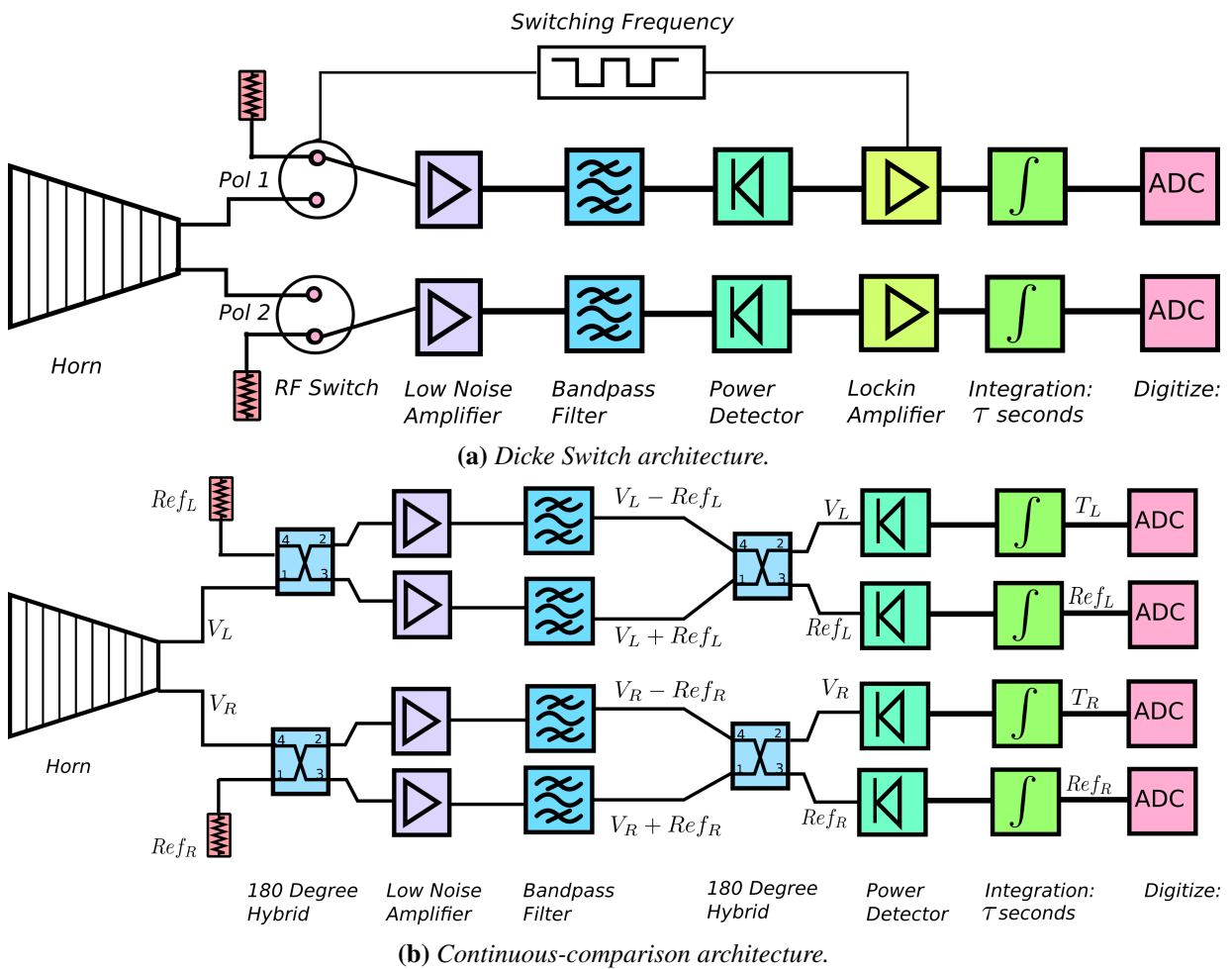


**Figure 2.7:** Examples of a Dicke switch and a continuous-comparison radiometer architecture. The continuous-comparison radiometer achieves a factor of  $\sqrt{2}$  improvement in sensitivity over the Dicke switch radiometer because it continually observes the sky. Taken from Copley (2013).

### 2.3.2.2 Correlation Polarimeter

The increased observation time afforded by the continuous-comparison architecture is especially beneficial to the measurement of polarization due to the increased sensitivity. As shown in Equations 2.4 and 2.5, polarization is measured by correlating the orthogonal circular polarized sig-

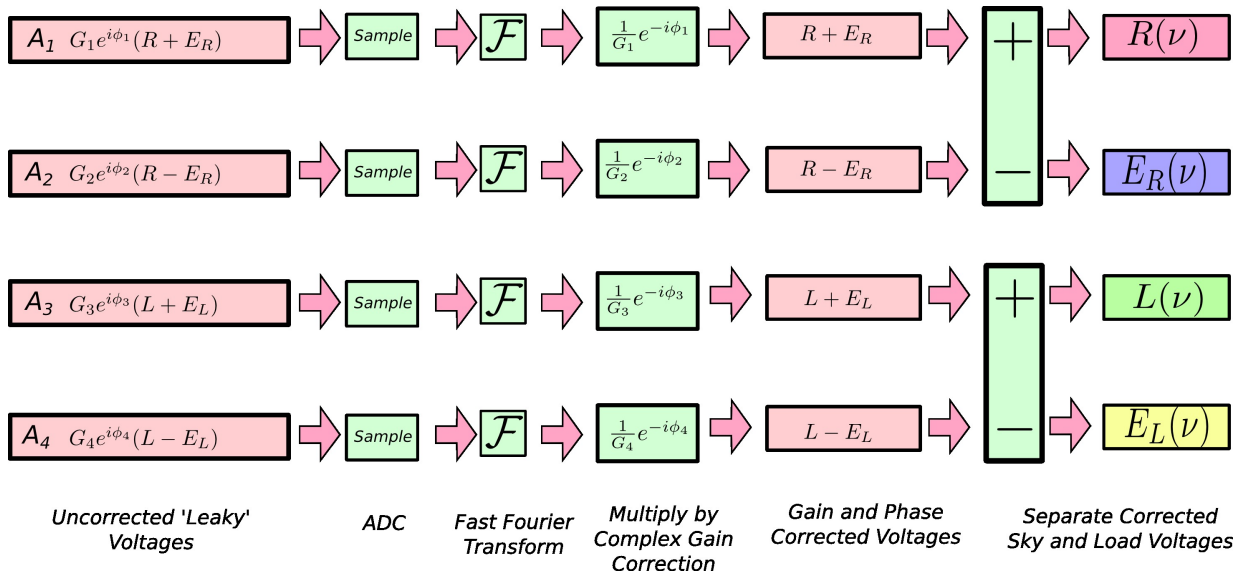
nals. This measurement is immune to gain drifts in the signal chains as these are uncorrelated. The reference signals are thus not used by the polarimeter, as they would simply add excess noise to the polarization measurement. In the northern system, the correlation is performed by a complex analog correlator made up of 90 degree hybrids and detector diodes, while in the southern system, it is performed in the digital back end

### 2.3.3 Back End Electronics

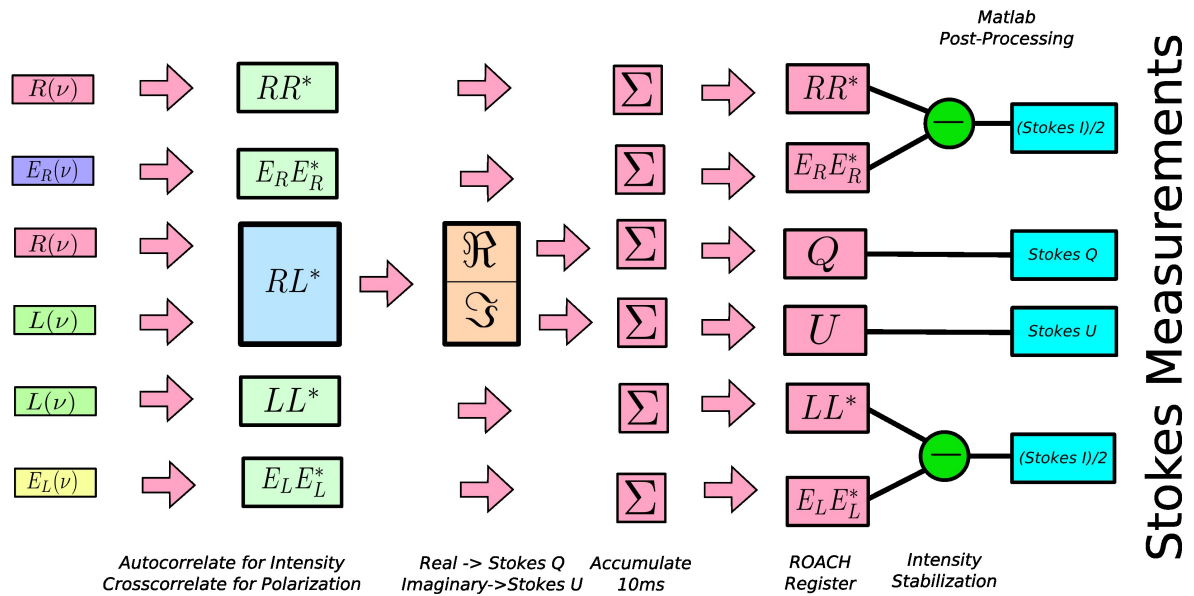
The biggest difference between the northern and southern receivers is in the back end electronics. The northern system employs analog electronics to perform the radiometer and polarimeter operations described previously on a single channel covering the entire measured bandwidth. The RF signal is converted to a power measurement using zero-bias Schottky detector diodes with a video bandwidth of around 800 kHz. For both the radiometer and the polarimeter, the RF signals are phase-switched, alternating the sky and load signals across the different gain paths. This is done to protect against noise introduced by the diode detectors. The detector outputs are sampled at 2 MHz, filtered and averaged down to 10 ms samples in a Xilinx Spartan 3 Field Programmable Gate Array (FPGA).

The southern system was built later and took advantage of new advances in digital processing hardware, allowing the southern receiver to have a digital back end. Thus all of the radiometer and polarimeter operations described previously are done with digital software, rather than analog hardware. This has the added advantage of providing spectral resolution within the band as the 1 GHz bandwidth is measured across 128 channels. The southern system employs an extra round of gain and bandpass filtering before mixing the four RF channels from the cryostat down to an IF baseband of DC–1 GHz, using a 4.5 GHz local oscillator. This 1 GHz band is then split into two 500 MHz sub-bands, one spanning DC–500 MHz and corresponding to the 4.5–5.0 GHz half of the RF band, and the other spanning 500–1000 MHz corresponding to the 5.0–5.5 GHz half of the RF band. Each sub-band is sampled by a 1 Gsps, 500 MHz bandwidth analog-to-digital (ADC) converter, with dual channel sampling and 8-bit resolution. The digital

signal processing in the southern receiver is performed by two ROACH boards, which are part of the Collaboration for Astronomy Signal Processing and Electronics Research (CASPER) hardware suite. The boards are based around a Xilinx Virtex 5 FPGA and each ROACH houses two ADC boards. The ROACHes carry out the signal processing operations matching those of the analog radiometer and polarimeter described previously. The digital processing chain consists of sampling and digitizing the analog signal, polyphase filtering and fast Fourier transforming the signal, gain and phase correction, sky and load signal separation, and finally Stokes I, Q and U detection. This process is illustrated in Figure 2.8. As with the northern system, the data are averaged over 10 ms and stored to disk.



(a) Analog signal is sampled, digitized, undergoes gain and phase correction and then the sky and load signals are separated.



(b) Stokes I auto correlations and Stokes Q and U cross correlations are performed in the ROACHes on 10 ms time integrated samples.

Figure 2.8: C-BASS south front end digital signal processing. Taken from Copley (2013).

# Chapter 3

## Data Reduction and Low-level Time Stream Processing

In this chapter, I will discuss the analysis of low-level time stream data from the northern telescope. The southern data analysis pipeline will be similar, but is currently still in its infancy and aspects thereof will be discussed in the final chapter.

### 3.1 The Time Stream Processing Pipeline

The C-BASS data analysis pipeline is a collection of data reduction scripts, formally based in MATLAB, with various functions calling to scripts written in C++, IDL, FORTRAN, and Python. The pipeline takes the raw data, stored in binary files, from the output of the ROACH, calibrates it, corrects systematic effects, flags bad data, and stores the clean, calibrated data in Flexible Image Transport System (FITS) format. The time ordered data is read in to the pipeline in the form of a six column array containing Stokes I, Q and U, and load data, as output by the FPGA (refer to Figure 2.4 in the previous chapter for details on how the raw data is produced and stored). The time stream processing pipeline consists of the following stages: complex gain correction, 1.2 Hz oscillation removal, radio frequency interference (RFI) removal, ground signal subtraction, pointing correction, astronomical calibration, and conversion to FITS file and stor-

age. These FITS files are then used to make maps, which will be discussed in Chapter 4. The order of the various processing steps in the pipeline is illustrated in Figure 3.1.

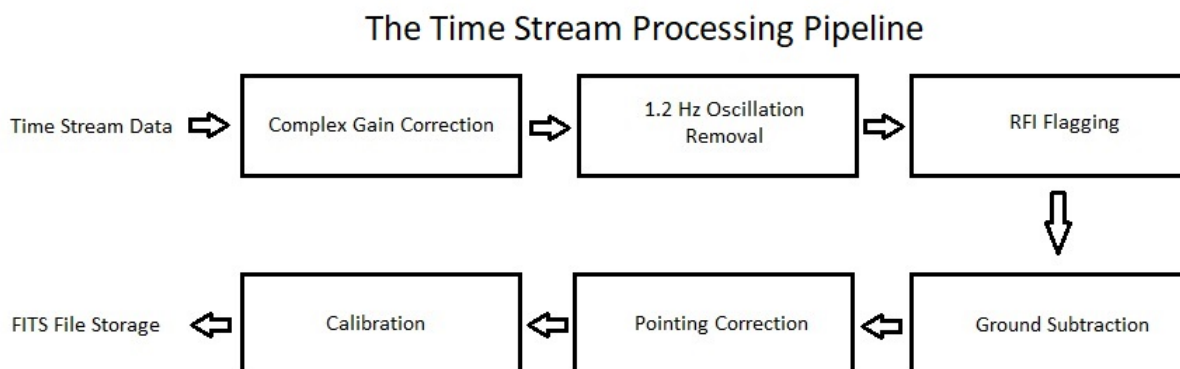


**Figure 3.1:** A flow chart showing the order in which the various steps in the time stream processing pipeline occur.

### 3.1.1 Complex Gain Correction

The complex gain correction stage uses noise diode events to apply a complex gain correction to the data. A noise diode is fired every four minutes during standard schedule observations. The purpose of this noise diode event is to provide a signal of known value, which can be used to calibrate the data and counter gain drifts. The complex gain correction value, scales the data so that the noise diode events equal unity, and by interpolating the magnitude of the correction value over the entire schedule, we are able to correct any gain drifts that occurred during the schedule. The correction value also has a phase component, to be used in identifying and correcting polarization signal leakage. The noise diode signal is added to the Stokes I and Q channels, but not to the U channels. Thus, any noise diode signal found in the U channels affects the phase of the correction value, which can then be used to correct that leakage.

### 3.1.2 1.2 Hz Oscillation Removal

The cryogenic pump that cools the northern cryostat operates with a 1.2 Hz periodic cycle, with the unfortunate side effect of producing microphonic oscillations at 1.2 Hz and its harmonics. These oscillations are picked up by the receiver and are consequently introduced into our data. The 1.2 Hz oscillation removal stage of the data analysis pipeline is responsible for removing these oscillations from our data. This work is ongoing and the problem has not yet been completely solved, but the general idea is to remove the oscillations with template fitting. A template for the 1.2 Hz oscillations over the course of a schedule is made by analysing the temperature fluctuations of the cold load. This template is then subtracted from the data, leaving it less affected by the oscillations.

### 3.1.3 RFI Flagging

Radio Frequency Interference (RFI) is the term used to describe unwanted man-made signals in the data. RFI signals are usually very bright, are often polarized, and can either be narrow- or broadband in nature. They emanate from various sources, including WIFI routers, mobile telephones, aircraft, and satellites. The presence of RFI, whether in-band or bright out-of-band sources, is an unavoidable fact for most ground based, single dish radio telescopes, and C-BASS is no exception. As discussed in the previous chapter, some of the more persistent RFI contamination in the northern survey was addressed in hardware with the use of notch filters. The remaining RFI signal is addressed in this section of the time stream processing pipeline. The role of the RFI flagging routine is to identify parts of the data that have been affected by RFI, and flag them, so that they do not appear in our final maps.

The true sky signal, as opposed to RFI, is very consistent and does not change on the time scale of our observations. This means that over time, as more data is taken, the RFI signal averages down when compared to the signal from the sky. Thus, the averaged sky signal from our data provides us with a model of the expected sky signal. We can compare the sky signal from

a particular sample of time ordered data (TOD) to the expected sky signal from our full data set, projected into the time domain of the TOD sample, and then flag the parts of the signal that do not match as RFI. This process is iterative, and with each repetition of running the full data set through the flagging routine, more RFI is removed, resulting in an improved data set and thus an improved estimate of the expected sky signal for the next iteration. At this point, we have only performed one iteration. The expected sky signal is stored as a Hierarchical Equal Area iso-Latitude Pixelization (HEALPix) map. These maps store data on a map in pixels of equal area, where the resolution, or number of pixels, of the map is defined by the  $N_{side}$ , where the number of pixels is given by  $12N_{side}^2$ . For a detailed explanation of the HEALPix data structure, the reader is referred to Gorski et al. (1999) and Górski et al. (2005) as well as subsequent revisions.

We project the expected sky signal into the time domain by using the Coordinated Universal Time (UTC), azimuth and elevation information of the time ordered data in question to determine the right ascension and declination of the sky. This can then be converted to pixel number and the expected sky signal of the time stream data is formed by pulling data from those pixel numbers in the correct order. I refer to this as the nearest pixel method as we determine the pixel number that is closest to the given right ascension and declination. The resolution of the expected sky signal map is important when producing an expected TOD sky signal, as a low resolution means that the pixels average over a large area. Thus several consecutive time ordered data elements would correspond to the same pixel, resulting in a discretized expected TOD sky signal. It is possible to use a lower resolution map and interpolate the nearest pixels to produce a smoother expected TOD sky signal. A comparison between the nearest pixel method and the interpolation method, both produced using an  $N_{side}$  512 map, is shown in Figure 3.2. Note the steps in the expected TOD sky signal produced by the nearest pixel method, illustrating that the resolution of the map used was too low.

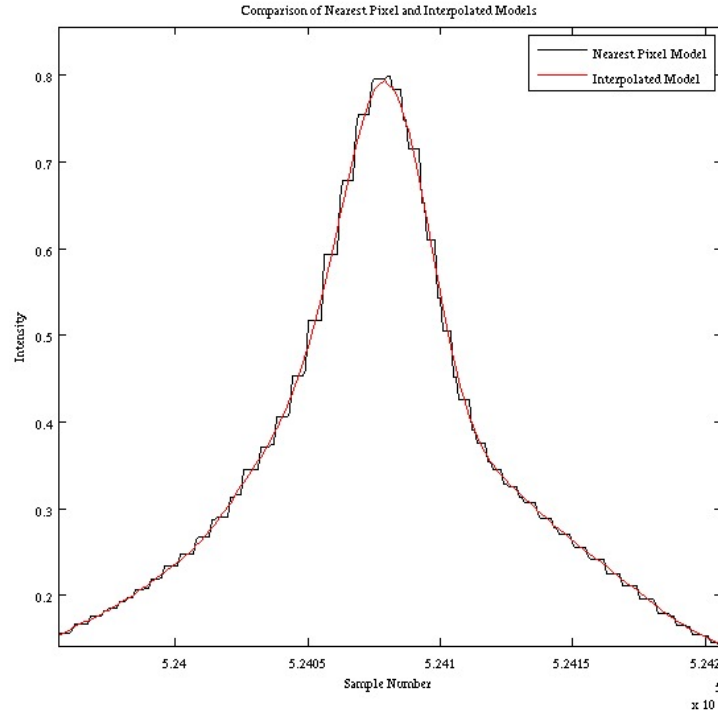


**Figure 3.2:** A plot showing a comparison between the nearest pixel expected TOD sky signal in black (denoted as ‘Nearest Pixel Model’) and the interpolated one in red (denoted as ‘Interpolated Model’) for a single source crossing. Both of these methods used an expected sky signal map stored in a HEALPix map with  $N_{\text{side}}$  512 resolution. This plot illustrates the discretization resulting from the nearest pixel method being used with a low resolution map.

Interpolating an  $N_{\text{side}}$  1024 map was found to be sufficient when matching the expected TOD sky signal to the data. For the nearest pixel method, we decided to increase the resolution to  $N_{\text{side}}$  4096. This method should result in a large time saving as we have effectively already interpolated the entire map, rather than having to interpolate during the pipeline run for each individual TOD. We found that even though the interpolation used a smaller map, it was still slower than the nearest pixel method by a factor of around two. Thus, the nearest pixel method was adopted, using an  $N_{\text{side}}$  4096 map. While such a large resolution map is not strictly necessary, given the size of our beam, we wished to avoid pixelization artifacts when sampling signal-only time streams. This was achieved by using a high resolution  $N_{\text{side}}$  4096 map at the minor cost of using more computer memory. Figure 3.3 shows that interpolating an  $N_{\text{side}}$  1024 map produces an

expected TOD sky signal that is effectively the equivalent of that produced by using the nearest pixel method with an  $N_{\text{side}} 4096$  map. The  $N_{\text{side}} 4096$  map that we finally used as our expected sky signal is shown in Figure 3.4.

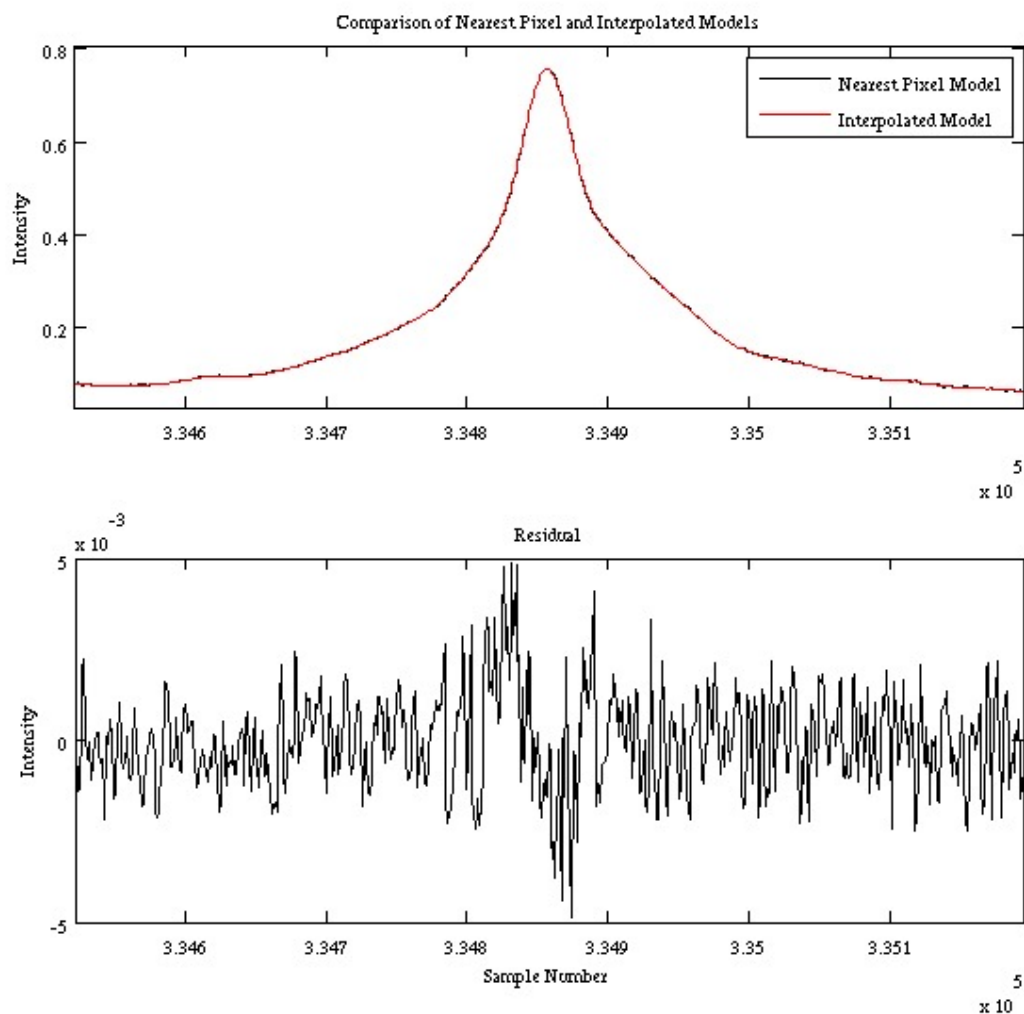


**Figure 3.3:** A comparison of the two methods of generating an expected TOD sky signal for a single source crossing. The top panel shows the nearest pixel method, in black (denoted as ‘Nearest Pixel Model’), which used an  $N_{\text{side}} 4096$  HEALPix map, and the interpolated method, in red (denoted as ‘Interpolated Model’), which used an  $N_{\text{side}} 1024$  HEALPix map. The bottom panel shows the difference between the plots resulting from the two methods.

We modelled the time ordered receiver data as a sum of three terms,

$$M\alpha + G\beta + \kappa, \quad (3.1)$$

where  $M$  is the expected sky signal,  $G$  is the ground contamination signal,  $\alpha, \beta$  are arbitrary coefficients, and  $\kappa$  is an arbitrary offset. Both  $M$  and  $G$  are projected into the time domain using map templates and the C-BASS scan strategy. By performing a linear least squares fit of the TOD against the model, we obtain estimates for the parameters  $\alpha, \beta, \kappa$ .

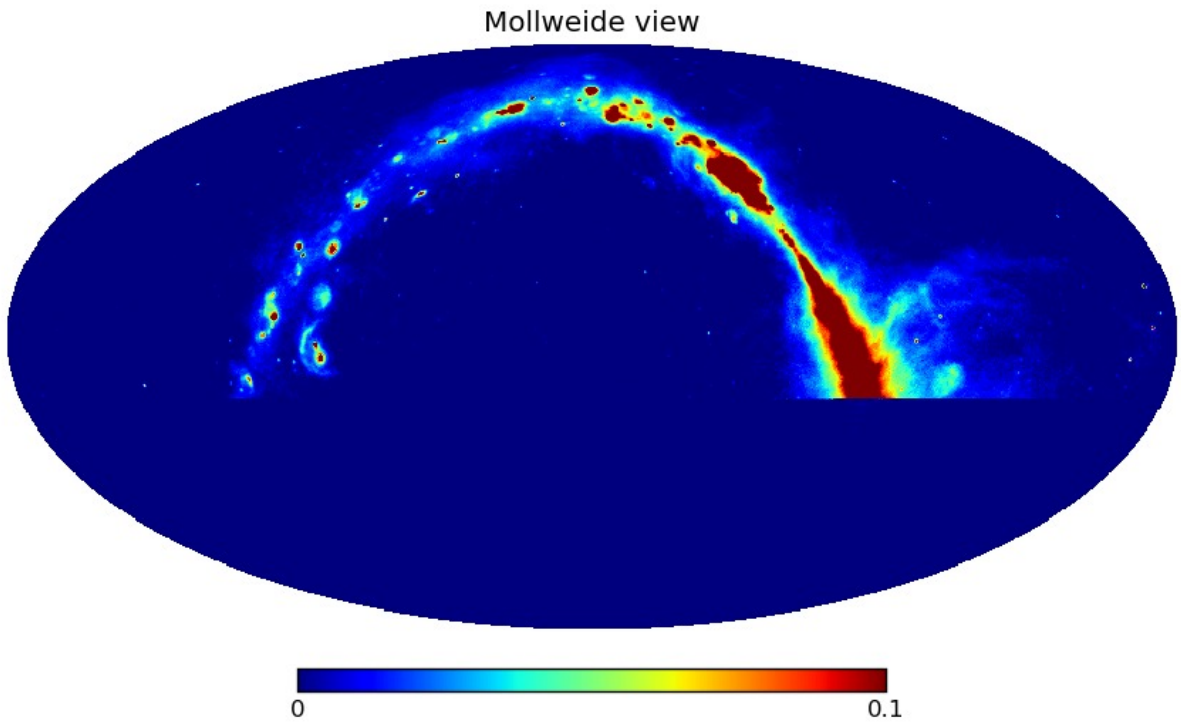


**Figure 3.4:** An  $N_{\text{side}} 4096$  HEALPix map of our entire data set in Stokes  $I$  in units of Kelvin. This map was used to model the expected sky signal.

RFI was identified by applying the following metric:

$$\frac{|D - (M\alpha + G\beta + \kappa)|}{\sigma} \geq \eta \quad (3.2)$$

where  $D$  is the data and  $\sigma$  is the RMS of the residual (the difference between the data and the expected TOD sky signal), which encompassed the noise associated with both data and model.

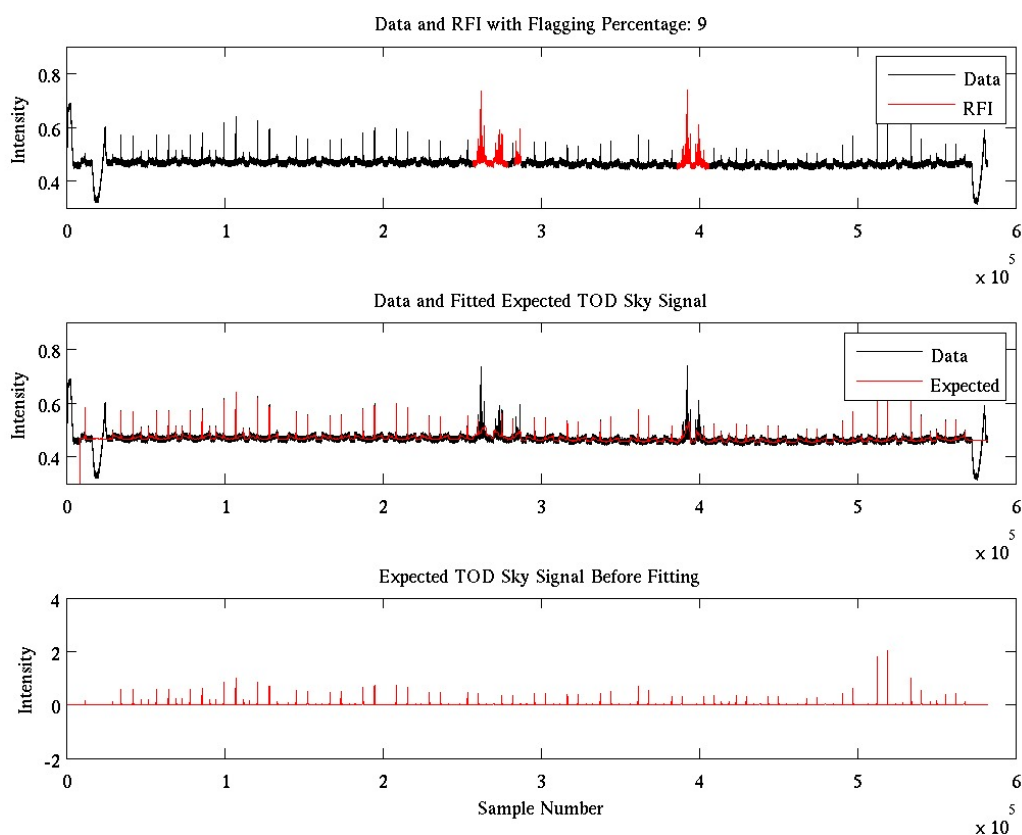
The cut-off value  $\eta$  began at 6 and was decreased iteratively by 0.5 as the following process was repeated:

- Any element for which the result of Equation 3.2 was greater than  $\eta$  was flagged as RFI.
- The skewness and kurtosis of the histogram of the residual, excluding data flagged in previous iterations, were evaluated.
- If the skewness was above 0.1 or the kurtosis was above 4, the value of  $\eta$  was decreased. This process was repeated until the skewness and kurtosis criterion were satisfied, or more than 50 % of the data had been flagged, at which point the entire scan would be flagged as RFI.
- The final step in flagging RFI was to flag 3 seconds of data on either side of an identified RFI event to ensure that all trace of the event had been removed from the data.

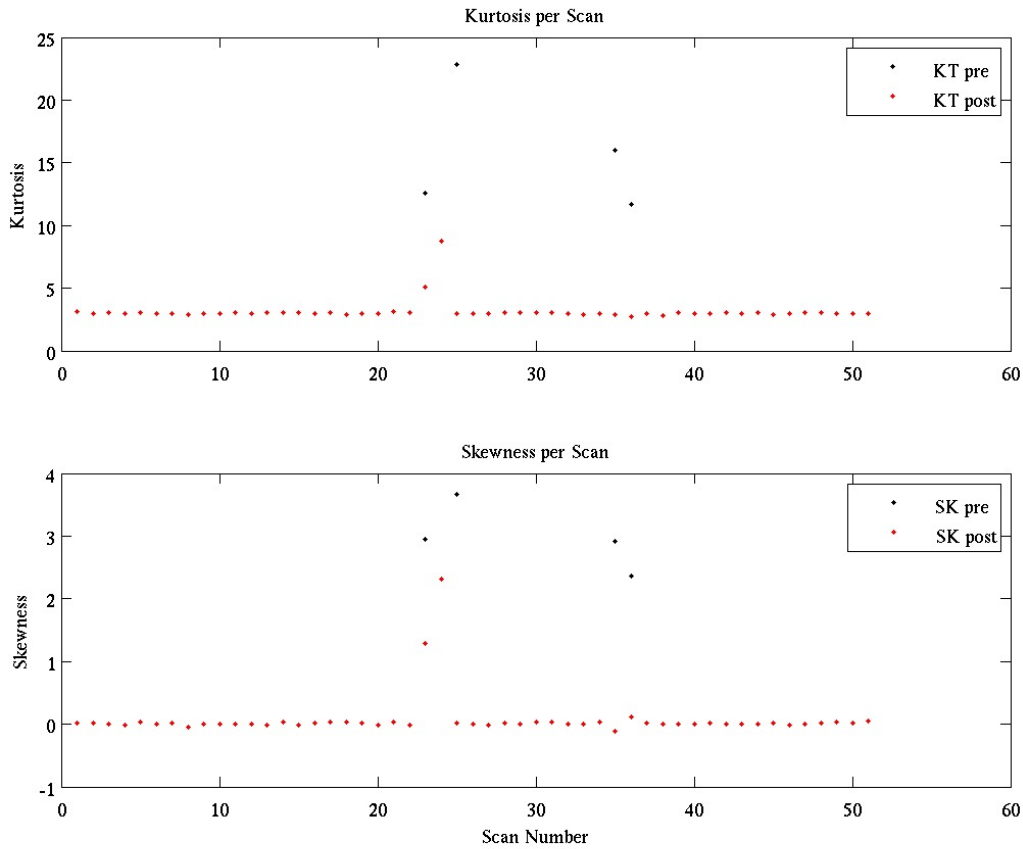
In an attempt to achieve a clean data set that would pass the suite of self-consistency tests, to be discussed in Chapter 4, we adopted a very aggressive approach to flagging RFI. This meant that the skewness and kurtosis limits were very strict, and any scans that could possibly still contain any RFI after flagging were just completely flagged. We expect the histogram of the residual, once all the RFI has been removed, to have a normal distribution. The skewness is a measure of how skewed the distribution is towards the left or right and the kurtosis is a measure of whether most of the data in the distribution is near the centre or in the tails. The skewness and kurtosis limits were chosen by interrogating a range of schedules. We found that a skewness of 0.1 and a kurtosis of 4 were typical for schedules where RFI was absent. Where RFI was present, these values were significantly higher. The initial  $\eta$  value of 6 was chosen as only data with zero RFI would pass the skewness and kurtosis tests at this value. The interval for decreasing  $\eta$  after each iteration was chosen to be 0.5 as higher values were too coarse and lower values required more iterations and therefore took longer. Note that the terms  $D$ ,  $M$ , and  $G$  are all time ordered. The time dependence has been suppressed in Equations 3.1 and 3.2 for the sake of clarity.

The northern survey scan strategy consisted of full azimuth scans at constant elevation, where the telescope would sweep back and forth a full 360 degrees in azimuth at one of four constant elevations, namely 37, 47, 67, and 77 degrees. Each observation schedule lasted about 1.5 hours, and consisted of multiple full azimuth scans in both directions. For a full description and example of the C-BASS north survey schedules, please refer to Figure 2.2 and the paragraph that precedes it in section 2.1.2 in Chapter 2. The expected TOD sky signal was fitted to the data on single direction azimuth scans. This was a natural scale to chunk the data on as there is no meaningful sky signal on longer time scales, and it provided protection against gain drifts and atmospheric fluctuations. This also avoided the possibility of a single massive RFI event upsetting the fit for an entire schedule. Calibration operations such as sky dips, which occur at the beginning and end of each observation schedule, and the firing of the noise diode are not included in the final data product, and so it was not necessary to apply the RFI flagger to such events. The sun and moon are also identified in the data and can be removed. In order to avoid flagging during these events, a mask was used to cover them, resulting in the flagging routine only being applied to survey data.

Here follows an example of the RFI flagging routine at work. Consider a typical survey schedule, shown in Figure 3.5, where the top panel shows the time stream data from the entire schedule, with RFI events coloured in red, the middle panel shows the expected TOD sky signal, in red, fitted to the time ordered data, and the bottom panel shows the original expected TOD sky signal before fitting. During the flagging process, this schedule is split into single azimuth scans and the model is fitted according to Equation 3.1. The iterative routine of applying Equation 3.2 and evaluating the resulting kurtosis and skewness is applied and the RFI is flagged. The skewness and kurtosis before and after flagging are shown in Figure 3.6.



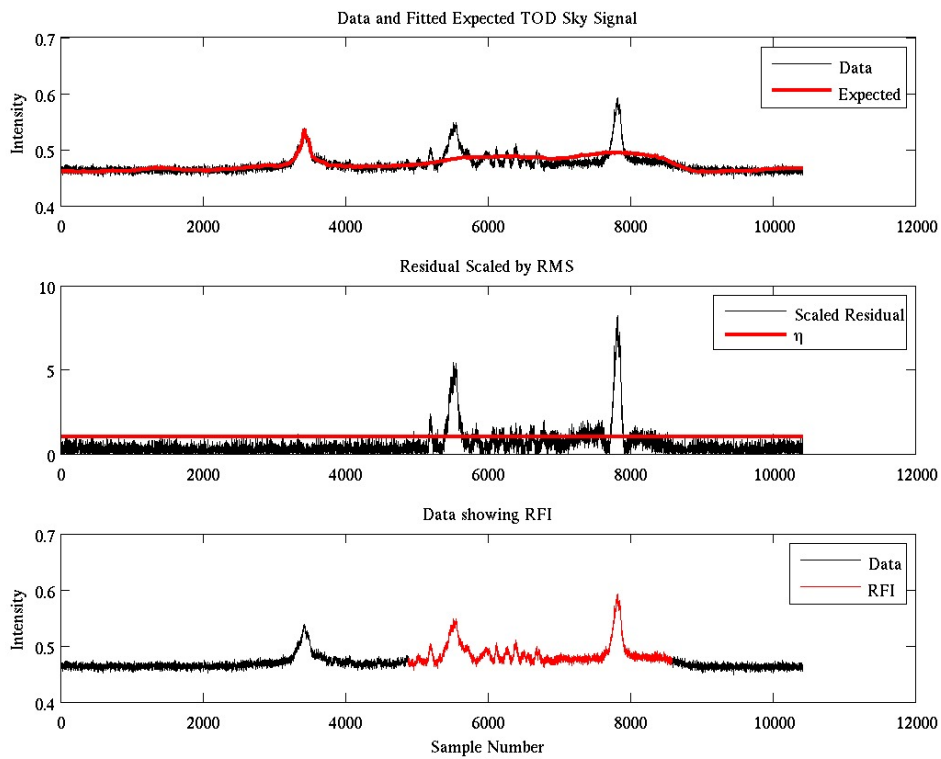
**Figure 3.5:** A comparison between the expected TOD sky signal and the time ordered data for a typical 1.5 hour survey schedule. The top panel shows the time ordered data in black and the data flagged as RFI in red. The middle panel shows the time ordered data in black and the fitted expected TOD sky signal in red. Note how the areas where these two lines do not match have been identified as RFI in the top panel. Also note that the sky dips at the beginning and end of the schedule have been ignored by the RFI flagging routine. The bottom panel shows the original expected TOD sky signal before it has been fitted to the data.



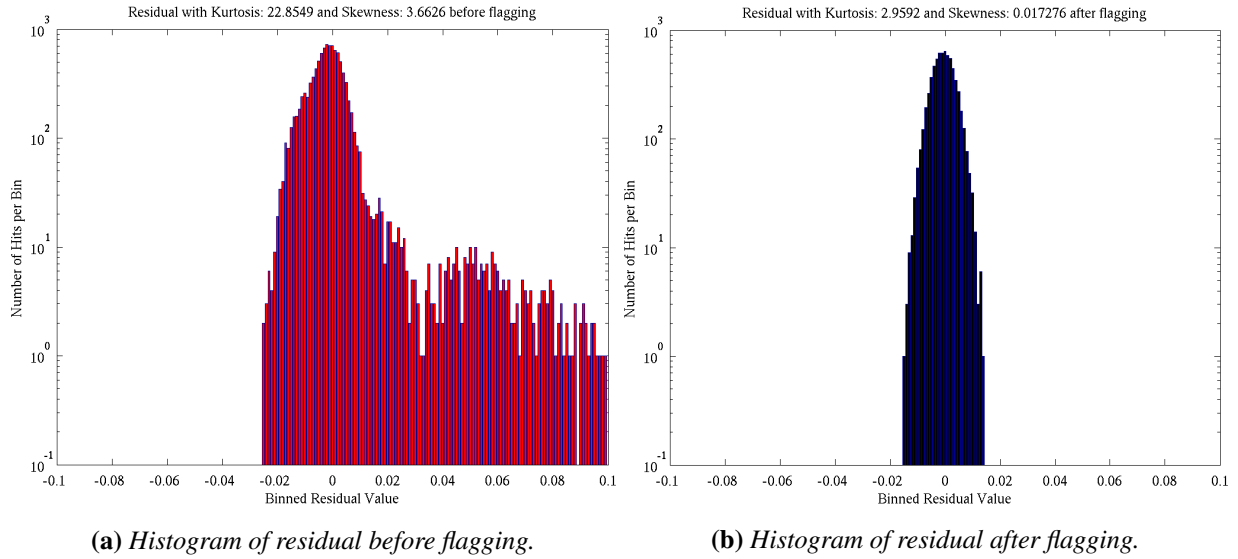
**Figure 3.6:** *The skewness and kurtosis of the residual of each azimuth scan in a typical survey schedule. The top panel shows the kurtosis before flagging in black, and after flagging in red. The bottom panel shows the same for skewness.*

Now consider a single azimuth scan within the full schedule, shown in Figure 3.7. With a scan speed of 4 degrees per second, each azimuth scan lasts just over 90 seconds, taking speed changes during scan direction change into account. This particular scan experienced a large RFI event. The top panel shows the expected TOD sky signal in red fitted to the time ordered data in black. This particular sample of time ordered data contained a Galaxy crossing, as well as two bright RFI spikes and some smaller RFI spikes. The middle panel shows the result of applying the metric in Equation 3.2, with  $\eta$  having been reduced all the way down to a value of 1 before the skewness and kurtosis criterion were satisfied. Note how the RFI affected data stands out above the red cut off line  $\eta$ . The data above this line was all flagged as RFI, along with 3 seconds

of data on either side of the RFI events. The bottom panel shows the time ordered data in black with the flagged RFI signal in red. Figure 3.8 shows the histograms of the residual of the data and the fitted expected sky signal before and after flagging. Note that the y-axis is on a logarithmic scale in order to highlight bins with few hits. This is done to show the RFI events more clearly in the histogram. The figure clearly shows that the RFI event has been effectively excised from the data, leaving a Gaussian histogram and reducing the skewness from over 3 to 0.02 and the kurtosis from over 22 to below 4.



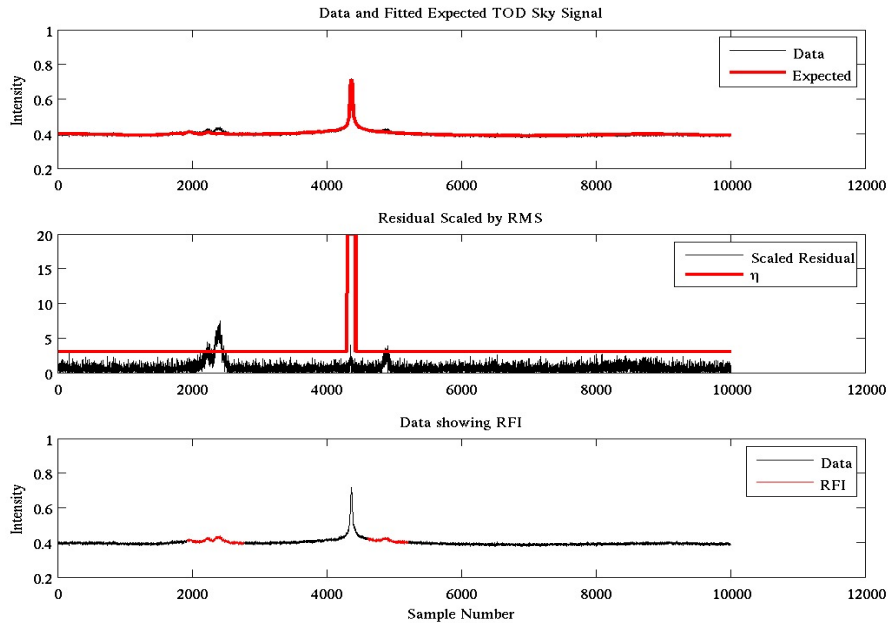
**Figure 3.7:** A comparison between the expected TOD sky signal and the time ordered data for a large RFI event. This plot shows data from a single azimuth scan lasting around 1.5 minutes. The top panel shows the time ordered data in black and the fitted expected TOD sky signal in red. The data includes a Galaxy crossing and a large RFI event consisting of two large peaks and several smaller peaks. The middle panel shows the result from Equation 3.2 in black and the cut off line  $\eta$  in red. Note that the RFI affected data stands out above the red line. The bottom panel shows the time ordered data in black and the RFI affected data in red.



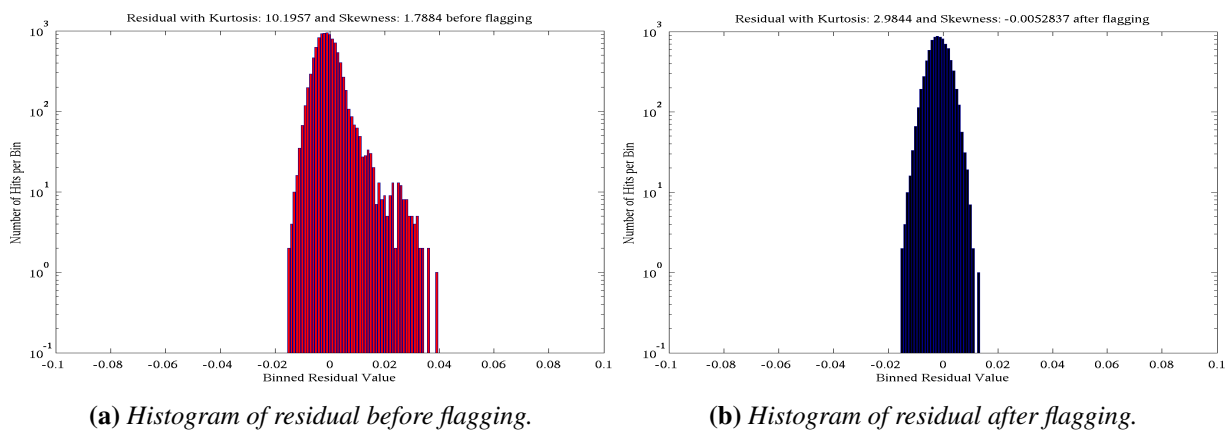
**Figure 3.8:** Histograms of the residual of the data and the fitted expected sky signal before and after RFI flagging. The y-axes have been plotted on a logarithmic scale to highlight bins with few hits.

Figure 3.9 shows a single azimuth scan that experienced a small RFI event. Note that for this event, the skewness and kurtosis criterion were satisfied much earlier and  $\eta$  remained at 3. Figure 3.10 shows the residual histogram before and after flagging. This particular scan contained a source, which was automatically identified in the expected TOD sky signal. In order to avoid flagging sources, a ‘top hat’ is used in the  $\eta$  cut off. This is necessary due to small pointing inaccuracies, but is not ideal as RFI close to or on a source could get through the flagging routine. A collaboration member is currently investigating these small pointing errors, and this part of the flagging process will be refined in future versions of the flagging routine.

Figure 3.11 shows a single azimuth scan experiencing a large RFI event. This event could not be completely flagged by the flagging routine, and the skewness and kurtosis criterion could not be satisfied. As a result, the entire scan was flagged.



**Figure 3.9:** A comparison between expected TOD sky signal and time ordered data for a small RFI event. This plot shows data from a single azimuth scan lasting around 1.5 minutes. The top panel shows the time ordered data in black and the fitted expected TOD sky signal in red. The data includes a bright source crossing and two small RFI events. The middle panel shows the result from Equation 3.2 in black and the cut off line  $\eta$  in red. Note that the RFI affected data stands out above the red line and that the red line avoids flagging the source by applying a ‘top hat’. The bottom panel shows the time ordered data in black and the RFI affected data in red.



(a) Histogram of residual before flagging.

(b) Histogram of residual after flagging.

**Figure 3.10:** Histograms of the residuals before and after RFI flagging. The y-axes have been plotted on a logarithmic scale to highlight bins with few hits.

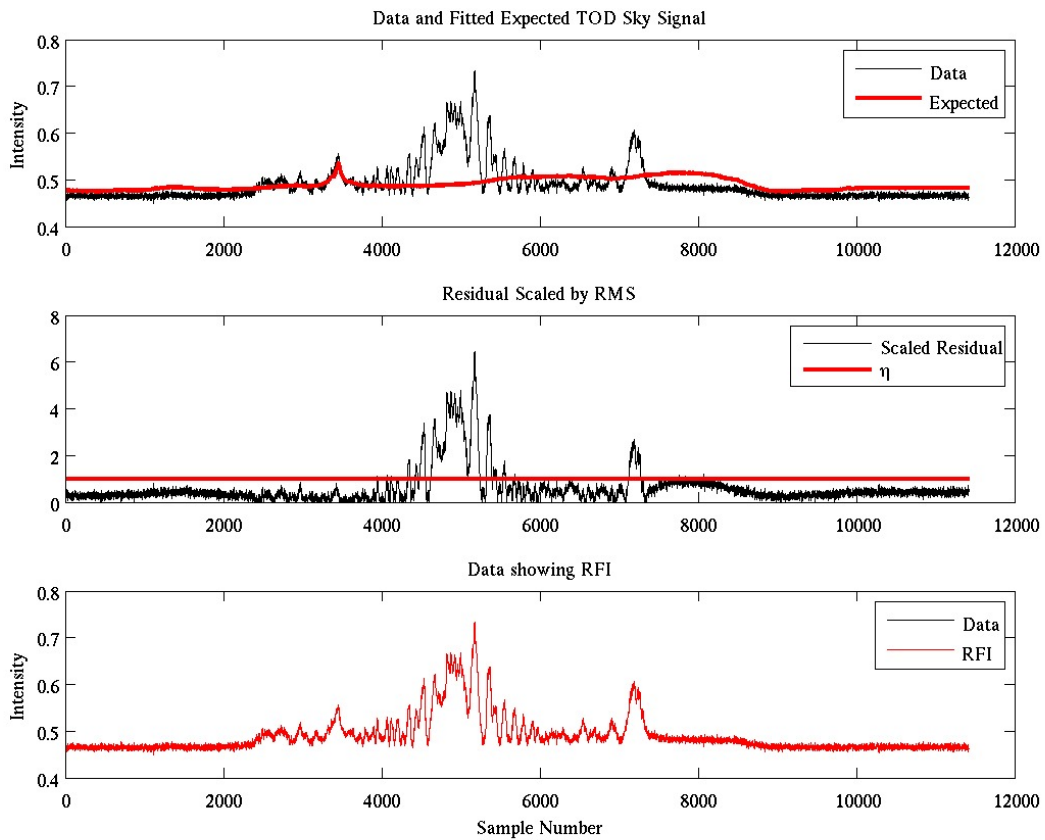


**Figure 3.11:** A comparison between the expected TOD sky signal and the time ordered data for a very large RFI event. This plot shows data from a single azimuth scan lasting around 1.5 minutes. The top panel shows the time ordered data in black and the fitted expected TOD sky signal in red. The middle panel shows the result from Equation 3.2 in black and the cut off line  $\eta$  in red. Note that the RFI in this TOD was so bad that the skewness and kurtosis criterion were never satisfied. As a result, the bottom panel shows that the entire TOD was flagged as RFI.

The data reduction pipeline stores the reduced data output in FITS files, to be mapped using the appropriate software. Figure 3.12 shows maps of a single schedule before and after flagging, as well as the difference between them, which highlights the flagged RFI. Similarly, we can look at maps of an entire day's data before and after flagging, as seen in Figure 3.13. These maps were produced using a destriping map making tool called the DESTriping CARTographer (DESCART), which was developed by Sutton et al. (2009, 2010). DESCART and our other map making tool, Ninkasi, described by Fowler et al. (2010) and Dünner et al. (2013), are discussed

in detail in Chapter 4.

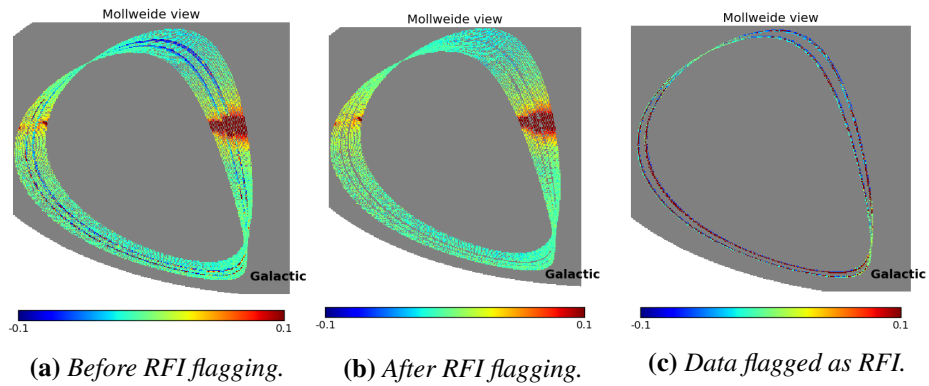


**Figure 3.12:** Mollweide projection maps of a single 1.5 hour survey schedule before and after RFI flagging, as well as the data flagged as RFI. The temperature scale is Kelvin.

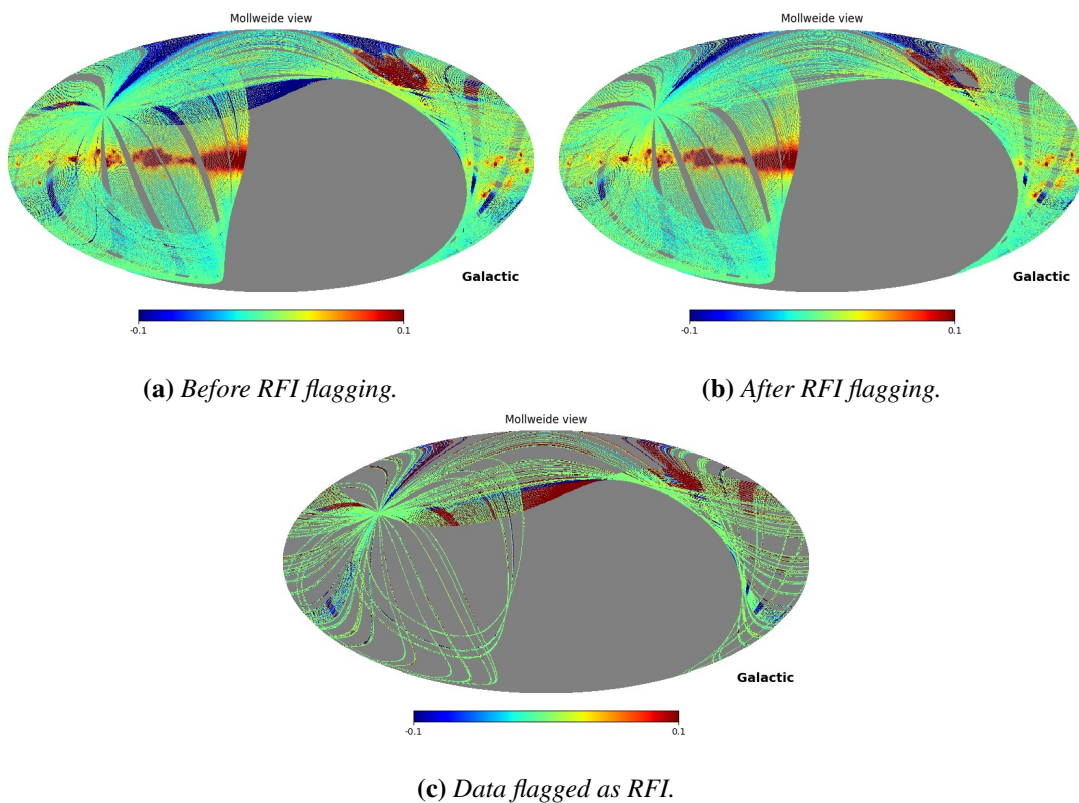


**Figure 3.13:** Mollweide projection maps of an entire day before and after RFI flagging, as well as the data flagged as RFI in units of Kelvin. The large blue streaks still present in plot (b) are most likely due to the calibration or ground removal (post RFI flagging) having difficulty with the presence of the sun.

It can be seen that all traces of RFI in Figure 3.13 have been flagged but the sky sources have been left untouched. The large blue streaks that are still present in plot (b) are there because that particular schedule tracked through the sun multiple times. Previous versions of the RFI flagging routine flagged the sun and moon, but my flagging routine ignores them because we are able to flag the sun and moon separately during the mapping process and some collaboration members have expressed an interest in studying the sun in our data. I believe that the presence of extremely bright solar radiation in the data has affected either the calibration or the ground removal process as this was not something that either routine had to deal with when the previous RFI routines were in use. This is something that will have to be investigated further. The RFI flagging routine proved to be highly successful at removing spurious RFI signals from the data while leaving true sky signal untouched. Previous attempts at removing RFI from C-BASS data had been far less precise in their identification of RFI signals, often flagging true sky sources such as TauA. The new flagger was also significantly faster than the old method. In previous versions of the data reduction pipeline, the RFI routine had been the easily the slowest part and it is now noticeably one of the fastest. For example, Figure 3.14 shows a comparison between the new flagging routine and the old method. The new routine took just under 12 seconds to flag the RFI in this schedule, the old routine took over 380 seconds and ended up flagging almost all of the signal because the ground contamination was not correctly taken into account. Apart from the ground signal, the old routine also flagged some weak sources. In fairness, the old method was incomplete and the collaboration member who had worked on it left the collaboration shortly after I began working on C-BASS. It was decided to pursue a new RFI flagging method after this collaboration member had left.

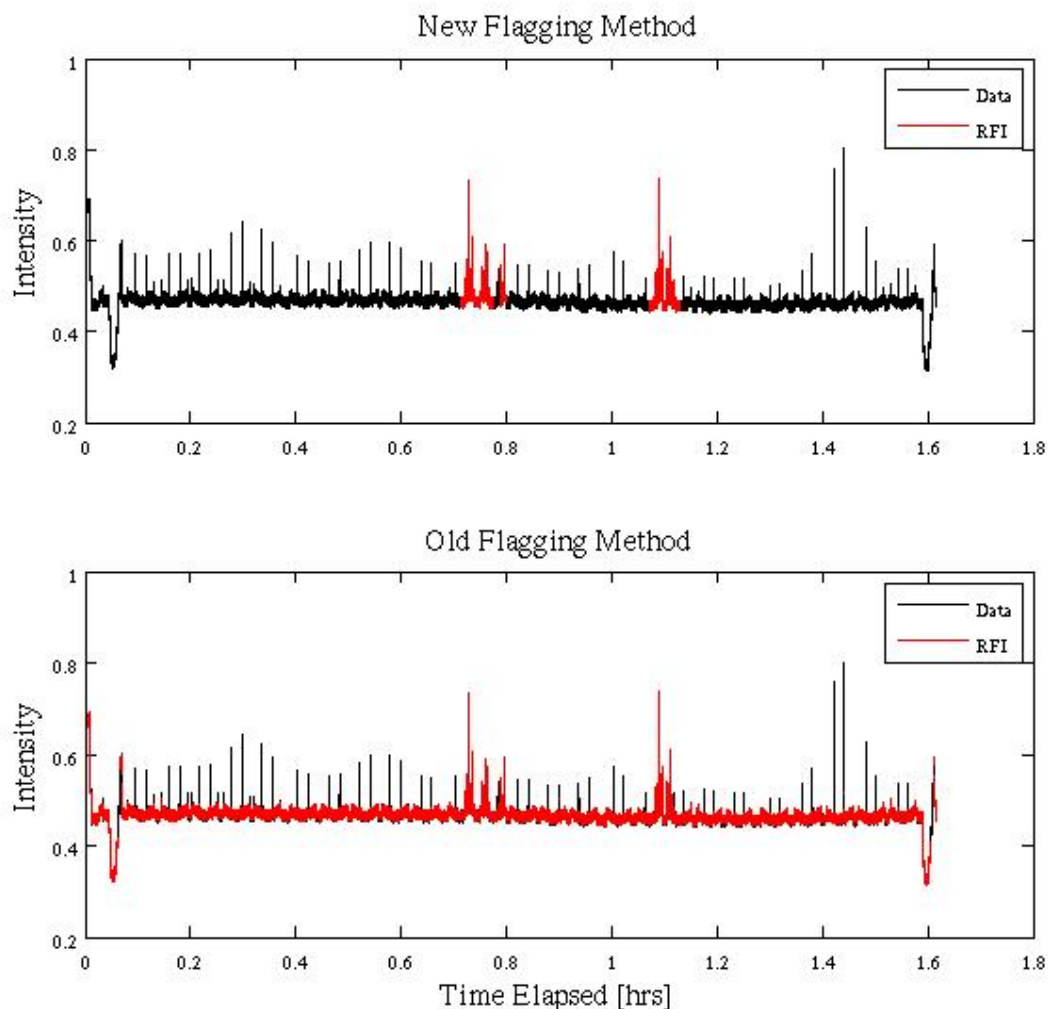


**Figure 3.14:** A comparison between the new and old RFI flagging routines. The new routine took 12 seconds to analyse this data, while the old method took over 380 seconds and failed to take the ground signal into account. It can also be seen that some weak sources were incorrectly flagged by the old routine.

The following is a more qualitative example of the RFI flagging routine at work. Special schedules were conducted to measure RFI in the area. These schedules consisted of complete azimuth scans separated by discrete 0.5 degree increases in elevation, generally from 15 to 85 degrees in elevation. Maps produced from these schedules, called azimuth-elevation maps, provide a useful way to visualize both the presence of RFI and the effectiveness of the RFI flagging

routine. Unfortunately, the ground signal could not be accounted for when flagging these scans as the elevation kept changing and we only have ground templates for our survey elevations, as shown in Figure 3.16. I therefore had to remove the ground scaling term from the fitting algorithm (Equation 3.1) when investigating these schedules. This resulted in a poorer fit for these schedules and as a consequence, I had to relax the flagging criterion quite considerably. Figure 3.15 shows azimuth-elevation plots with and without flagging where the plots in the top row show the data before RFI flagging and those in the bottom row show the data after the RFI has been flagged. The plots on the left have no Galaxy present but show how the sun is ignored by the flagger and the plots on the right show how the RFI has been flagged, but the Galaxy remains untouched. The vertical line around azimuth 340 degrees is the noise diode, the large sources at low elevations near azimuth 50 and 250 degrees are ground reflections while those near azimuth 120 and 325 degrees are RFI sources. The advantage of plots like these is that they show the position of the RFI sources in azimuth and elevation, which allows us to differentiate between sky and ground based RFI sources, and could allow us to realise if certain RFI sources consistently evade flagging.

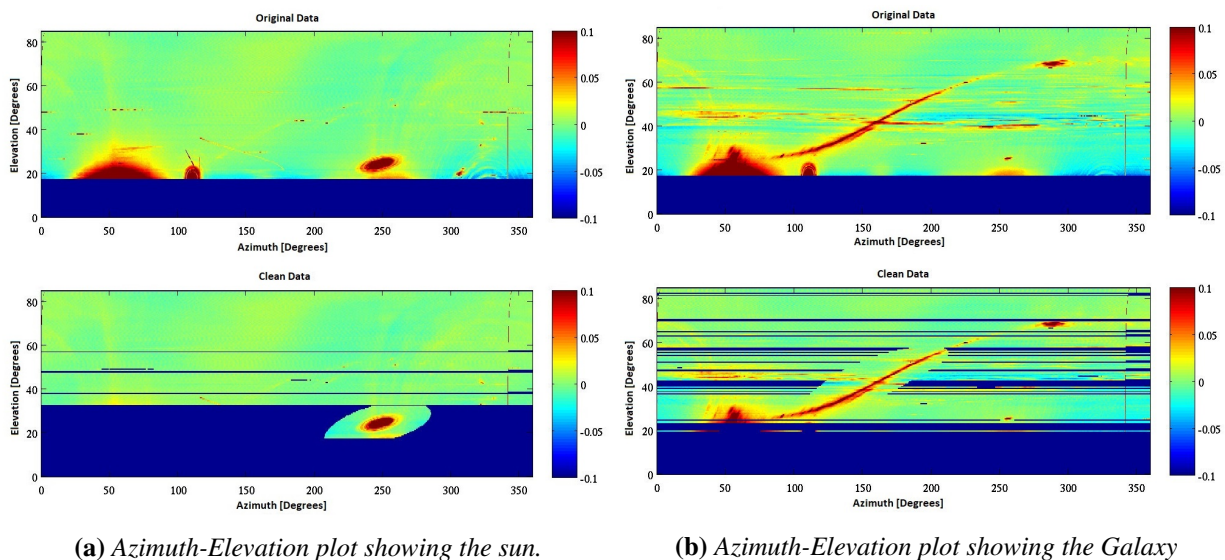


**Figure 3.15:** Azimuth-Elevation plots with and without RFI flagging in receiver backend units. Note that the ground term in the flagging routine had to be removed, resulting in a poorer fit between the expected signal and the data.

### 3.1.3.1 The Effect of the Ground Signal on the RFI Flagging Routine

The northern telescope was situated in a valley between two large mountain ranges. Radio signals reflected off of these mountains and were picked up by the receiver, effectively contaminating the data with a ground signal. This signal is identified and removed from the data by binning and averaging the data in azimuth, making a daily ground template to be subtracted from the data in each schedule. The data which is used to model the expected TOD sky signal during RFI removal has already been through this ground removal process, and so the ground contamination signal must be added back in to the expected TOD sky signal in order to achieve an accurate fit to the time ordered data. A different ground template is made for each elevation, that is, 37, 47, 67, 77 degrees, as well as for I1, I2, Q1, Q2, U1, U2. Figure 3.16 shows the ground templates over azimuth, for intensity,  $(I1 + I2)/2$ , for each elevation, averaged over the entire data set.

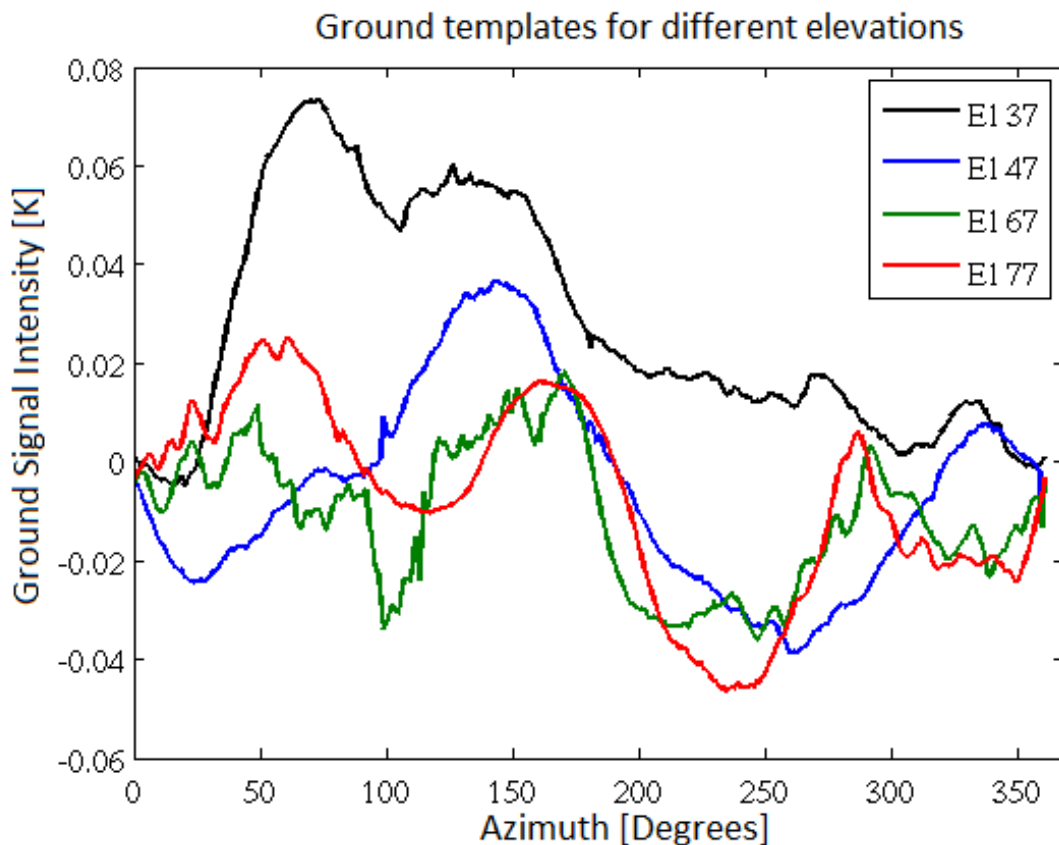


**Figure 3.16:** Templates for ground contamination in Stokes I at the different survey elevations.

During the expected TOD sky signal fitting process, the contribution due to ground at each point in azimuth is taken from the averaged ground template, scaled, and added to the scaled expected TOD sky signal. Figure 3.17 shows the effect of including ground contamination during the fitting process. Both plots show the time ordered data in black and the expected TOD sky signal in red over several azimuth scans. The panel on the left shows the expected TOD sky signal fitted to the time ordered data without including ground contamination. Note how the expected TOD sky signal has a consistent baseline, which would result in most of the data being incorrectly flagged as RFI. The panel on the right shows the expected TOD sky signal fitted to the time ordered data with the ground contamination signal included. There is a clear improvement of fit in the second case. Collaboration member Adam Barr is currently working on the ground removal process as part of his PhD thesis and the reader is referred to his thesis (currently in prep) for more information.

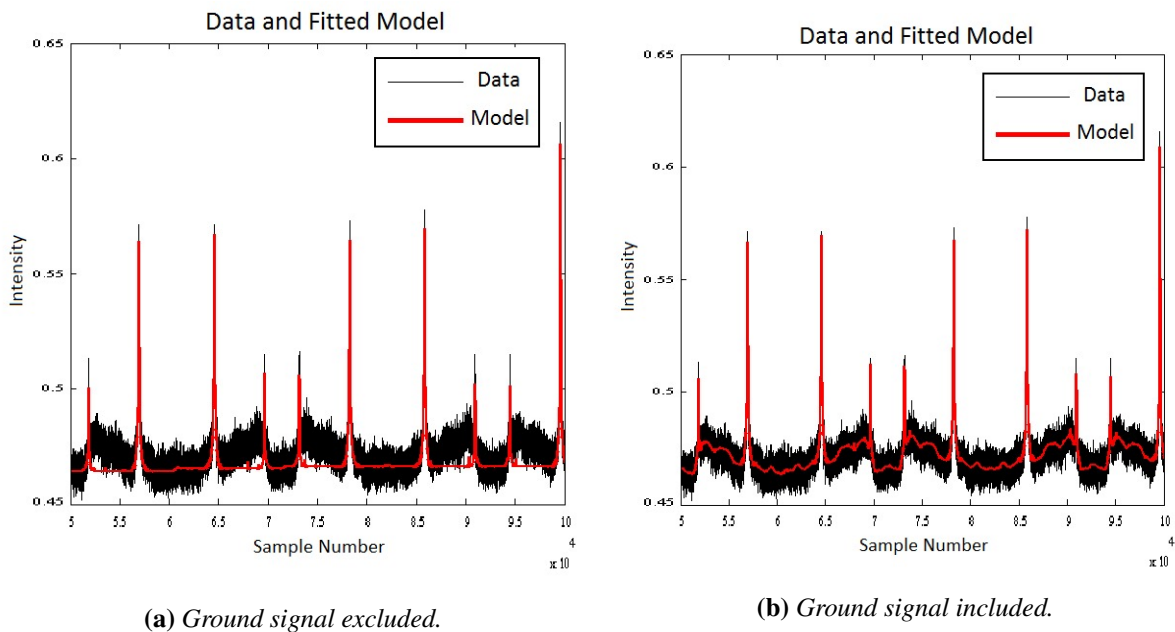


**Figure 3.17:** Several azimuth scans illustrating the importance of including the ground contamination signal in the expected TOD sky signal fitting process. At this point in the analysis pipeline, intensity is measured in backend units.

### 3.1.4 Pointing

Pointing offsets introduce noise into our final maps, as each measurement is stacked on top of the others. If the telescope position is not accurately known when making a measurement, then the position of the measurement on the sky will carry that inaccuracy, resulting in a smearing out of the measured power. Pointing offsets can be caused by several factors: encoder position, tilt, and antenna sag. The azimuth and elevation position of the telescope are measured by encoders. These encoders measure a voltage which is dependent on the angle of rotation. Encoder errors occur when the value assigned to the angle zero is incorrect. Tilt is the result of the azimuth and elevation axes not being entirely perpendicular and antenna sag is the result of the primary dish surface deforming slightly as a consequence of its own weight. We kept a record of pointing offsets with a pointing model; see Chapter 5 for a description of the pointing model for the southern system. The pointing model used the pointing offsets to determine the true telescope position and applied the correction in real time while the telescope was performing observations. Pointing corrections were applied roughly every two months on the northern telescope. Pointing errors are determined in the pipeline by fitting a 2D Gaussian to certain bright sources, Cygnus A, Cassiopeia A, Taurus A, and M42, whenever they appear in the data. According to Rohlfs and Wilson (2004), pointing offsets should not exceed 0.1 of the beam FWHM, as this ensures that the power measured within the beam is within 3 % of the total power of the source. The power response of a Gaussian beam is given by:

$$P(\theta) = P_0 e^{-\frac{\theta^2}{2\sigma^2}} \quad (3.3)$$

where

$$\sigma = \frac{FWHM}{2\sqrt{2\ln(2)}}. \quad (3.4)$$

Thus, to achieve a measured power that is within 3 % of the total power, our pointing offsets must be within 0.104 of the FWHM. For C-BASS, with a FWHM of around 44 arcminutes, we require pointing offsets of less than 4.5 arcminutes.

### 3.1.5 Calibration

Unlike space based astronomical experiments, ground based experiments must view the sky through a thick layer of atmosphere. Thus, before we begin with calibration, we must take the effect of the atmosphere into account. Water and oxygen molecules in the atmosphere absorb and re-emit incident electromagnetic radiation, which affects the atmospheric opacity. We measure changes in the atmospheric opacity as a function of elevation by performing ‘sky dips’ at the beginning and end of each schedule. During a sky dip, the telescope slews down and up in elevation to measure how the signal intensity changes with elevation, where a change in elevation results in a change in the amount of air that the signal passes through. This measurement allows us to determine an atmospheric opacity correction factor, which is applied to the entire schedule.

After the atmospheric calibration, we perform the astronomical calibration. The first step of the data reduction pipeline calibrated the data relative to the noise diode. In this step, we calibrate that data against one of three calibration sources, Cygnus A, Cassiopeia A, and Taurus A. These sources were chosen because they are point-like and bright at 5 GHz. We use the temperature of the calibration sources to determine the temperature of the noise diode and then scale the data by that temperature to calibrate the data in Kelvin.

### 3.1.6 Time Stream Processing Pipeline Output

The pipeline stores the reduced data in Flexible Image Transport System (FITS) format. These files contain MJD, right ascension, declination, azimuth, elevation, data flags, and the data in Stokes I, Q and U. The data flags consist of logical 1’s and 0’s to indicate the presence of RFI, Sun or Moon, and whether the data was taken during the day or at night. These FITS files are then used by our map making software to produce maps. We are currently using two different map making programs, DESCART and Ninkasi (Fowler et al., 2010), and these are discussed in Chapter 4.

## 3.2 Producing a Final Data Set

The data reduction pipeline is still very much a work in progress, however, we believe that we are nearing the threshold of ‘science quality’ data. In an attempt to produce a subset of our data that is ready for science, a data set that is reliable, without excessive systematic errors and inconsistencies, we decided to run the pipeline with very stringent RFI flagging conditions, using only our Elevation 37 data set. This data set consisted of 3431 schedules, taken from November until July 2014. Figure 3.18 shows the percentage flagged per schedule over the entire Elevation 37 data set. The mean percentage of data affected by RFI, indicated in the figure by the solid red line, was about 45 %, and the median, illustrated by the green line, was found to be 37 %. However, this data set includes some completely unusable data. Of the 3431 schedules, 684 were 100 % flagged, including data from several months in early 2013. This was due to some cracked cables in the receiver which added spurious signals and noise into the data. The receiver was serviced in July 2013, resulting in a notable improvement in the data quality. If we only use data from after this service, and we exclude the schedules that were 100 % flagged, then the mean percentage of data affected by RFI in a given Elevation 37 schedule is found to be about 24 % for 2385 schedules. This value is pulled up by the presence of many high RFI schedules, and so a median of 12 % is a more accurate description of the expected RFI in a given schedule of Elevation 37 data. The percentage flagged per schedule for the period July 2013 to July 2014, with all 100 % flagged schedules removed, is shown in Figure 3.19 with the red and green lines once again illustrating the mean and median flagged percentage per schedule. Table 3.1 is a summary of the Elevation 37 data from the period July 2013 to July 2014 with the 100 % flagged schedules excluded. This table indicates the number of schedules run per month at elevation 37 degrees, as well as the mean and median amount of data flagged as RFI per schedule for that month. There were fewer Elevation 37 schedules run in June and July of 2014 as we had begun to look at other elevations by that point. The Elevation 37 data set is currently being investigated for systematics, and some of these investigations are discussed in Chapter 4.

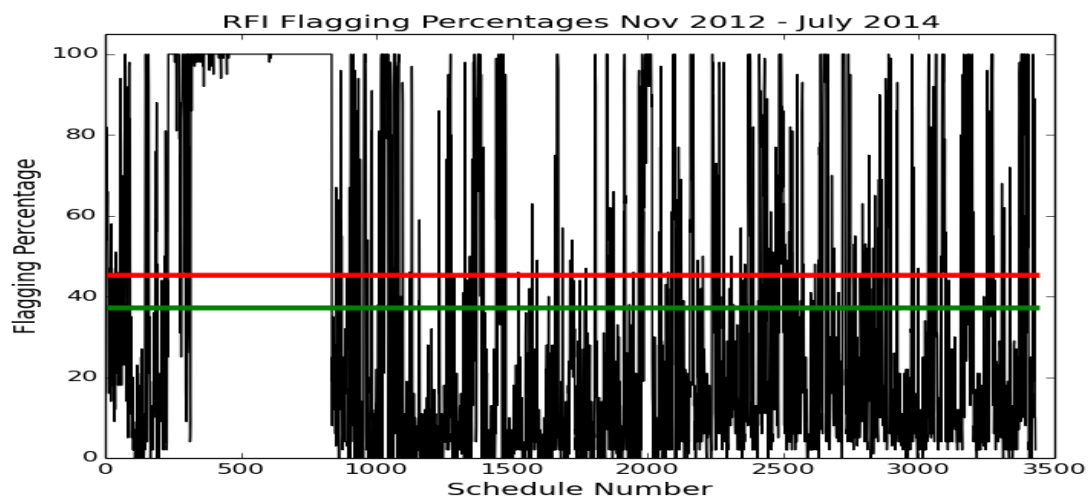


**Figure 3.18:** The percentage of RFI flagged per schedule for the Elevation 37 data set, where the red line indicates the mean RFI affected data percentage per schedule, and the green line indicates the median.

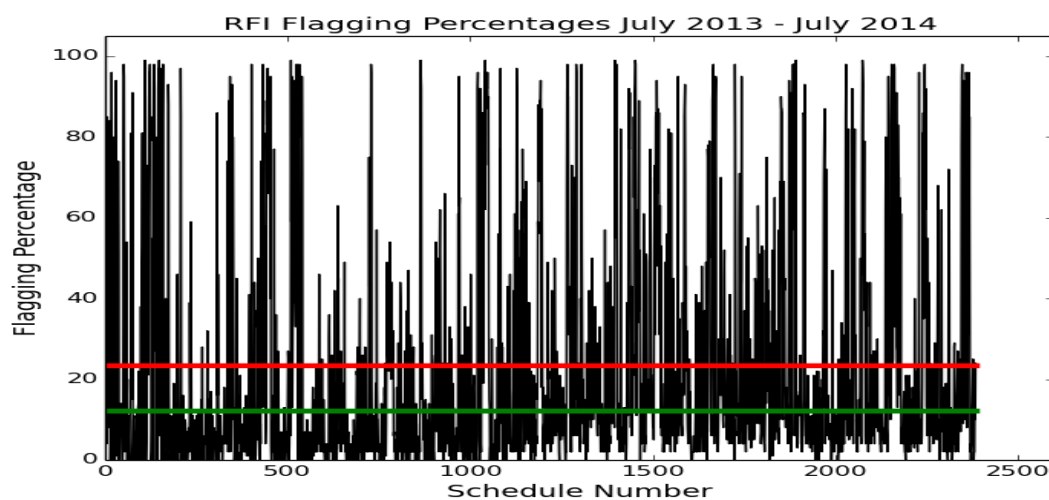


**Figure 3.19:** The percentage of RFI flagged per schedule for the Elevation 37 data set, where the red line indicates the mean RFI affected data percentage per schedule, and the green line indicates the median. All survey schedules that were 100% flagged have been removed from this data set.

**Table 3.1:** *Summary of RFI flagging percentages per month for the period July 2013–July 2014.*

| Month    | No of Schedules | Mean % | Median % |
|----------|-----------------|--------|----------|
| Jul 2013 | 181             | 32     | 14       |
| Aug 2013 | 254             | 14     | 6        |
| Sep 2013 | 231             | 20     | 6        |
| Oct 2013 | 213             | 13     | 5        |
| Nov 2013 | 227             | 21     | 10       |
| Dec 2013 | 139             | 24     | 15       |
| Jan 2014 | 217             | 26     | 14       |
| Feb 2014 | 202             | 26     | 14       |
| Mar 2014 | 217             | 26     | 16       |
| Apr 2014 | 232             | 22     | 11       |
| May 2014 | 169             | 26     | 13       |
| Jun 2014 | 63              | 13     | 9        |
| Jul 2014 | 40              | 38     | 25       |

### 3.3 Future Work

There is still plenty of work to be done, on the data reduction pipeline in general and on the RFI flagging routine. Currently, the routine is only applied to intensity data. I would like to apply it individually to each channel, as sometimes RFI is present in one channel, but not the other, and it gets averaged away when the two channels are combined. I would also like to look for RFI in the Stokes Q and U channels, as RFI is often polarized. I also wish to further interrogate another method of looking for RFI that varies quickly. This method is outlined in Chapter 5, where I applied it to the southern data.

RFI and ground signal are interconnected. Ideally, we would address them simultaneously in the pipeline, but unfortunately, the presence of RFI strongly affects the ground template. Thus, we plan to run the pipeline over several iterations, using the produced data set and the ground templates from the previous iteration as models of the expected signal for the next iteration. This

should finally result in a data set that is completely free of RFI and ground signal. The Elevation 37 ground templates are used to produce the ground templates for other elevations. Therefore, we plan to operate the pipeline on the other elevation data sets, so that we finally have a full, clean, reliable C-BASS North data set. Finally, we plan to apply a slightly modified version of this pipeline to our southern data in order to complete our survey and produce high fidelity maps of the entire sky.

# Chapter 4

## Map Making and Data Consistency Tests

In the previous chapter, I discussed the analysis of the low-level time ordered data. In this chapter, I will describe the map making process where we take the data produced by the analysis pipeline and make maps, both in temperature and polarization. Two map making programs are currently being tested, and they will be described in the following section. I will also discuss some of the data consistency tests that have been conducted to ensure the scientific quality of our data.

### 4.1 Map Making

The incredible volume of data produced by CMB experiments requires methods of reducing the data volume without sacrificing the integrity of the cosmological signal. Reducing the raw data into a map can reduce the data volume by orders of magnitude (Tegmark, 1997). CMB experiments employ various methods to produce sky maps from their data, and care must be taken to choose a method that meets the correct balance between computational expense and signal integrity. One common map making method uses maximum-likelihood to reduce noise while completely preserving the signal (Tegmark (1997); Doré et al. (2001); Stompor et al. (2002); de Gasperis et al. (2005)). We are currently experimenting with two different maximum-likelihood map making software packages: Ninkasi, which employs only the maximum-likelihood method, and DESCART, which incorporates a destripping algorithm to augment the maximum-likelihood

method in an effort to reduce computation time. Long term low frequency noise drifts, called  $1/f$  noise, are caused by atmospheric fluctuations along the telescope line of sight. The destriping algorithm (Delabrouille (1998); Burigana et al. (1999); Maino et al. (1999); Keihänen et al. (2010, 2005, 2004); Kurki-Suonio et al. (2009)) attempts to combat  $1/f$  noise in the TOD by subtracting a series of offsets. These offsets approximate the low frequency drifts in the TOD. Both DESCART and Ninkasi aim to produce an unbiased map of the sky by solving for  $\hat{m}$  in the following equation:

$$P^T N^{-1} P \hat{m} = P^T N^{-1} d \quad (4.1)$$

where  $\hat{m}$  is the output map,  $P$  is the pointing matrix used to project the map into the time stream,  $N$  is the noise covariance matrix, and  $d$  is the data. The data can be described as the true sky map  $m$  projected into the time stream via the pointing matrix as

$$\langle d \rangle = P m. \quad (4.2)$$

Thus, Equation 4.1 becomes

$$\langle P^T N^{-1} P \hat{m} \rangle = \langle P^T N^{-1} P m \rangle, \quad (4.3)$$

and provided the noise on both sides of the equation is identical, on average,  $\hat{m}$  is  $m$ , the true unbiased sky map. While this is true in theory, in reality, the noise model is extremely unlikely to match the actual noise exactly, which means that generally  $\hat{m} \approx m$  on average, rather than exactly equal. In order to achieve an unbiased map, the accuracy of the noise model is less important than keeping the noise consistent on both sides of the equation. This means that DESCART and Ninkasi can both produce unbiased maps, even though they model the noise differently. This will be discussed in the following sub-sections.

One alternative map making method that is commonly employed is filtered map making. In this method, a high pass filter is applied to the time ordered data. This aims to reduce striping in the map by reducing long term noise fluctuations. The angular power spectrum of the map produced using this method is determined using Monte Carlo pseudo- $C_\ell$  methods (Szapudi et al. (2001); Hivon et al. (2002)). While this method is quick, given that the high pass filter eliminates

the need for multiple iterations, it can result in the distortion of the TOD signal as time stream filters introduce bias. Thus, unlike the methods used in DESCART and Ninkasi, maps produced with filtered map making methods are biased maps and this bias must be addressed using simulations.

### 4.1.1 Map Making with Ninkasi

Ninkasi is the maximum-likelihood map maker used by the Atacama Cosmology Telescope as described by Fowler et al. (2010) and Dünner et al. (2013). It works by finding the best-fit sky map that minimizes  $\chi^2$  when given a noise and data model. The data is modelled as

$$d = Pm + n \quad (4.4)$$

where  $d$  is the data,  $P$  is the pointing matrix used to project the map into the time stream,  $m$  is the true sky map for which we wish to solve, and  $n$  is the noise model. The maximum-likelihood method requires us to find the model that will maximize the likelihood function

$$\mathcal{L} = \exp\left[-\frac{1}{2}(d - Pm)^T N^{-1}(d - Pm)\right] \quad (4.5)$$

where the noise covariance matrix  $N$  is estimated by  $N \equiv \langle nn^T \rangle$ . The matrix  $P^T N^{-1} P$  in the standard least-squares solution, Equation 4.1, is too big to be easily inverted. Thus, the least-squares solution for  $m$  is solved iteratively using a Preconditioned Conjugate Gradient (PCG) scheme (Wright et al. (1996); Hinshaw et al. (2003)), which uses  $G$ , an approximate inverse of  $P^T N^{-1} P$ , to speed up convergence by solving the better conditioned system:

$$GP^T N^{-1} Pm = GP^T N^{-1} d. \quad (4.6)$$

The noise in Equation 4.6 can be viewed as a set of weights used to reduce the impact of unwanted modes. As long as these weights are applied equally to both sides of Equation 4.6, this will produce an unbiased map.

Ninkasi uses the PCG algorithm to solve for the map, using the hit-count map as a preconditioner and accounting for bias with an estimation of the noise. Bias can arise when noise estimates are made on time stream data that still contains signal. It is induced in the map by noise fluctuations in the time stream data as sometimes the noise is positively correlated with the signal, and sometimes it is negatively correlated. When the noise is negatively correlated with the signal, the variance of the measurement will be low, resulting in that period of data incorrectly receiving a higher weighting. Similarly, a period of data where the noise fluctuation is positively correlated with the signal will incorrectly receive a low weighting. These incorrect weightings induce bias. We reduce the bias effect by subtracting an estimate of the signal from the data before estimating the noise. This noise estimate is then used to produce an output map, which is the difference between the data and the signal estimate. The output map and original signal estimate are combined to form a new signal estimate, which is subtracted from the data to produce a new noise estimate. This process is repeated over a number of iterations to produce a final map. The number of iterations is determined by looking at how the power spectrum of the output changes after each iteration. Once the power spectrum becomes consistent, there is no need for further iterations. For our maps, 500 iterations produces a sky map that has converged sufficiently for preliminary investigations. The production of the final converged sky maps will require several runs of 500 iterations, with the brighter signal in the Stokes I map requiring more runs than the Stokes Q and U maps.

#### 4.1.2 Map Making with DESCART

The DEStriping CARTographer (DESCART), developed by Sutton et al. (2009, 2010), is a destriping map maker specifically designed to handle the large data sets produced by modern experiments in the search for  $B$ -mode polarization. The idea behind a destriping algorithm is to remove offsets in the data caused by  $1/f$  noise in the form of long term instrument gain drifts and, in the case of ground based telescopes, atmospheric fluctuations. Once the  $1/f$  noise is removed, the remaining noise is expected to be Gaussian white noise, which makes map making trivial as the best map is just the noise-weighted average of the data in each map pixel.

DESCART assumes a slightly modified model for the data, when compared to Equation 4.4,

$$d = Pm + n_W + Fa \quad (4.7)$$

where the noise has been split into a white noise component,  $n_W$ , and a  $1/f$  noise component,  $Fa$ . The matrix  $F$  maps a set of basis functions, with amplitudes  $a$ , onto the time stream data. This leads to the least-squares solution

$$P^T N_W^{-1} Pm = P^T N_W^{-1} (d - Fa), \quad (4.8)$$

similar to Equation 4.1, with  $N_W$  the white noise covariance matrix. Thus the correlated noise,  $Fa$  is subtracted from the time stream data  $d$ , leaving only signal and uncorrelated white noise. Like Ninkasi, DESCART employs a PCG algorithm to solve for the map, but does so in fewer iterations because of the preconditioning and noise covariance matrices used in this method. Where Ninkasi uses the hits map as the preconditioner and doesn't break the estimated noise into components, DESCART splits the noise estimate into white and correlated noise uses a preconditioner that is a combination of both noise component covariance matrices. Both DESCART and Ninkasi should achieve an unbiased sky map, but by using different noise estimates and, in the case of DESCART, with fewer iterations.

The difficulty that we have experienced with DESCART is that it was designed to operate on long, continuous data sets, not data sets intermittently flagged for RFI. In Sutton et al. (2009), they specifically name  $C_{\ell\text{over}}$  (North et al., 2008) as the type of experiment that DESCART was designed for, along with balloon borne experiments like EBEX (Oxley et al., 2004) and SPIDER (MacTavish et al., 2008). Thus, the remaining work in this thesis is based on map making in Ninkasi. For the sake of completeness, I have provided a brief description of DESCART. A full account of our investigations with DESCART can be found in fellow collaboration member Luke Jew's PhD thesis (in prep).

### 4.1.3 Convergence Tests

A typical Ninkasi run compares an input map (or best guess model) against the data over 500 iterations, resulting in an output map that represents the difference between the input map and the data. Thus, the sky map produced by Ninkasi is the sum of the input and output maps. We had to be sure that the output map was completely uninfluenced by the input map before we could trust the output from Ninkasi. This was confirmed by running a convergence test. The convergence test consisted of two series of Ninkasi runs, using two different sets of input maps. In all cases the bright Galactic signal in the input map, as well as in the data, was masked at a threshold of  $0.05 K$ , with the mask smoothed by the C-BASS beam. The first series of Ninkasi runs, the control test, began with an input map made from six months of data. This input map was made using DESCART. The second series was performed using an input map consisting of the same six months of data, but with an added artificially injected signal. This artificial signal was a simulated signal drawn from the power spectrum of the original input map itself and was statistically consistent with the true sky signal. The goal of the experiment was to show that after several Ninkasi runs, the sky maps from the two series of runs would converge, thus proving that Ninkasi's resulting sky map was dependent on the data, and independent of input map.

The first series began with an input map made from six months of data, denoted here as  $(O)$ . Running Ninkasi over 500 iterations using this map as an input resulted in the first output map, denoted as  $(r_1)$ . This output is the difference between the input map (or best guess model) and the data. Thus, the output was added to the original input map to make a new input map for the second Ninkasi run, denoted as  $(O + r_1)$ . The output from the second Ninkasi run,  $(r_2)$ , was added to the input map to create the input for the third run,  $(O + r_1 + r_2)$ . This process was repeated over several Ninkasi runs, with the input map for the next run always updated by the output from the previous run.

The second series began with the same six month map,  $(O)$ , with an artificial signal  $(S)$  added to it. The artificial signal was produced by masking the brightest parts of the input map,

smoothing the mask by the C-BASS beam, calculating the power spectrum of the masked map and then simulating the signal. The power spectra of the masked original input map ( $O$ ) and the artificial signal are shown in Figure 4.1. The artificial signal was then injected into the six month map from the control test to serve as the other input map, denoted as ( $O + S$ ). The original input map ( $O$ ) and the signal added input map ( $O + S$ ), used in the first Ninkasi run for each series respectively, are shown in Figure 4.2, along with the difference between them, which is effectively the injected artificial signal ( $S$ ).

For the sake of clarity, I will refer to the input map of each successive Ninkasi run from the first series of runs as the ‘clean input map’ because it has no injected artificial signal added to it. I will refer to the input map of each successive Ninkasi run from the second series of runs as the ‘signal added input map’ because it does have the injected artificial signal.

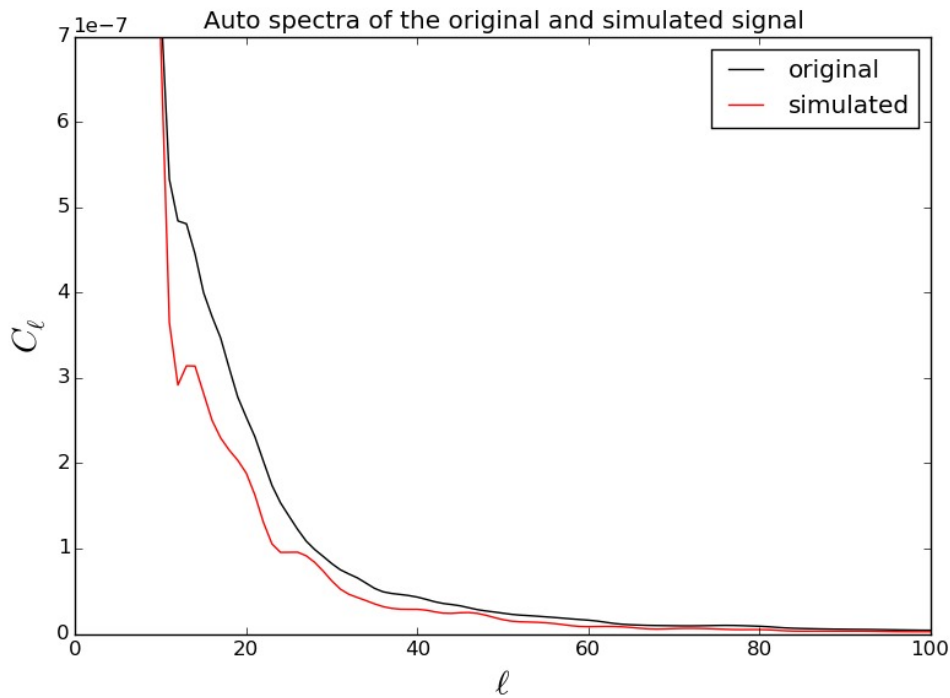


**Figure 4.1:** This plot shows the auto spectrum of the input map made from six months of data and used as the estimate in the first Ninkasi run. It also shows the power spectrum of the artificial signal that was injected into the six month map to form the input estimate for the second series of Ninkasi runs.

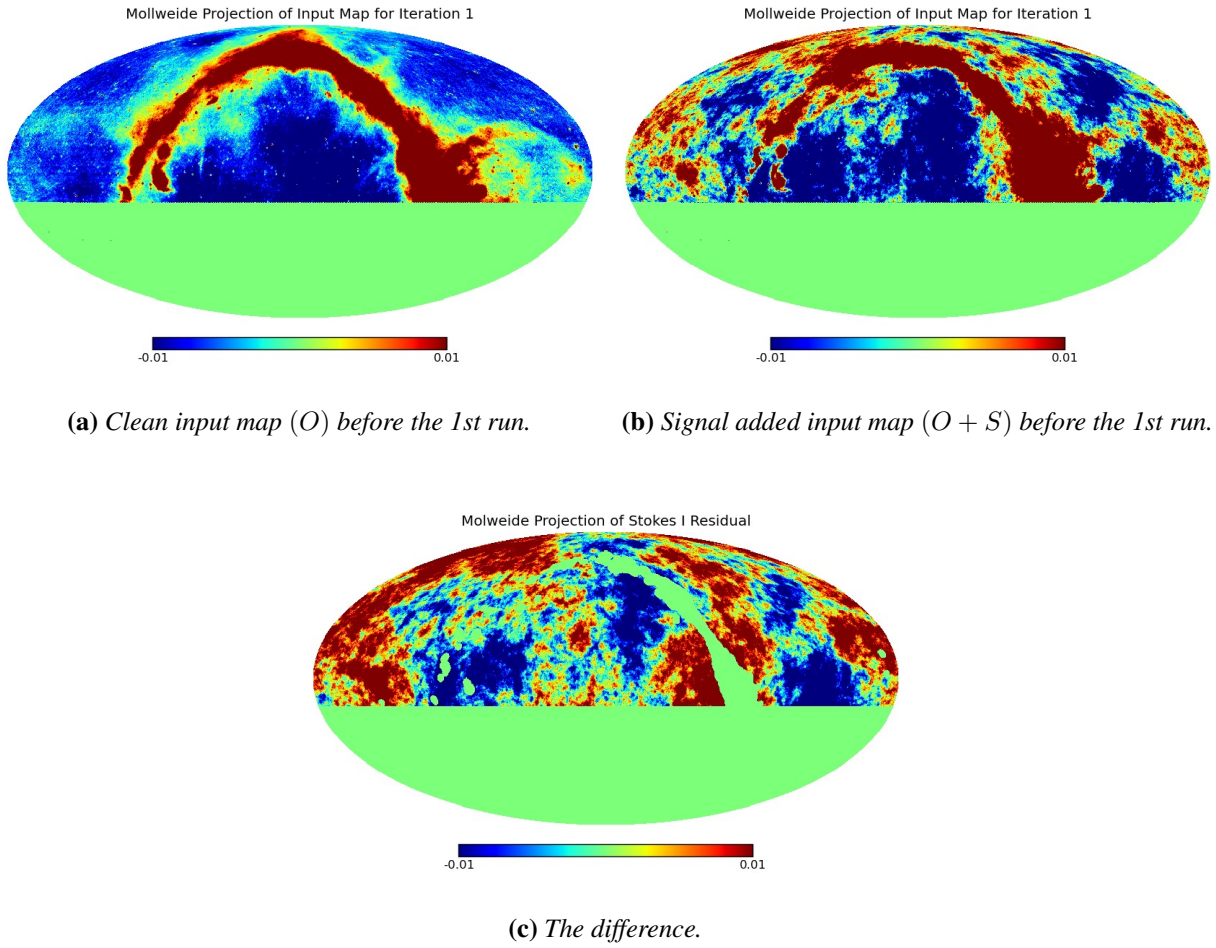


**Figure 4.2:** Input maps for the first Ninkasi runs of each series in Stokes I with the clean map on the left, signal added map in the middle and the difference between them on the right. The temperature scale is in Kelvin.

The process of producing new input maps by adding the input and output map from the previous run was repeated for this series of Ninkasi runs, resulting in a final input map ( $O + S + R_1 + \dots + R_n$ ) where the capital  $R$  denotes an output from the second series of runs as opposed to the first series output  $r$  and  $n$  is the number of Ninkasi runs. In the event of a successfully converged map, the sum of Ninkasi output maps  $R_1 + \dots + R_n$  from the second series of runs would compensate for (and therefore remove) the injected artificial signal  $S$ . The input maps used in several runs for both the clean and signal added Ninkasi runs are shown in Figure 4.3, with the clean maps in the left column, the signal added maps in the central column, and the difference

between them in the right column. This whole process was repeated for Stokes I, Q and U.

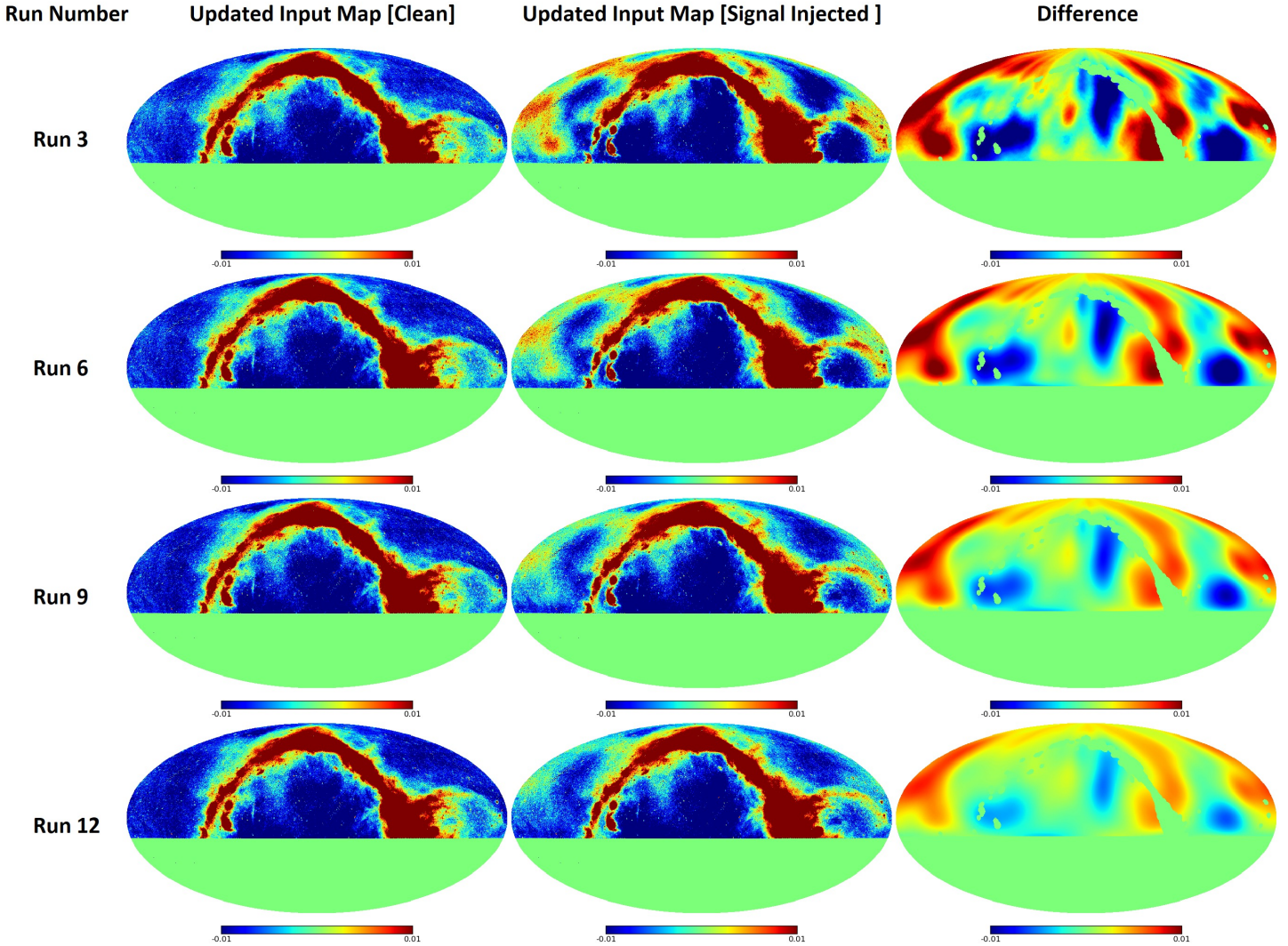


**Figure 4.3:** *Input maps for several Ninkasi runs in Stokes I with clean maps on the left, signal added maps in the middle and the difference between them on the right. The temperature scale is in Kelvin.*

The aim of our investigation was to determine the degree to which the final Ninkasi map estimate depends on the input guess. This was done by investigating the difference between the resulting sky maps of the two series of Ninkasi runs after each run. Merely investigating the differences between the maps provides no information on the angular scale of potential discrepancies. This is particularly important, for example, when considering the relevance of our maps

to foreground removal in  $B$ -mode searches. Thus an investigation of the angular power spectrum is required. We took the auto correlated spectrum of the residual signal in the differenced maps and compared this to the auto spectrum of the injected artificial signal. If the auto spectrum of the residual was of similar order to that of the artificial signal, then the injected artificial signal (or at least a large part of it) still remained, and the maps had not converged. Conversely, if the auto spectrum of the residual was small relative to that of the artificial signal, then the injected artificial signal (or at least most of it) had been removed and the maps had converged. This was tested further by taking the cross correlation of the residual signal and the injected artificial signal. A high cross correlation between these two signals would also indicate that the injected artificial signal was still influencing the final Ninkasi map, resulting in an unconverged map, while a low cross correlation would indicate a converged map.

To investigate this mathematically, we look at the fractional error in the power spectrum that comes from lack of convergence, or the degree to which the input guess leaks into the final calculated result. Let us say that  $q$  represents the injected artificial signal map, and  $p$  represents the residual map (which can be thought of as the sum of systematic and statistical errors). The fractional power spectrum error is then given by

$$\frac{\langle (p+q)^2 \rangle - \langle q^2 \rangle}{\langle q^2 \rangle} = \frac{\langle (p+q)^2 \rangle}{\langle q^2 \rangle} - 1. \quad (4.9)$$

If we expand the terms, then the fractional power spectrum error is

$$\frac{\langle p^2 + 2qp + q^2 \rangle}{\langle q^2 \rangle} - 1 = \frac{\langle p^2 + 2qp \rangle}{\langle q^2 \rangle}, \quad (4.10)$$

which reduces to

$$\frac{\langle 2qp \rangle}{\langle q^2 \rangle} \quad (4.11)$$

in the limit that  $p$  is much smaller than  $q$ . This expression provides us with a reasonable estimation of the fractional error in the power spectrum arising from map making systematics. We can also investigate the worst case scenario for the fractional power spectrum error by replacing the cross spectrum  $\langle qp \rangle$  with an upper bound from the triangle of inequality

$$|\langle qp \rangle| \leq \sqrt{\langle q^2 \rangle \langle p^2 \rangle}. \quad (4.12)$$

The right hand side of this equation relies only on the auto spectra  $\langle q^2 \rangle$  and  $\langle p^2 \rangle$ , and so the worst case estimate of the fractional power spectrum error is then

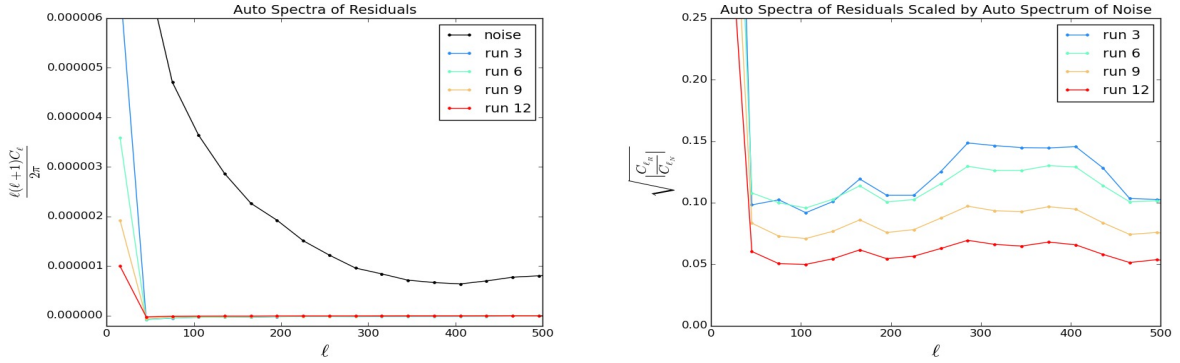
$$\frac{2\sqrt{\langle q^2 \rangle \langle p^2 \rangle}}{\langle q^2 \rangle} \quad (4.13)$$

which simplifies to

$$2\sqrt{\frac{\langle p^2 \rangle}{\langle q^2 \rangle}}. \quad (4.14)$$

Thus, we have two estimates of the fractional error in the power spectrum that result from map making systematic errors: the cross spectrum expression (Equation 4.11), which represents our best guess, and the auto spectrum expression (Equation 4.14), which represents the estimate for the worst case scenario. Note that in the results presented in this chapter, I have ignored the factor of 2 present in Equations 4.11 and 4.14.

The maps in Figure 4.3 show clear evidence of a trend towards convergence, with a large residual signal in the first runs becoming very small in later runs. This trend is confirmed when looking at the binned power spectra of the residuals as shown in Figure 4.4 (a), which shows the auto spectra of the residuals as well as that of the injected artificial signal. The spectra have been grouped into  $\ell = 30$  bins to smooth the plots and improve clarity. The requirement that the residuals are small relative to the added signal is confirmed in Figure 4.4 (b) which shows the square root of the ratio between the auto spectra of the residuals and the auto spectrum of the artificial signal, as shown in Equation 4.14. These plots show that while the residuals of the first runs were large, the residuals of later runs are only a few percent of the artificial signal, with the 12th run showing residuals of about 6 % of the artificial signal. It is important to check that this residual signal is not a result of the injected artificial signal. This is confirmed by looking at the cross correlation between the residual and the artificial signal.

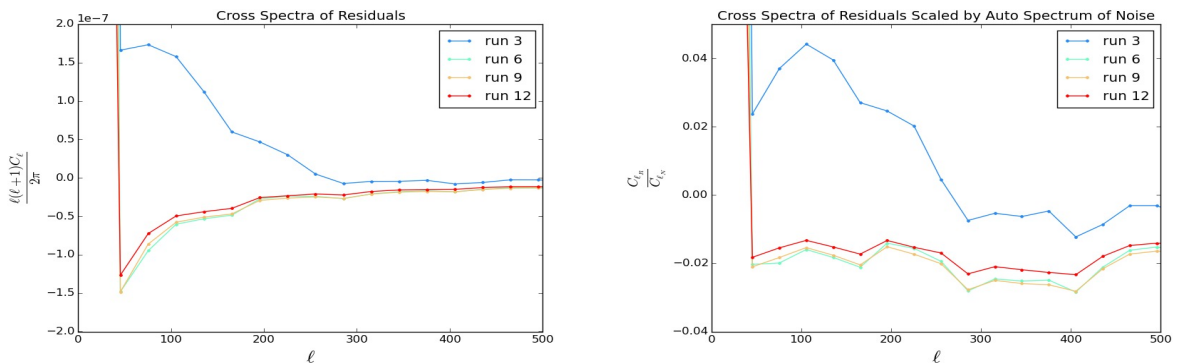


(a) Auto spectra of the residuals after selected Ninkasi runs and the auto spectrum of the injected artificial signal in Stokes I.

(b) Square root of the ratio of the auto spectra of the residuals after selected Ninkasi runs, and the auto spectrum of the injected artificial signal in Stokes I.

**Figure 4.4:** Auto spectra of the residuals after selected Ninkasi runs and the injected artificial signal (denoted as ‘noise’) in Stokes I, binned by  $\ell = 30$ .

The cross correlation between the injected artificial signal and the residual decreased with each successive run as the maps began to converge, ending with a cross correlation of order 2 % by the 12th run. This is low enough when compared to other instrumental systematic errors that we can conclude that the intensity maps converged sufficiently within twelve Ninkasi runs. The cross correlation is shown in Figure 4.5 (a), while Figure 4.5 (b) shows the ratio between the cross correlated signal and the auto spectrum of the injected artificial signal, as shown in Equation 4.11.



(a) Cross correlation between the residuals and the injected artificial signal.

(b) The ratio between the cross correlated signal and the auto spectrum of the injected artificial signal.

**Figure 4.5:** Cross correlation between the residuals and the injected artificial signal in Stokes I, binned by  $\ell = 30$ .

The polarization maps were tested in the same manner, where input maps of Stokes Q and U were used in two series of Ninkasi runs, one series using the clean maps and the other using maps that had been injected with the artificial signal. In this case, only the  $E$ -mode power spectra from the original Q and U maps were used to produce the artificial signal. The power spectra of the masked original input map ( $O$ ) and the artificial signal are shown in Figure 4.6. The input maps in used in the first run of each series for Stokes Q and U are shown in Figures 4.7 and 4.8, with the clean maps on the left, signal added maps in the middle, and the difference between them (effectively the injected artificial signal ( $S$ )) on the right.

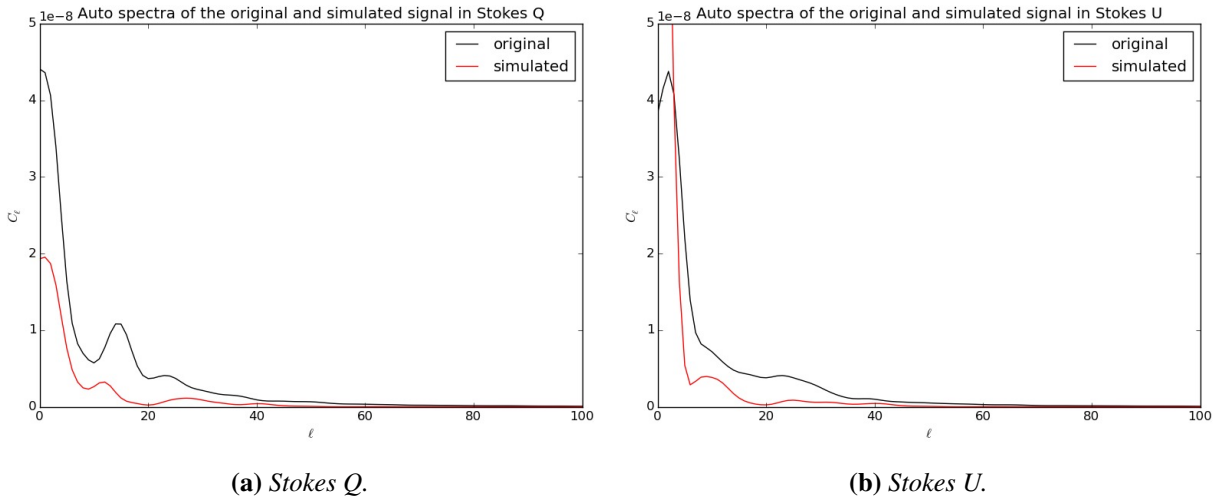


**Figure 4.6:** These plots show the auto spectrum of the input map used as the estimate in the first Ninkasi run for Stokes Q and U. They also show the power spectrum of the artificial signal that was injected into the original input map to form the input estimate for the second series of Ninkasi runs.

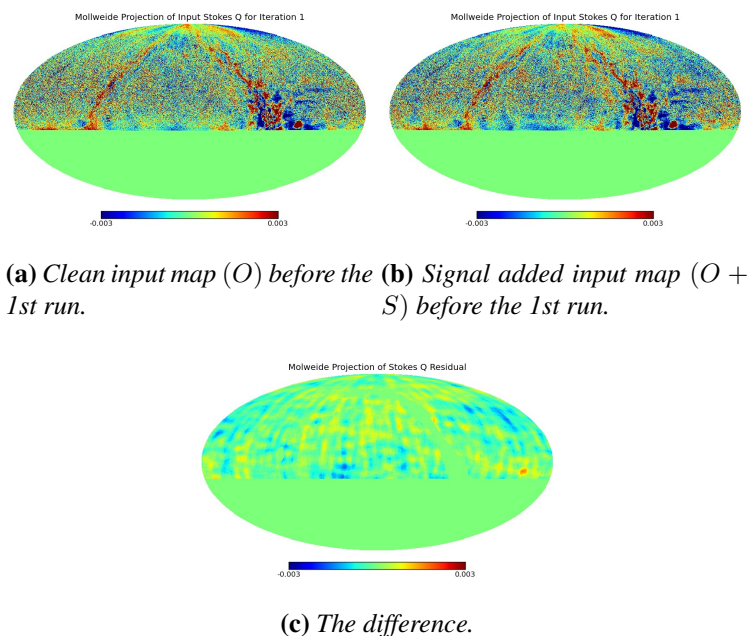


**Figure 4.7:** Input maps for the first Ninkasi runs of each series in Stokes  $Q$  with the clean map on the left, signal added map in the middle and the difference between them on the right. The temperature scale is in Kelvin.

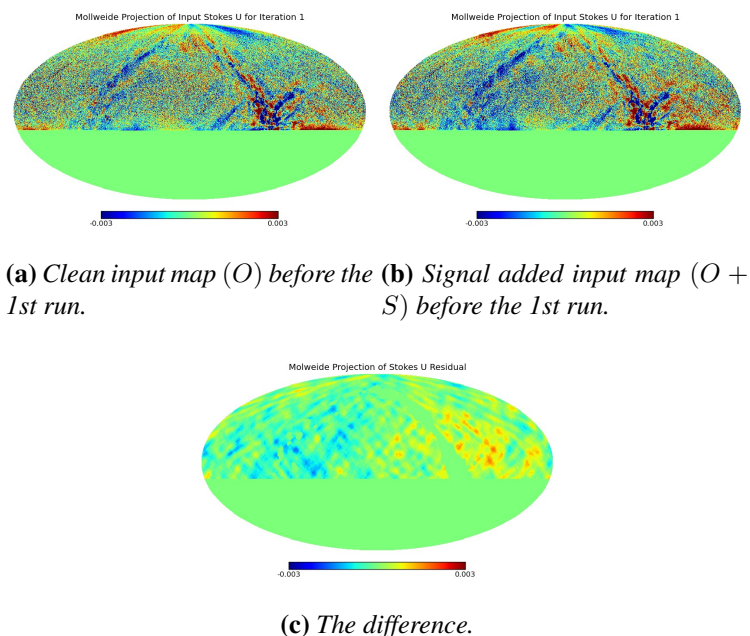


**Figure 4.8:** Input maps for the first Ninkasi runs of each series in Stokes  $U$  with the clean map on the left, signal added map in the middle and the difference between them on the right.

Figures 4.9 and 4.10 show the input maps used for each successive run, as well as the difference between them, illustrating the trend towards a converged map with each successive Ninkasi run.

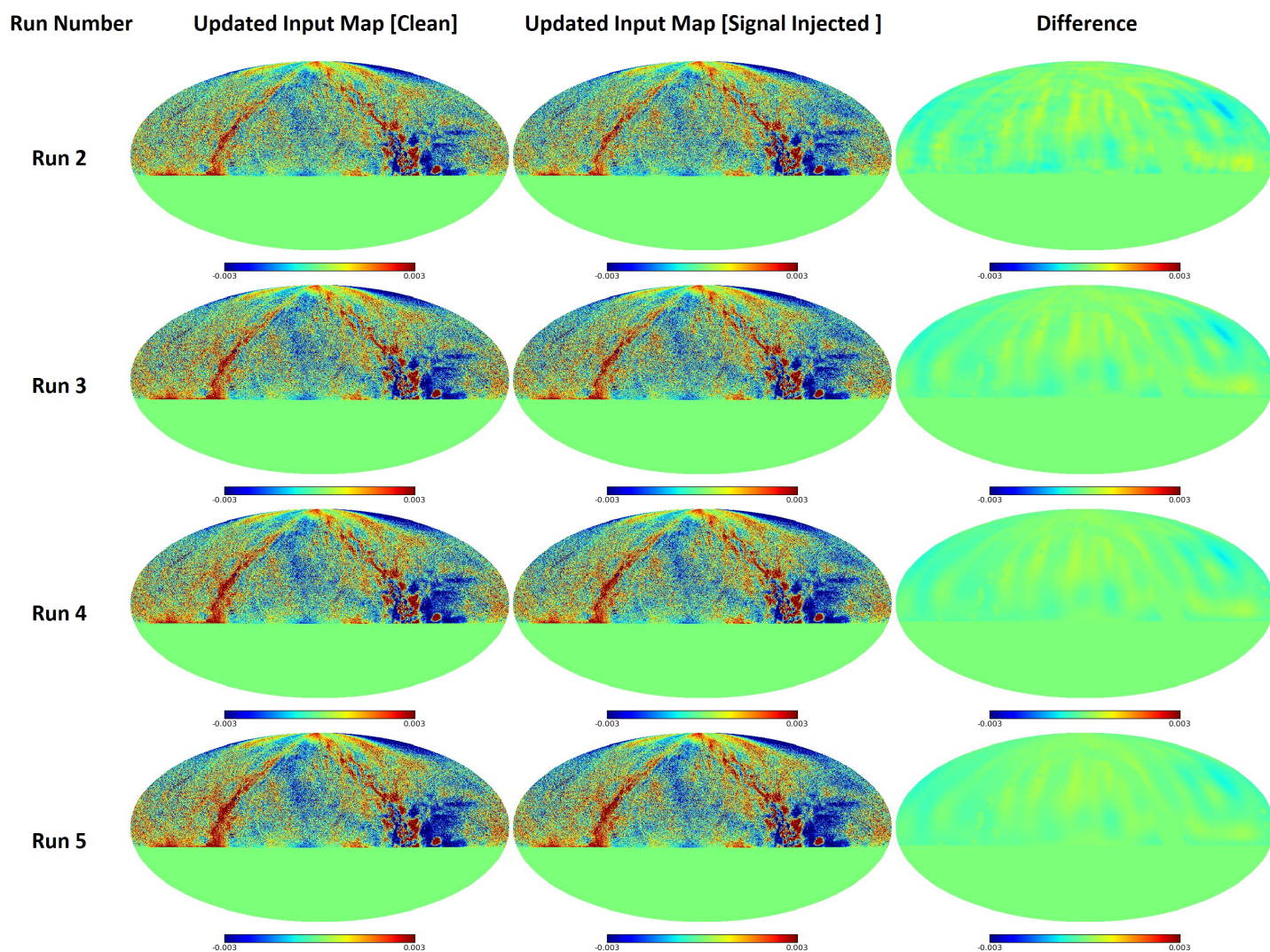


**Figure 4.9:** Input maps for several Ninkasi runs in Stokes  $Q$  with clean maps on the left, signal added maps in the middle, and the difference between them on the right. The temperature scale is in Kelvin.

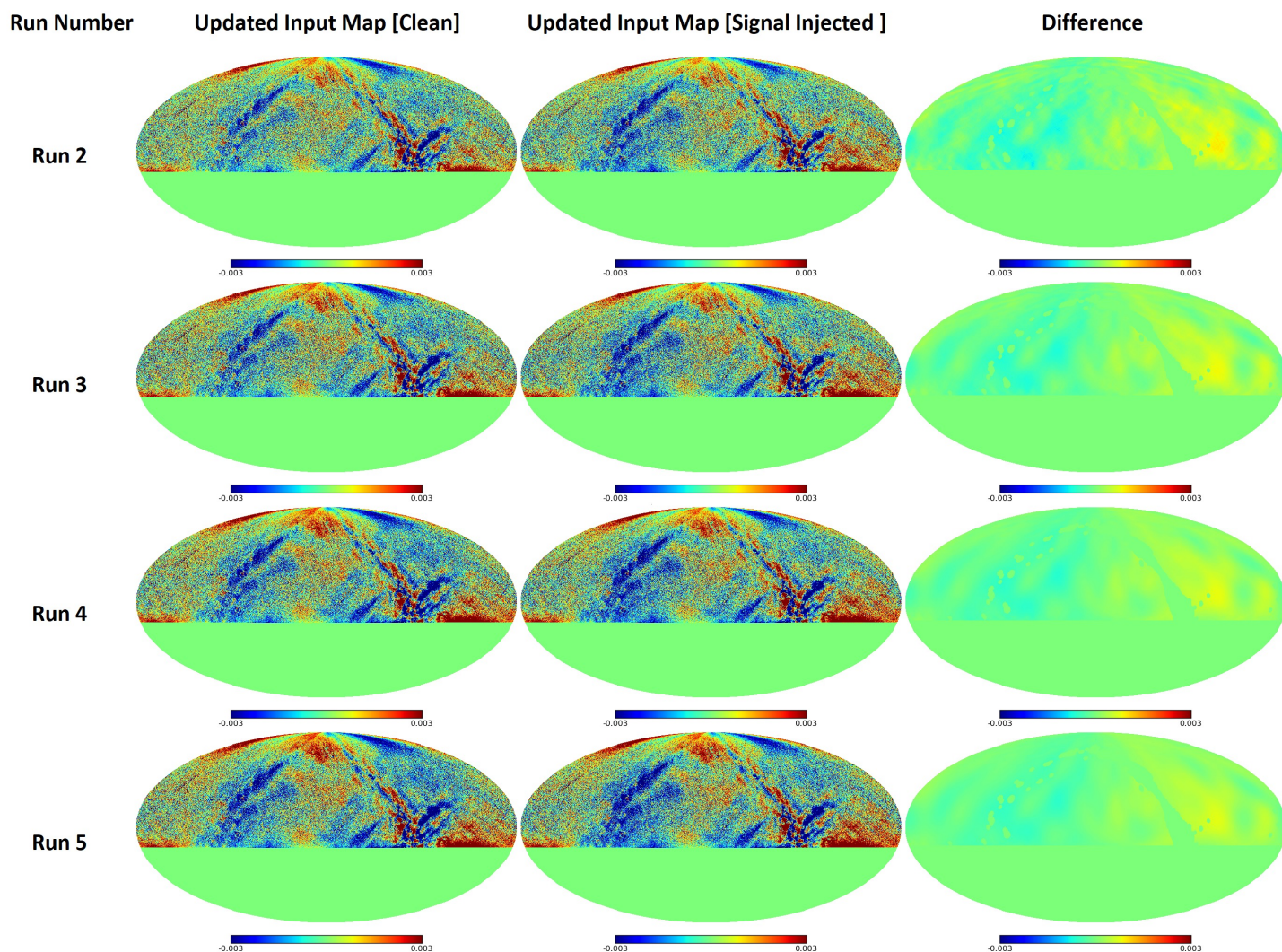


**Figure 4.10:** Input maps for several Ninkasi runs in Stokes  $U$  with clean maps on the left, signal added maps in the middle, and the difference between them on the right. The temperature scale is in Kelvin.

This trend is confirmed when looking at the power spectra of the residuals as shown in Figure 4.11, which shows the auto spectra of the residuals as well as that of the injected artificial signal. The requirement that the residuals are small relative to the artificial signal is confirmed in Figure 4.12 where the power spectra of the residuals have been scaled by the power spectrum of the injected artificial signal. As was the case for intensity, these plots show that while the residual of the first run was large, the residuals of later runs are only a few percent of the artificial signal.

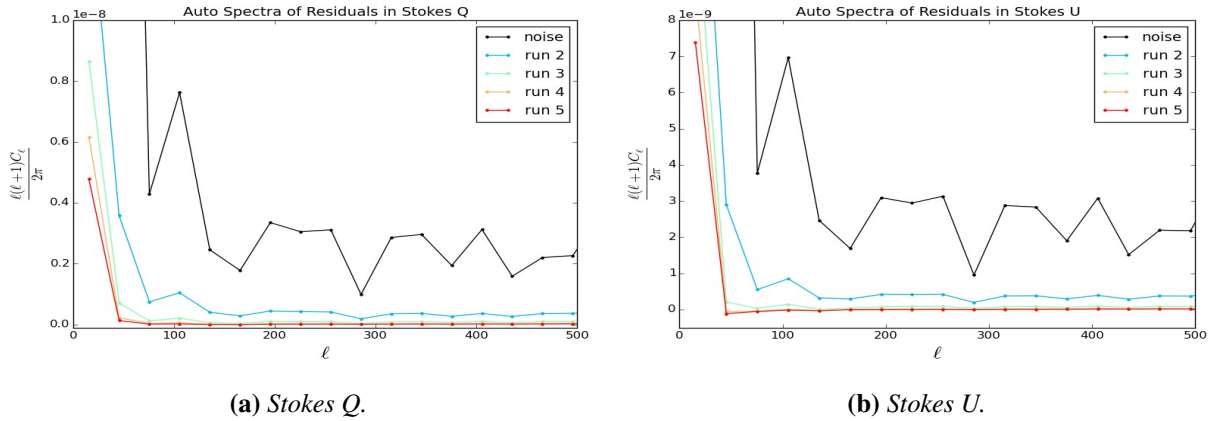


**Figure 4.11:** Auto spectra of the residuals after each run and the auto spectrum of the injected artificial signal (denoted as ‘noise’) in Stokes Q and U, binned by  $\ell = 30$ .

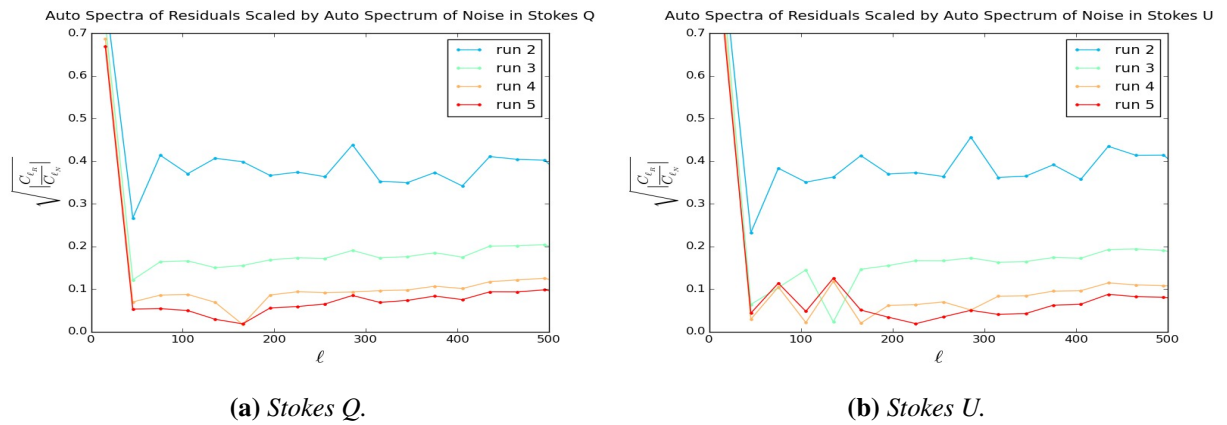


**Figure 4.12:** The square root of the ratio between the auto spectra of the residuals after each run, and the auto spectrum of the injected artificial signal (denoted as ‘noise’) in Stokes Q and U, binned by  $\ell = 30$ .

The cross correlation between the injected artificial signal and the residual also decreased with each successive run until convergence was achieved. Figure 4.13 shows this correlation, and Figure 4.14 shows the cross correlation scaled by the auto spectrum of the injected artificial signal. The cross correlation between the residual and the original injected artificial signal after 5 Ninkasi runs is only a few percent, and given that this is low compared to other instrumental systematic errors, we can conclude that the Stokes Q and U maps have converged sufficiently within 5 Ninkasi runs.

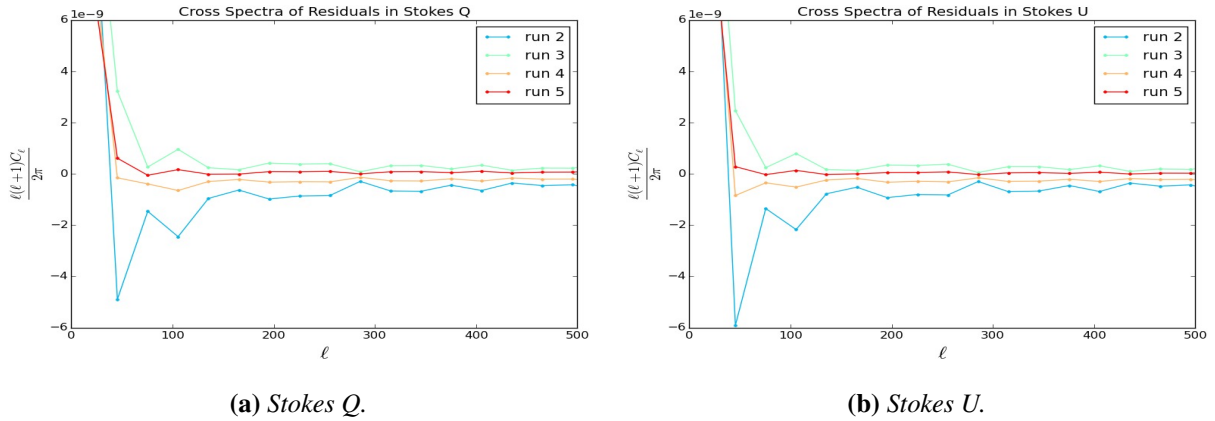


**Figure 4.13:** The cross correlation between the residuals and the injected artificial signal in Stokes Q and U, binned by  $\ell = 30$ .

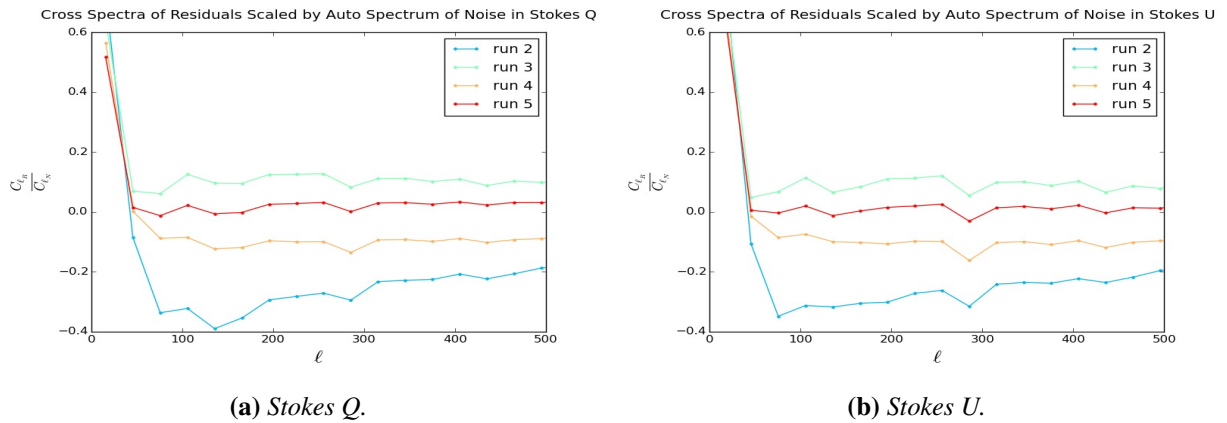


**Figure 4.14:** The ratio between the cross correlated signal and the auto spectrum of the injected artificial signal (denoted as ‘noise’) in Stokes Q and U, binned by  $\ell = 30$ .

## 4.2 Data Consistency Tests

We tested the self-consistency of our data by performing jackknives, where we split the data in half and investigated the power spectrum of the differenced halves. These tests allowed us to probe for various types of inconsistencies in our data. Long term system drifts were probed with jackknives of interleaved months, while diurnal variations were checked with jackknives of day against night time data. Signal chain inconsistencies were probed by jackknifing receiver channel 1 against receiver channel 2, where these are defined by the different signal chains in the re-

ceiver used to measure the Stokes parameters. Thus, for example, we are able to jackknife Stokes I channel 1 with Stokes I channel 2, which corresponds to jackknifing the left and right polarized intensity measured by the radiometer (see section 2.3 of Chapter 2 for more information on C-BASS receiver). Further tests to be conducted in future include tests for pointing consistency by jackknifing scans at different speeds, and tests for ground contamination by jackknifing scans at different elevations. The remainder of this section will present and discuss results from jackknives used to test long term system drifts, diurnal variations, and signal chain inconsistencies.

### 4.2.1 Jackknife Results

A successful jackknife test would result in a power spectrum that is consistent with the expected level of noise. Some residual signal could be acceptable, depending on the data split, given that it is highly unlikely that the signal levels in the two maps would be exactly equal. One would expect the signal chain jackknife to be the easiest to pass, as the data in this jackknife was recorded under the exact same conditions. By contrast, a day vs night jackknife represents two data sets taken under very different conditions with different temperatures, atmospheric conditions etc to contend with. Of course, the presence of unflagged RFI could cause any jackknife to fail, provided it is present in one data split and not the other. In order to determine the success or failure of a jackknife test, we wish to compare the power spectrum of the differenced data set to that of the expected noise in our data. Unfortunately, we have not yet developed the simulation machinery required to assess signal leakage and the comparison with the expected noise is still a work in progress and beyond the scope of this thesis. The tests presented in the remainder of this thesis were made as a proof of concept and as such, we have sent the data through a single 500 iteration Ninkasi run. This means that it is possible that some of the results could be affected by a lack of convergence in the map making process. When we have all of the jackknife test machinery in place, these tests will be conducted over multiple runs to ensure that the maps have properly converged before the power spectra are investigated.

Thus far, we have produced data sets using the low-level time ordered data analysis pipeline

as discussed in Chapter 3, split these data sets according to the criterion discussed previously, and differenced the data splits. Then we calculated the power spectra of the two original data splits as well as the power spectrum of the residual signal remaining after differencing the split data sets. Finally, we compared these power spectra and looked for cases where the power spectra of the two data splits varied greatly, resulting in spikes and other features.

#### 4.2.1.1 Interleaved Months Test

Some additional masking was required in order to prepare our data sets for the jackknife test. The presence of the sun and moon in our data would cause our jackknife tests to fail spectacularly as the position in the sky of these bright radio sources is not consistent over time. It was thus necessary to mask all pixels within thirty degrees of these sources. It is also unreasonable to expect other bright sources such as the Galaxy to cancel out perfectly when differencing them, so a mask with a threshold of  $0.05 K$  was applied to the data before determining the power spectra. In each power spectrum calculation, the two halves were first normalised by the number of hits in each pixel. The plots in Figure 4.15 show the Ninkasi output maps of the jackknifed data from the long term drift tests where data from interleaved months was jackknifed for Stokes I, Q and U. These plots show evidence of bad data that occurred in one half but not the other in all of the Stokes maps. For example, all of the plots in Data Split 1 exhibit a large streak in the upper left hand quadrant that is not evident in any of the Data Split 2 plots. The plots in Stokes I show streaks in an 'X' shape centered on bright sources (the sources have been masked). All plots in the figure exhibit random diagonal streaks and the plot of Stokes I in Data Split 2 also contains horizontal stripes which are not present in any of the other plots. It is likely that these events occurred in one or two single survey schedules as they are very localised. The streaking around bright sources could be caused when a schedule contains both bright sky sources and a large amount of RFI. As such, more careful pruning of the list of acceptable schedules is required. Figure 4.16 shows the power spectra resulting from these tests with the power spectra of each subset as well as the power spectrum of the differenced data set.

## Interleaved Months Jackknife

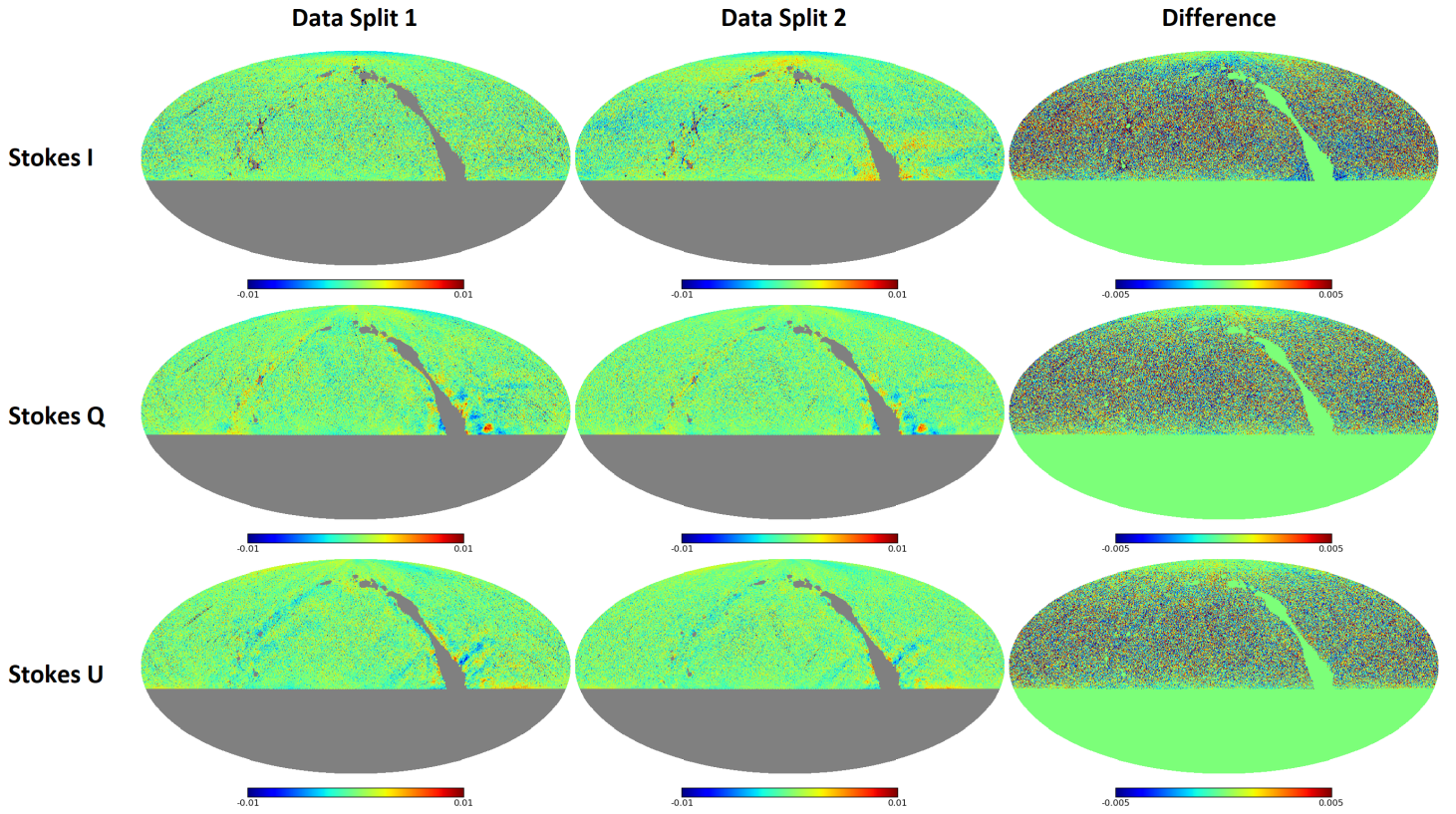
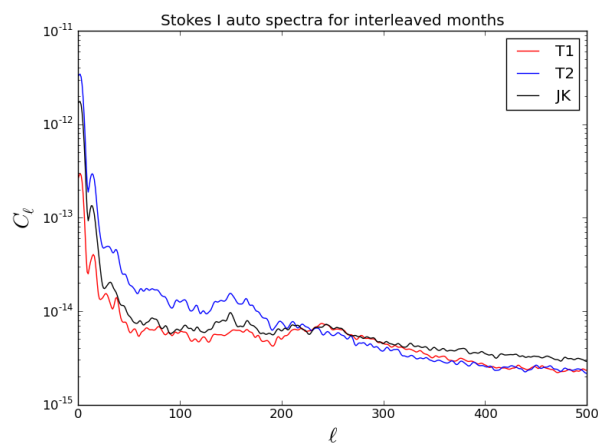
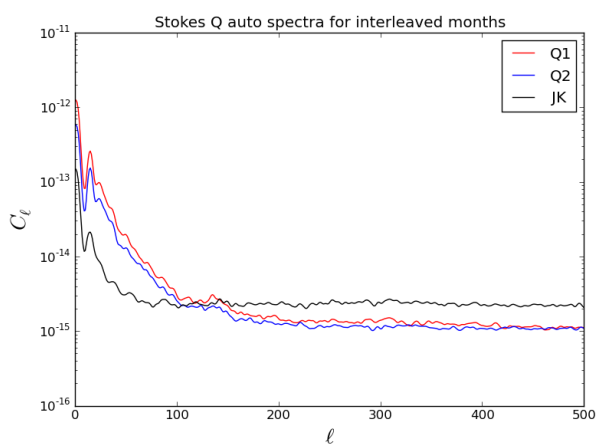


**Figure 4.15:** Ninkasi output maps of the interleaved months jackknife of the full data set, showing each half and the difference between them for Stokes I, Q and U. The temperature scale is in Kelvin.

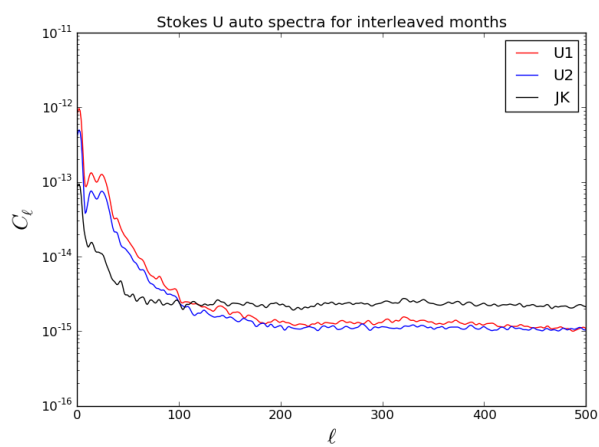
There are two likely causes for the streaks of bad data evident in Figure 4.15: either some RFI went undetected and contaminated the data, or too much signal was flagged as a result of a large RFI presence in the data, resulting in a poorly sampled ground template. In the case of the latter, identifying and removing schedules with a high RFI flagging percentage would remove these defective ground templates. It would also assist in treating the former case, as RFI is more likely to go undetected when there is so much of it that the actual sky signal is difficult to identify. The large peaks around  $\ell \approx 15$  in all three plots of Figure 4.16 suggest that there is a large scale feature in each of the data sets, and this likely indicates the presence of bad ground templates. In order to test this, we repeated the interleaved months jackknife test, but this time we did not include schedules where more than 60 % of data was flagged as RFI. The more RFI present in a



(a) Stokes I.



(b) Stokes Q.



(c) Stokes U.

**Figure 4.16:** The power spectra of the interleaved months jackknife for the full data set in Stokes I, Q and U, where JK is the power spectrum of the jackknifed dataset.

schedule, and therefore the higher the RFI flagging fraction, the more unreliable that data would be. Various cuts of different flagging fractions were tried, and it was decided to use the 60 % cut as a compromise between the amount of data lost and the amount of bad quality data allowed. The 60 % cut removed just under 15 % of the data.

Figure 4.17 shows the Stokes I, Q and U maps of the jackknifed data for the interleaved months test with the 60 % RFI contamination limit applied. It can be seen that the RFI events evident in full data set test (Figure 4.15) are not present here and the striping caused by bad ground templates has also been removed. It must be noted that the maps shown in Figures 4.15 and 4.17 are not sky maps, but Ninkasi output maps, which means that they represent the difference between the actual sky map and the input estimate. As the input estimate is the same in all cases for the jackknife tests, it is more useful to look at the Ninkasi output maps rather than the full sky maps as the output maps are not completely dominated by the sky signal and differences are therefore clearer to the human eye. Figure 4.18 shows the power spectra results for this test and shows good improvement over those in the full data set test (Figure 4.16), with the two halves of split data much more closely aligned and the plots having much smaller peaks. The overall power on large scales ( $\ell < 40$ ) appears to have increased, but this is likely a result of the difference in the number of hits between the data used in Figure 4.16 and Figure 4.18. What is important to note is that the peaks around  $\ell \approx 15$  have disappeared and the difference curves are smoother. The remainder of the work in this section is based on data with the 60 % RFI contamination limit applied.

#### 4.2.1.2 Diurnal Variations Test

The plots in Figure 4.19 show the maps of the jackknifed data from the diurnal variations test where data from day and night time was jackknifed for Stokes I, Q and U. These results are not quite as good as those from the interleaved months test, as there is a larger difference in the power spectra shown in Figure 4.20 on large scale ( $\ell < 40$ ). This could indicate a need to use different ground templates between day and night, or we may need to flag data further from the sun. We

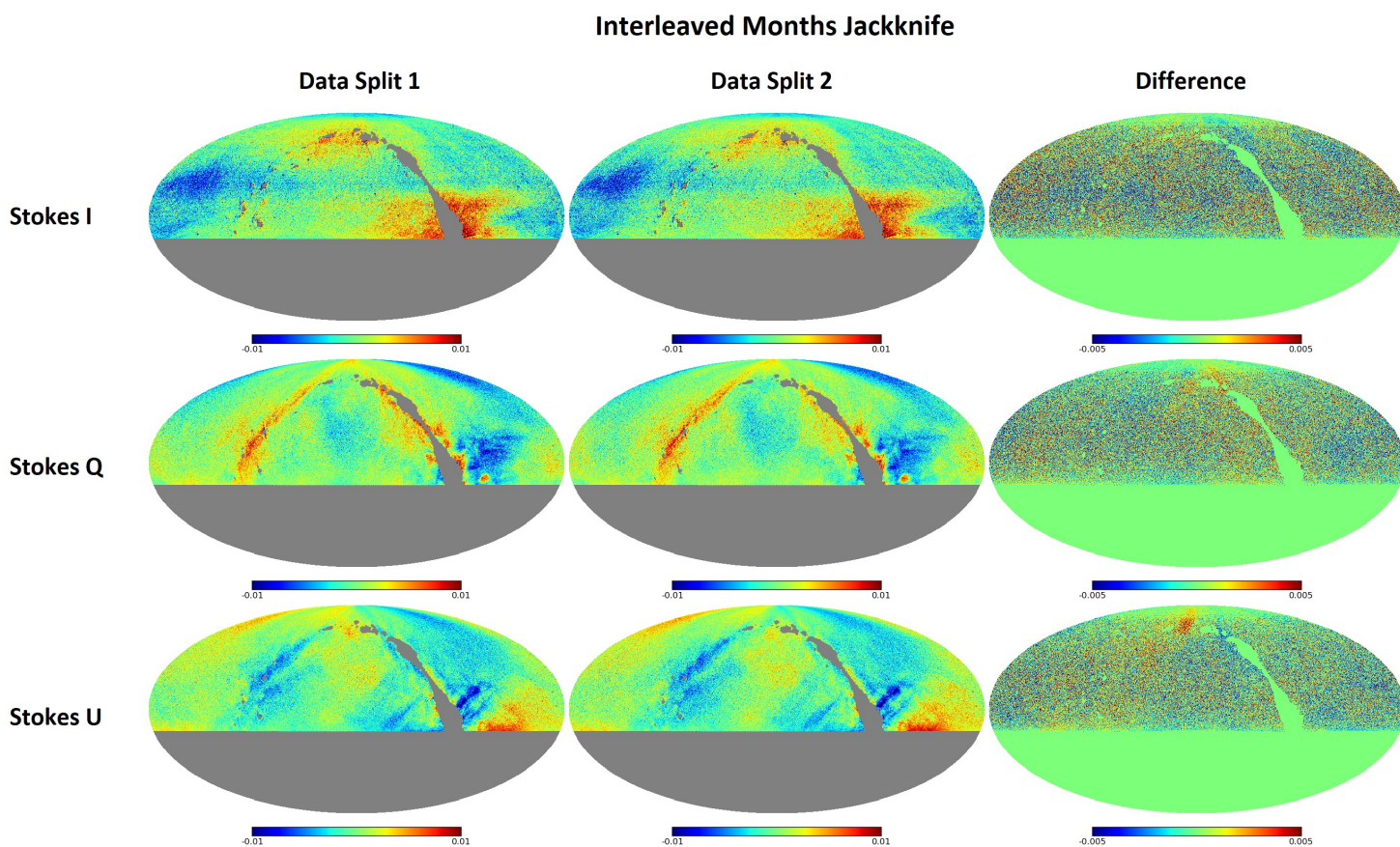
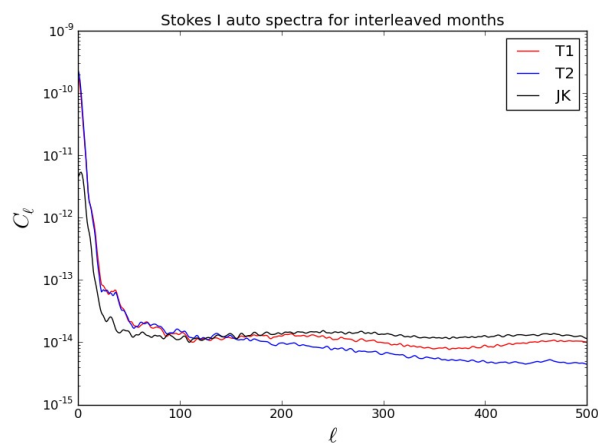
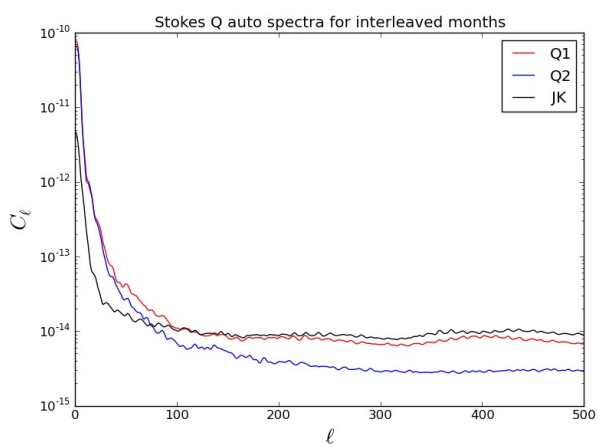


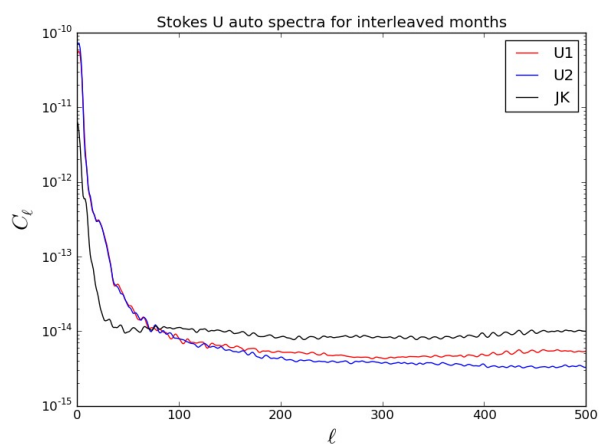
**Figure 4.17:** Ninkasi output maps of the interleaved months jackknife for data with less than 60 % RFI flagged, showing each half and the difference between them for Stokes I, Q and U. The temperature scale is in Kelvin.



(a) Stokes I.



(b) Stokes Q.



(c) Stokes U.

**Figure 4.18:** The power spectra of the interleaved months jackknife for data with less than 60 % RFI flagged, in Stokes I, Q and U.

currently flag all data within 30 degrees of the sun, but this radius will need to be increased.

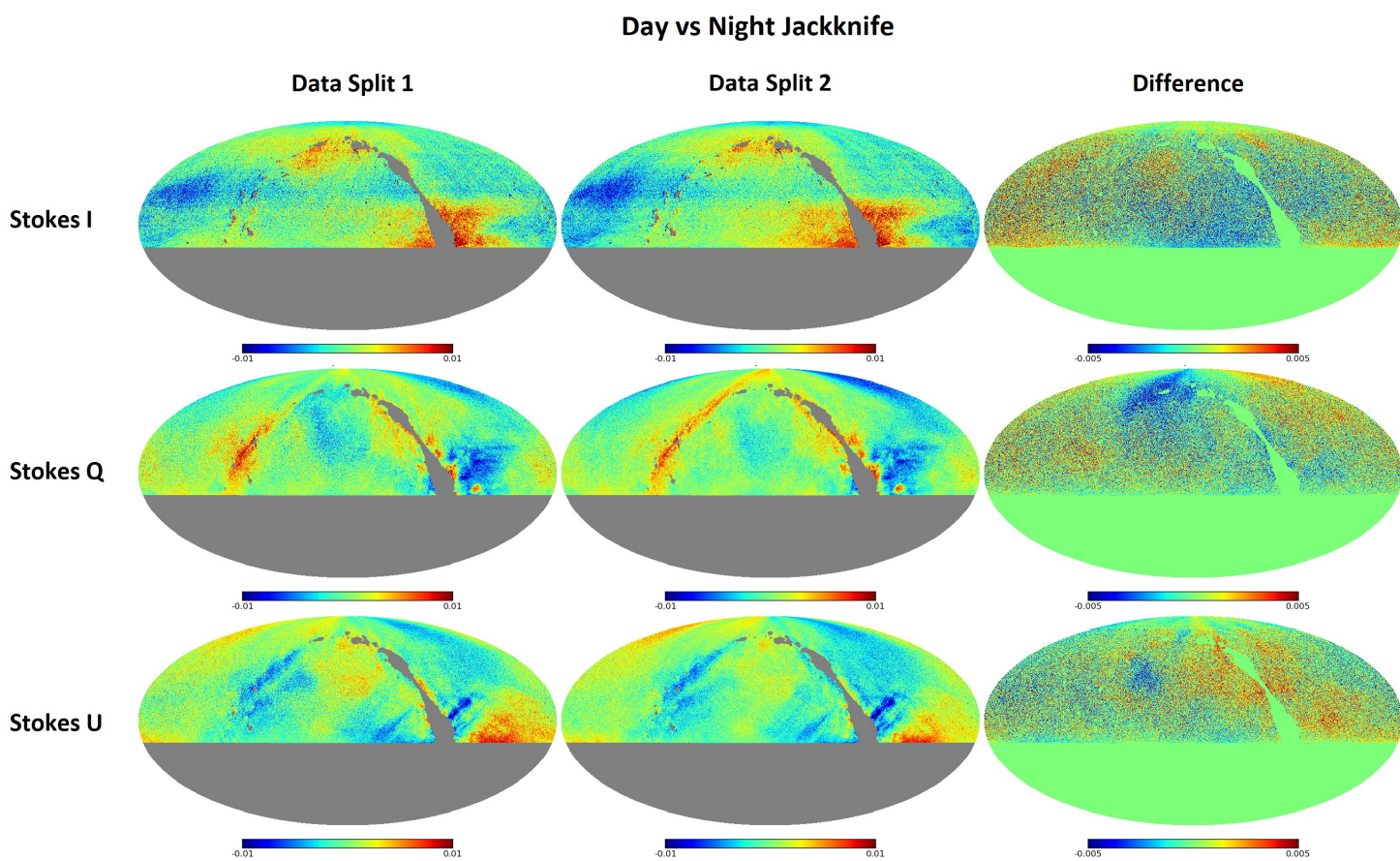


**Figure 4.19:** Ninkasi output maps of the day and night jackknife showing each half and the difference between them for Stokes I, Q and U. The temperature scale is in Kelvin.

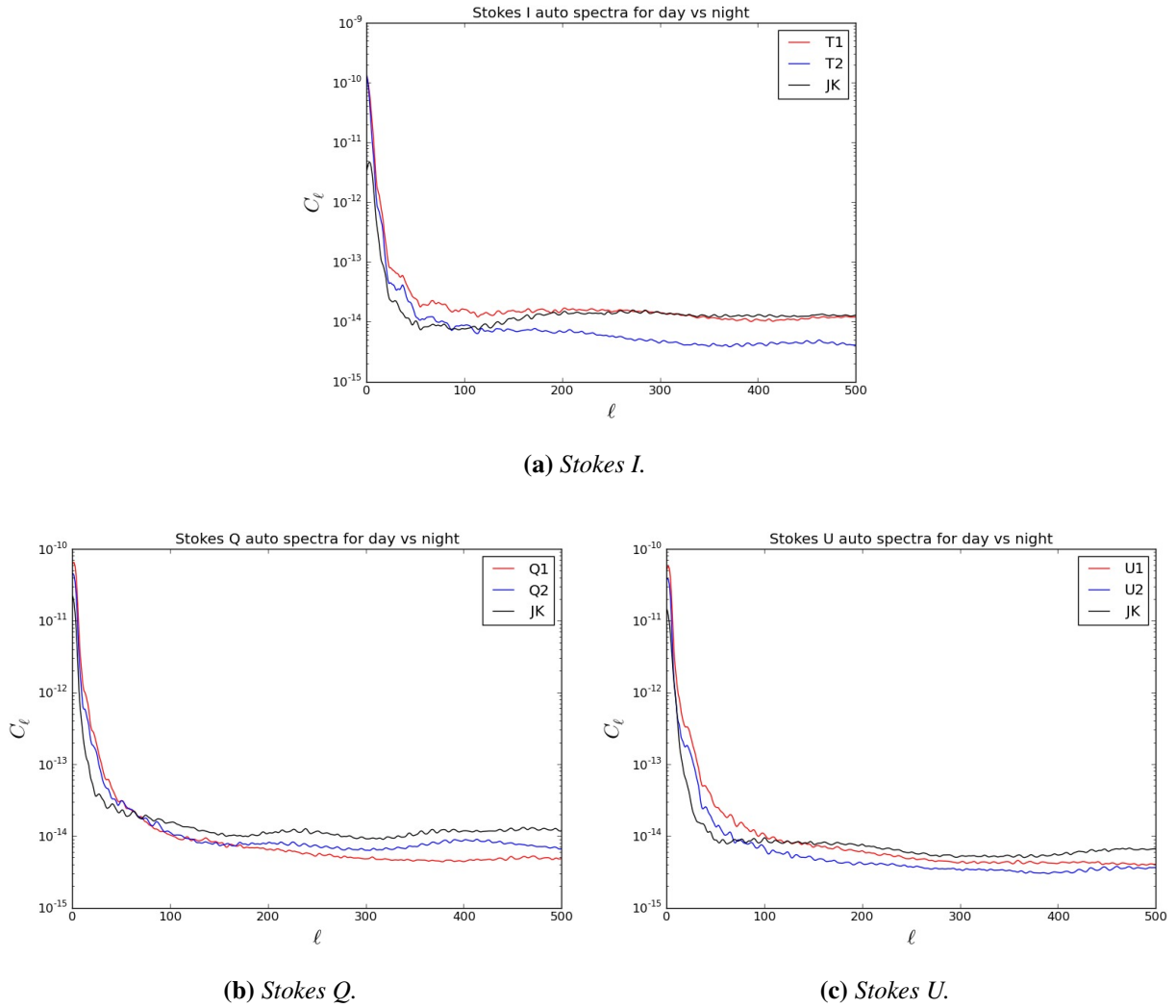


**Figure 4.20:** The power spectra of the day and night jackknife in Stokes I, Q and U.

#### 4.2.1.3 Signal Chain Test

The plots in Figure 4.21 show the maps of the jackknifed data from the signal chain inconsistencies test where data from each signal chain was jackknifed for Stokes I, Q and U. Figure 4.22 shows the power spectra resulting from these tests. The data in these jackknife splits were taken under identical conditions and as such, the only possible points of failure are in the signal chains themselves or in the data analysis pipeline. As such, a poor performance in this test would be a very concerning. Fortunately, the results for this test are very good, especially in Stokes Q and U, with very little power seen in the difference plots beyond  $\ell \approx 10$ , however, there is evidence

of features, as opposed to just white noise, in both the difference maps and the power spectra that may warrant further investigation. Note that the power in the jackknifed data set was very small, as the power spectra of the two data subsets were almost identical. This is particularly evident in Stokes Q and U where the power spectrum of the jackknifed data set is much lower than either subset.

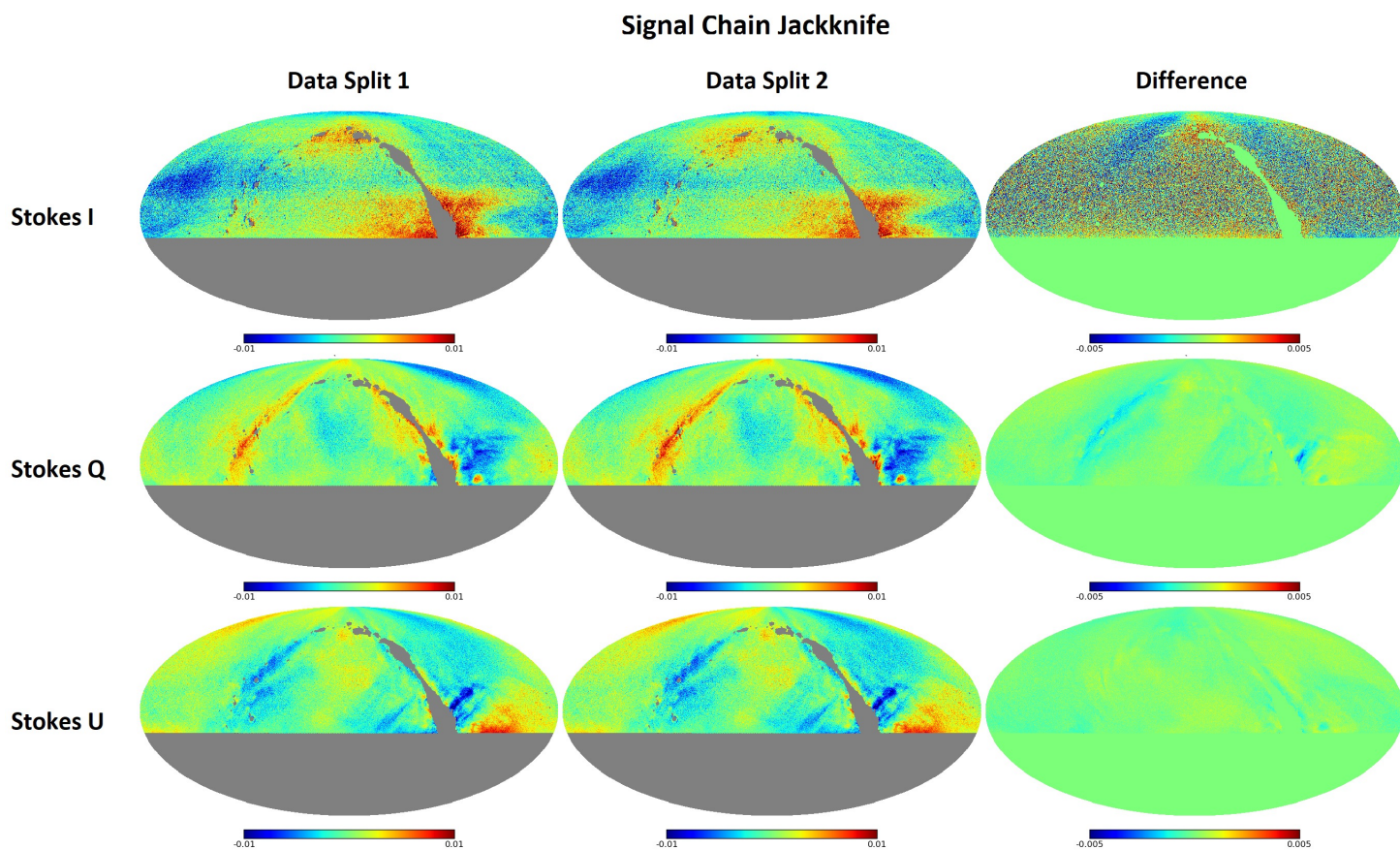


**Figure 4.21:** Ninkasi output maps of the signal chain jackknife showing each half and the difference between them for Stokes I, Q and U. The temperature scale is in Kelvin.

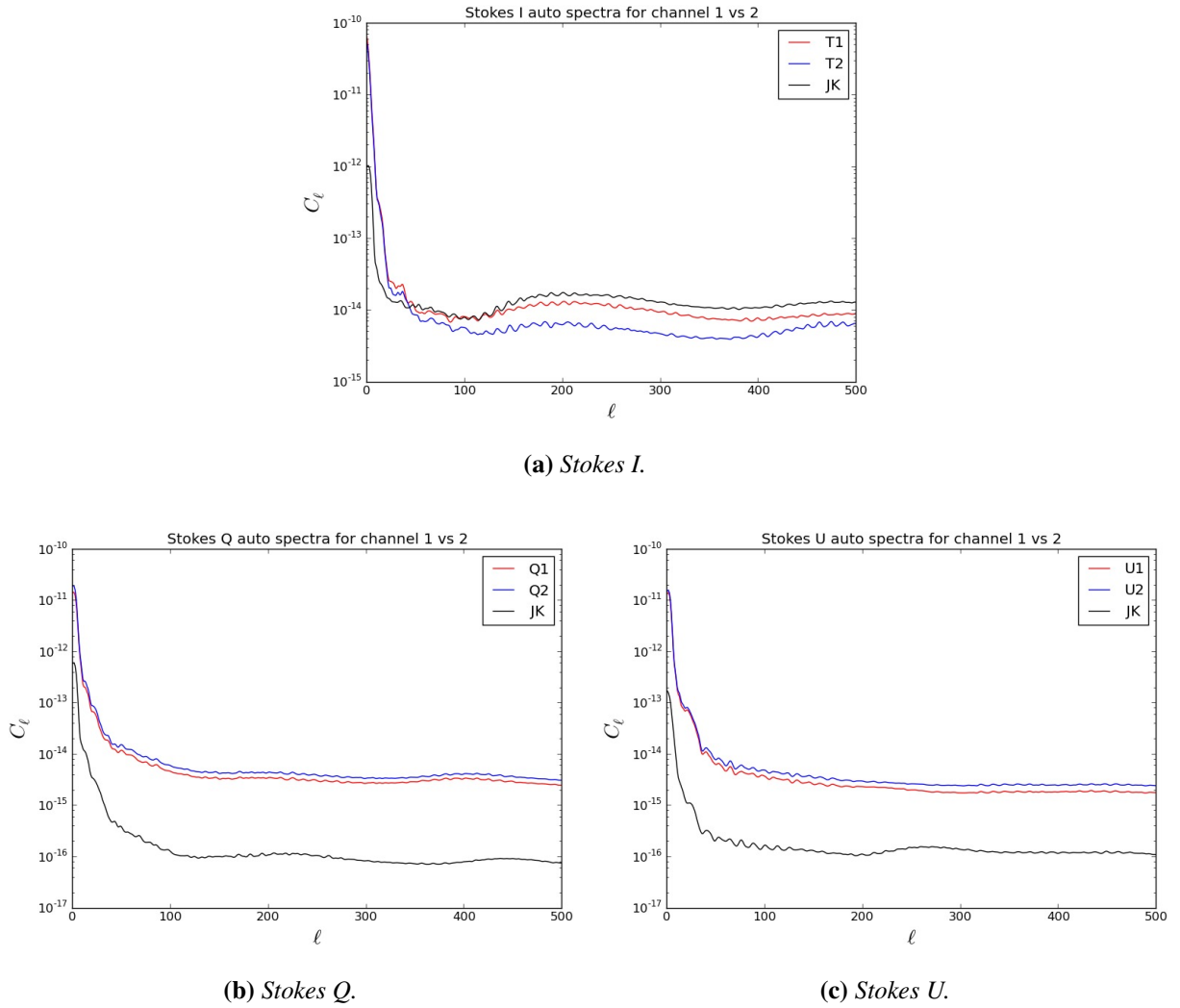


**Figure 4.22:** The power spectra of the signal chain jackknife in Stokes I, Q and U.

#### 4.2.1.4 Azimuth Scan Direction Test

The plots in Figure 4.23 show the maps of the jackknifed data from the scan direction test where data from the telescope scanning in opposite directions was jackknifed for Stokes I, Q and U. Figure 4.24 shows the power spectra resulting from these tests. These results are remarkably good, especially on large scales, although perhaps this should not be unexpected as the measurements were taken under very similar conditions, with the only difference being the direction in which the telescope was moving. There are some features evident in the power spectra, particularly around  $\ell \approx 40$  in all three plots in Figure 4.24, and around  $\ell \approx 20$  for Stokes Q and U. These

features have been evident in all of the jackknifed power spectra and thus could be evidence of residual signal in the best case, or evidence of bad data at those angular scales in the worst case. This will be investigated once the signal leakage and noise comparison techniques have been developed.

The scan direction jackknife test would fail if there were pointing inaccuracies in the data, and given the fact that pointing inaccuracies were encountered during the RFI flagging process, as discussed in Chapter 3, it may seem strange that there is no evidence of them in these results. This is because the pointing inaccuracy problem only occurred around bright sources, and those have all been flagged for this analysis. It will be worth investigating this further once the pointing inaccuracy has been addressed in the low-level time stream processing pipeline.

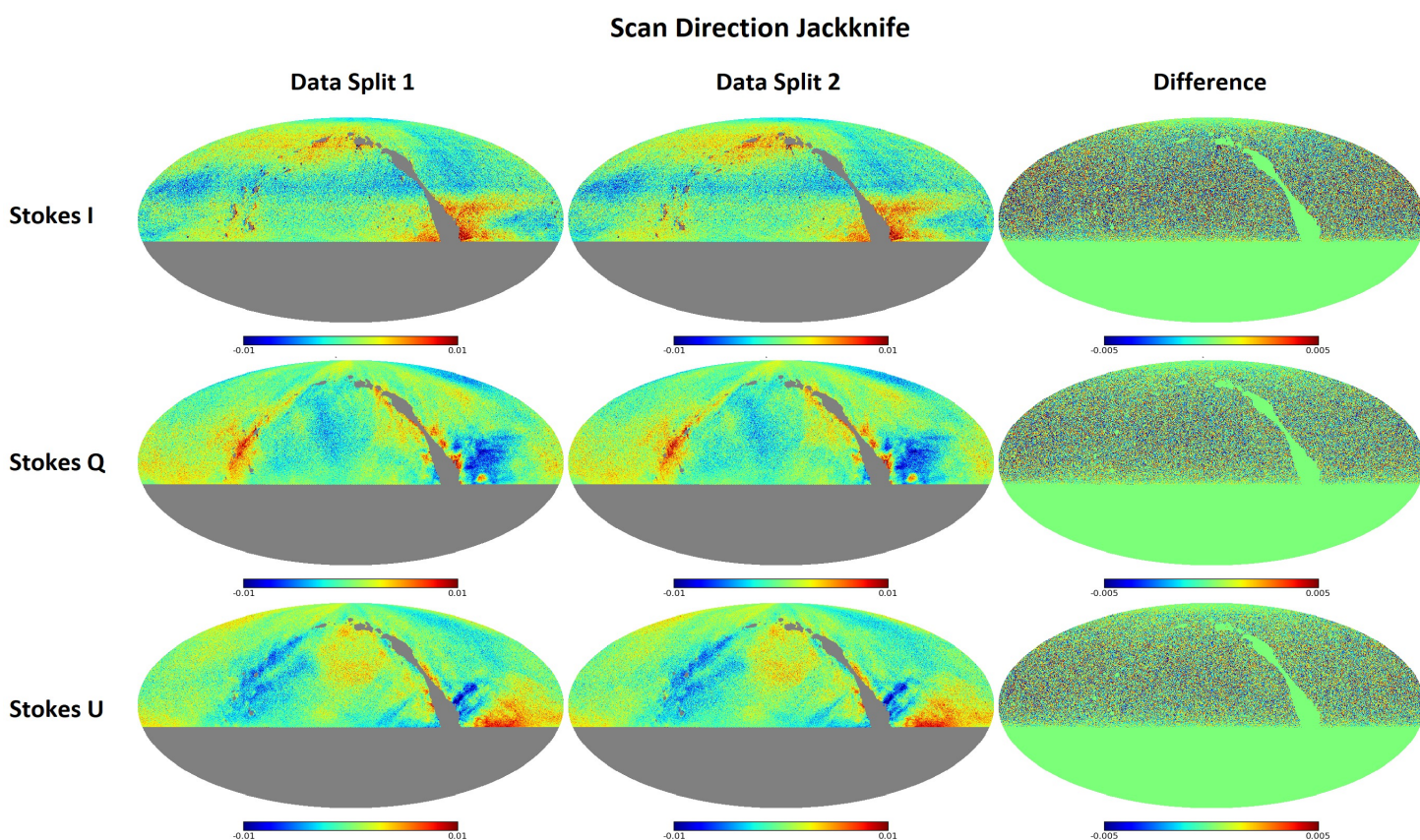


**Figure 4.23:** Ninkasi output maps of the scan direction jackknife showing each half and the difference between them for Stokes I, Q and U. The temperature scale is in Kelvin.

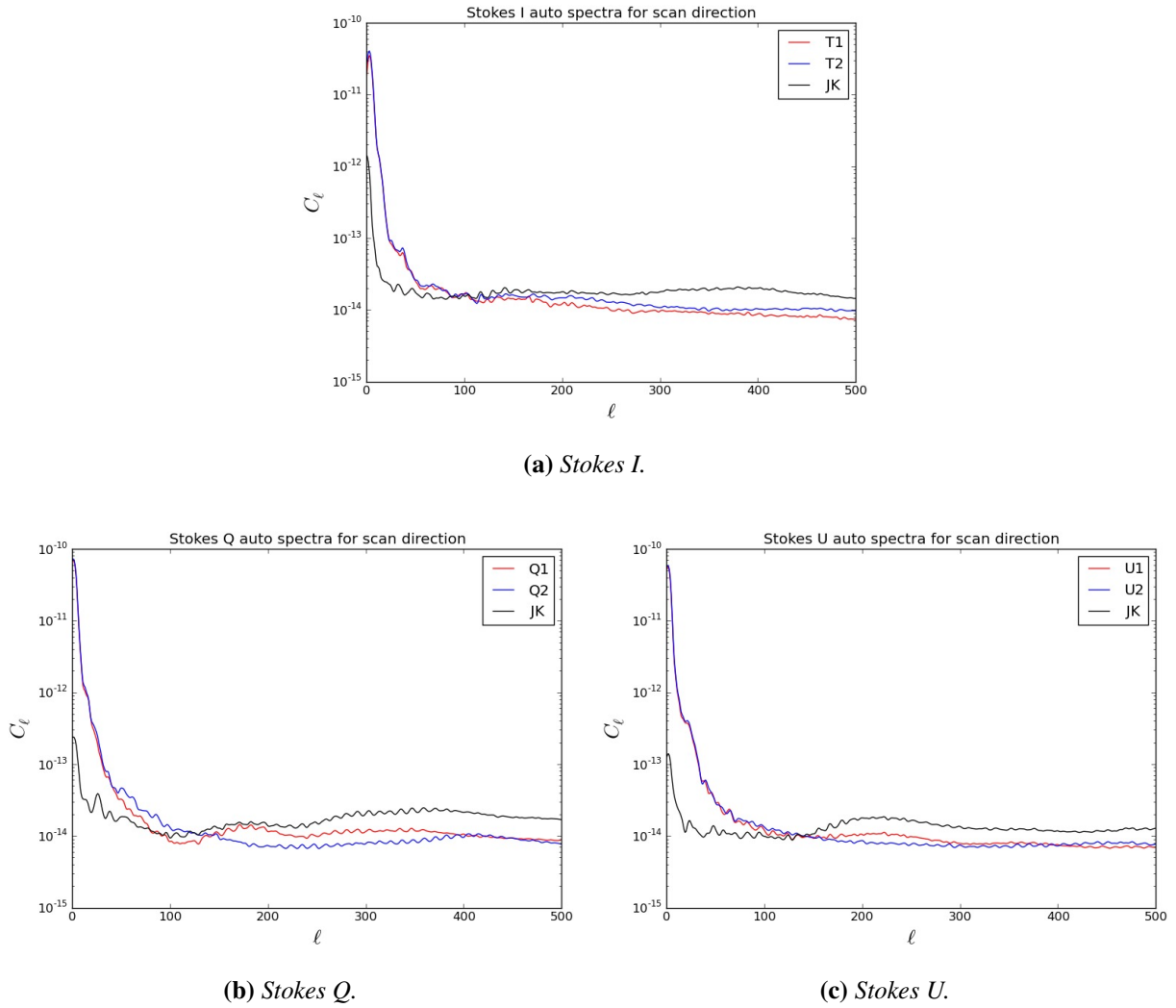


**Figure 4.24:** The power spectra of the scan direction jackknife in Stokes I, Q and U.

### 4.3 Summary and Conclusions

In this chapter, I have discussed various map making methods, and have described the two methods used by the C-BASS collaboration. I have also described the data consistency tests that I have conducted, specifically Ninkasi convergence tests, and data jackknife tests. These tests are designed to test the scientific quality of our data by ensuring that there are no systematic errors and inconsistencies therein. The convergence tests showed that our intensity sky maps converged to a few percent of any injected artificial signal within 12 runs of 500 iterations, while our po-

larization sky maps converged to a similar level within 5 runs of 500 iterations, proving that our Ninkasi map making program can produce high fidelity maps of the data, regardless of errors in the input model. The jackknife tests showed that consideration must be taken when choosing which data to include in the map, as certain schedules containing a large amount of RFI are untrustworthy and contain bad data. They also showed that it could be necessary to use different ground templates between day and night, or to flag data further from the sun than we currently do. The jackknife tests showed that the low-level data analysis pipeline has improved the quality of our data. A collaboration member is conducting jackknives using DESCART. Comparisons between the jackknife results in DESCART and Ninkasi will be made in due course.

# Chapter 5

## Commissioning the Southern System

In this chapter I will describe the technical and commissioning work that I performed with the southern system. I will discuss how we set the alignment of the primary and secondary reflectors, as well as the process of calibrating the optical and radio pointing, and I will describe the system that I developed that allows us to perform optical pointing from a remote location. I will also give an overview of the RFI environment at Klerefontein.

### 5.1 Commissioning the Southern System

The receiver, now situated on site in Klerefontein, was originally commissioned on an identical antenna at the Hartbeesthoek Radio Observatory (HartRAO). This was done because the location was far more easily accessible than the site at Klerefontein and because of the infrastructure that already existed at HartRAO, which did not yet exist at Klerefontein. While at HartRAO, I was able to work on primary and secondary reflector focusing, beam mapping and a host of other tasks while familiarising myself with the instrument. Our main task was to ensure that the system ran accurately and reliably over a reasonable period of time (a few months). Once this was achieved, the receiver was relocated to Klerefontein. While the receiver was being commissioned in HartRAO, we were also working at Klerefontein to ensure that the antenna operation was all in order and ready for the receiver. The receiver was moved to Klerefontein in May 2014.

Figure 5.1 is a map of South Africa, showing the location of Klerefontein and also showing the extent of Vodacom 3G cellphone coverage in South Africa. This map highlights how isolated Klerefontein is from any large settlements, thus limiting the amount of RFI prevalent in the area.

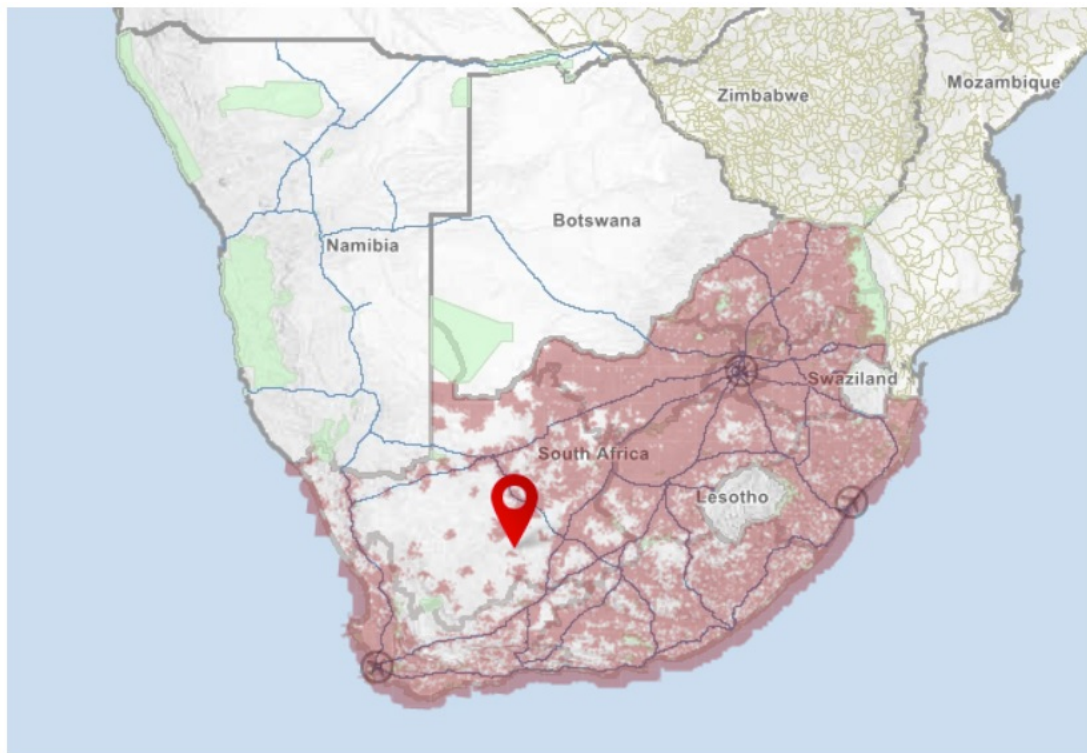


**Figure 5.1:** A map of Vodacom 3G signal coverage in South Africa, showing the location of Klerefontein. The lack of cellphone coverage in the area surrounding Klerefontein is one of the key reasons for the selection of the site for C-BASS. The map was created on the website <https://vccoverage.afrigis.co.za>, accessed on 01 November 2017.

Once the receiver had arrived in Klerefontein, it had to be tested to ensure that it had survived the journey without damage. We set up the receiver on some scaffolding, far enough from the antenna to be unaffected by its presence. Figure 5.2 shows the C-BASS South site during early commissioning, with the scaffolding positioned away from the telescope, while Figure 5.3 shows the receiver mounted on the scaffolding test rig. Measurements of the receiver output were taken at various stages along the signal chain using a spectrum analyser and compared to similar measurements taken at HartRAO to ensure that the receiver was still operating as expected. Load

tests were also conducted by covering the receiver with a thick sheet of eccosorb to test receiver response. Once we were satisfied that the receiver had survived the trip with no ill effects, we mounted the receiver onto the dish, cooled it down and took first light at Klerefontein.



**Figure 5.2:** A photograph taken during the on site commissioning of C-BASS South. The scaffolding where the initial receiver testing took place can be seen on the left.



**Figure 5.3:** The receiver test rig. We set the receiver up on some scaffolding away from the antenna and ran some preliminary tests to ensure that the receiver had survived the trip to site.

C-BASS South has suffered a litany of problems during its commissioning phase, which were aggravated by the remoteness of its location, meaning that problems would remain unaddressed until a collaboration member could arrive on site. Some of the biggest difficulties we've had to

overcome include a lightning strike on the weather station—which caused considerable damage to various electronic components in the control room—hard drive failures, and multiple compressor and chiller failures. After the lightning strike, we took added precautions by placing a copper earthing mat under the new weather station and optically isolating every electronic component we could. Hard drive failures were countered by adding a backup computer to the network that could take over when needed. The C-BASS computer network includes a control computer, responsible for the operation of the telescope, a data computer with minor data analysis capability, responsible for storing and distributing data, and a gateway machine, which is the only access to the network from the outside world. We added another computer to this network, which contained backups of all the other machines and its own private network access, so that this machine could be accessed even if the gateway computer was down. The compressor failures were caused by multiple electricity supply failures. There is a backup generator at Klerefontein, but it takes a few seconds to establish a stable supply of electricity, and the fluctuations in electricity supply caused several compressors to burn out. This was countered by placing all of the C-BASS electronics behind a very large UPS system, which keeps the supply of electricity constant.

### **5.1.1 Commissioning C-BASS South Optics**

We were able to alter the position and shape of the primary reflector, as well as the position and orientation of the secondary reflector in order to maximize the antenna gain and optimize the beam shape. The adjustments that were made to properly focus the primary and secondary reflectors are discussed in this section.

#### **5.1.1.1 Focusing the primary reflector**

The northern primary reflector was a single piece reflector while the southern one was a segmented reflector made up of twelve adjustable panels. The ideal primary reflector shape for the southern system, designed to optimise antenna forward gain, was modelled by collaboration member Christian Holler. He derived a best fit model, Equation 5.1, using photogrammetry data. The panels of the southern primary reflector needed to be adjusted so that the surface matched a

shape described by this equation, in order to focus the reflector.

$$z(r) = -0.000524r^5 + 0.004680r^4 - 0.016472r^3 + 0.120840r^2 - 0.015305r \quad (5.1)$$

where  $z$  is the depth of the reflector as a function of radius  $r$ . The exact position of each panel was measured using photogrammetry, a technique that uses photographs of the panels from different angles to determine their position. An example of a photograph used in this analysis is shown in Figure 5.4. Reflective markers were placed at various points on each panel, and photogrammetry could only be performed at night for maximum contrast between the dish surface and the reflective markers. These markers provided specific data points used in modelling the dish surface. A 3D point model of the dish surface was produced from the photographs, using a program called PhotoModeler \*. This model was then fitted to the function in Equation 5.1 using MATLAB and the offset from the required shape was calculated, allowing the required panel adjustments to be determined. This work was the primary focus of collaboration member Johannes Allotey, and the reader is referred to his MSc thesis, Commissioning and Characterisation of the C-Band All-Sky Survey Southern Telescope, for more information.

### 5.1.1.2 Focusing the secondary reflector

The secondary reflector is mounted in a foam cone which is bolted directly onto the feedhorn, as shown in Figure 5.5, by three adjustable bolts. These bolts allow the position of the secondary reflector to be adjusted in terms of focal position, and tilt, both in azimuth and in elevation. The secondary reflector was focused by adjusting these bolts, and the result was tested by rastering over a bright source and investigating the resulting beam maps, with the aim of producing beam maps that were symmetrical. The moon was chosen as the source for rastering as it was the only bright radio source in the sky at the time that was far enough away from the sun.

The secondary reflector was initially set at the nominal focal point, with no tilt in azimuth or elevation. This meant there was a 12 mm gap between the flange on the horn and the base of the cone on all sides. We tested the focal length by adjusting this gap evenly, doing rasters at

---

\*PhotoModeler tool described in <http://www.photomodeler.com/products/modeler/default.html>



**Figure 5.4:** A photograph of the C-BASS dish, showing the reflective markers used in photogrammetry. These markers allow PhotoModeler to estimate the surface shape of the dish.

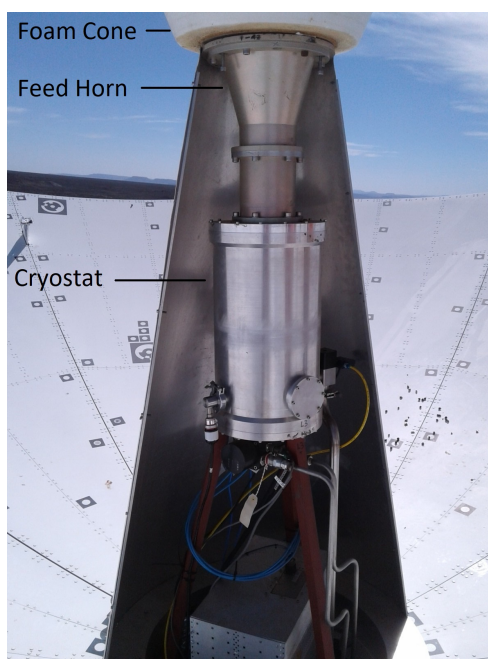
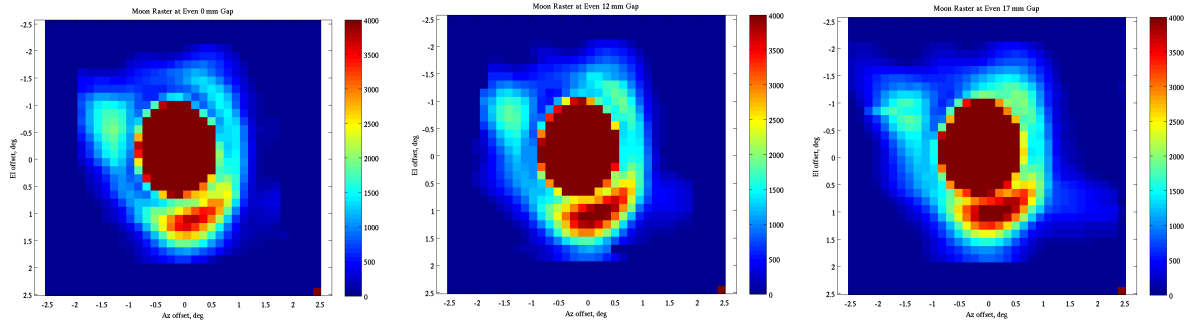


**Figure 5.5:** A photograph of the C-BASS receiver, mounted on the dish, with part of its covering removed. This photograph shows the very bottom of the foam cone that holds the secondary reflector in place, the feedhorn, and the cryostat. The one half of the protective cover and part of the primary reflector is also visible.

gaps of 0 mm, the maximum travel on the bolts (17 mm), and at the nominal focus of 12 mm. The resulting beam maps from these position adjustments showed that there was almost no discernible change in beam shape over the available position range. To test the effect of tilting the reflector in azimuth and elevation, we positioned the secondary reflector at the nominal focal length (12 mm gap), as this allowed us to adjust the azimuth and elevation tilt freely without being limited by the range of the adjustment bolts. We then tested the effect of azimuth and elevation individually, keeping one constant at the nominal focal position while tilting the other. For our final position, we interpolated our results, and decided to place the secondary reflector at a slightly lower focus, with a tilt towards the negative in both elevation and azimuth, as this produced the most symmetrical beam. The gap between the flange on the receiver horn and the base of the foam cone was measured at the cardinal points, and set to the values shown in Table 5.1, where positive and negative azimuth and elevation are defined when the receiver is pointed towards the horizon. Figure 5.6 shows the beam maps of a moon rasters after each secondary reflector position adjustment, with plots (a)–(c) showing the results from focal position changes, plots (d)–(g) showing the results of tilt changes, and plot (h) showing the result of the final secondary reflector position and tilt. The plot shown in Figure 5.6 (h) shows clear improvement over all the previous plots in the figure, with the first sidelobe showing less intensity and a more even spatial distribution. Note that while we have reduced the amount of power in the first side lobe, there is a three-fold symmetry that remains prevalent in all of these beam maps. This is most likely due to the primary reflector which is still undergoing photogrammetry adjustments. Once the primary reflector is in its final configuration, this exercise will have to be repeated in order to perfect our beam shape.

**Table 5.1:** *Secondary reflector position settings*

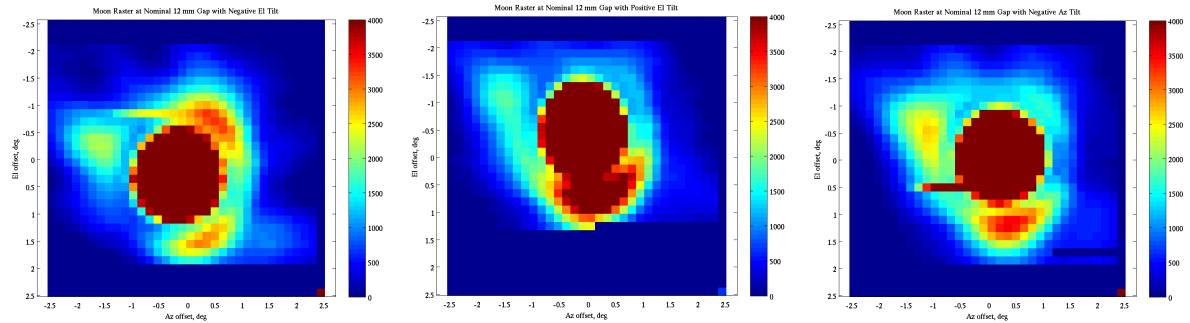
| Azimuth  |          | Elevation |          |
|----------|----------|-----------|----------|
| Positive | Negative | Positive  | Negative |
| 11.5 mm  | 5.5 mm   | 12 mm     | 4.5 mm   |



(a) Beam map of moon rasters with the secondary reflector positioned at the minimum (0 mm) gap.

(b) Beam map of moon rasters with the secondary reflector positioned at the nominal best (12 mm) gap.

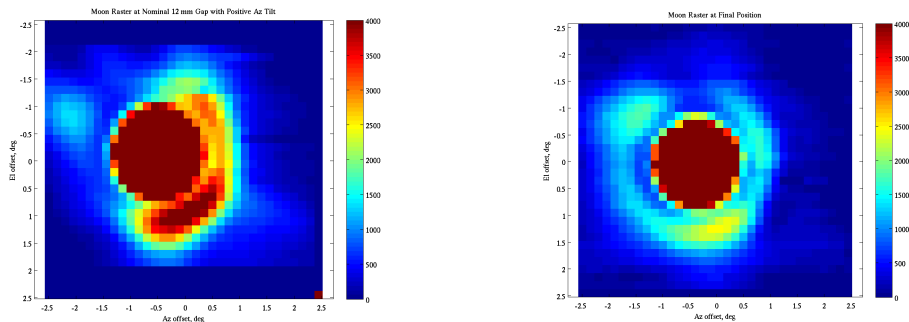
(c) Beam map of moon rasters with the secondary reflector positioned at the maximum (17 mm) gap.



(d) Beam map of moon rasters with the secondary reflector tilted negative in elevation.

(e) Beam map of moon rasters with the secondary reflector tilted positive in elevation.

(f) Beam map of moon rasters with the secondary reflector tilted negative in azimuth.



(g) Beam map of moon rasters with the secondary reflector tilted positive in azimuth.

(h) Beam map of a moon raster with the secondary reflector in its final position.

**Figure 5.6:** Beam maps of moon rasters, showing the results of the secondary reflector positional adjustments. Plots (a)–(c) show maps produced after adjustments in focal position. Plots (d)–(g) show maps produced after adjustments to tilt in azimuth and elevation. Plot (h) shows the map produced with the secondary reflector in its final position. At this point in the analysis pipeline, intensity is measured in backend units.

## 5.1.2 Optical Pointing

Antenna pointing accuracy was achieved using an online pointing model. This model was developed by setting the telescope to track a star, taking photographs to see what the telescope was pointing at and measuring the offset between the centre of the image and the position of the star. This process is called optical pointing. I was tasked with making it possible to perform optical pointing from a remote location. This meant that a camera had to be permanently mounted onto the telescope, with the requirement that the camera had to be protected from the elements, namely, wind, rain and direct sunlight. To this end, I designed an environmental enclosure and camera mount assembly, shown in Figure 5.7, that could be mounted onto the support frame of the dish.

### 5.1.2.1 Physical Setup

The setup consisted of a Mintron 12V6HC-EX CCD optical camera coupled to f4.5-5.6 300 mm Nikon zoom lens, housed inside a waterproof box and mounted on the rim of the telescope dish. The optical camera was electrically isolated from its 12 V DC power supply, meaning that the user had the ability to turn the camera on and off remotely. It was connected to the control PC with a CCTV cable and images from the camera were taken using a Sensoray 611 PCI frame grabber. The camera was protected from the sun by means of a shutter flap (see Figure 5.7a). This could be opened or closed remotely using a servo motor (Figure 5.7b), which was mounted to the side of the waterproof housing. A magnetic reed switch, attached to the flap, was used to detect whether the flap was open or closed. The waterproof housing, along with the shutter flap and servo motor, was attached to an aluminium base plate which held the camera and lens (Figure 5.7c). This was then bolted onto the telescope dish support frame (Figure 5.7d). The user interacted with the system by running one of several Python scripts which communicated with an Arduino microcontroller board that controlled the optical pointing system. These scripts allowed the user to switch the camera on and off, open and close the shutter flap, and check whether the flap was open or closed. This was achieved using the circuit shown in Figure 5.8, with the circuit diagram shown in Figure 5.9.



(a) Photograph of the environmental enclosure, showing protective flap, servo and magnetic reed switch system.



(b) Photograph of the environmental enclosure, showing the servo motor mounted on the side.



(c) Photograph of the optical camera mounted with lens on the enclosure base plate.



(d) Optical camera assembly mounted to the telescope dish support structure

**Figure 5.7:** Protective enclosure and camera mount assembly

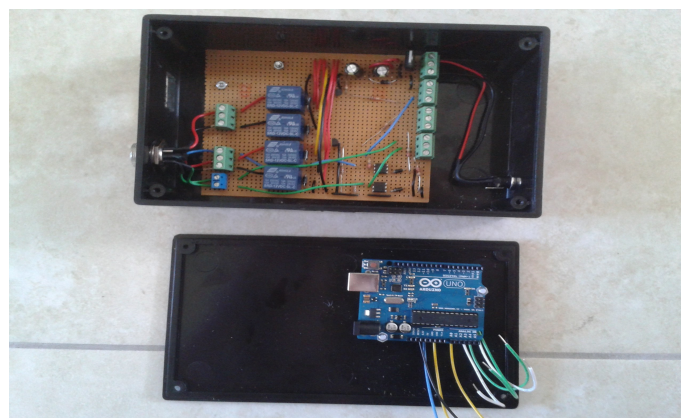


**Figure 5.8:** Photograph of the remote optical pointing control system.

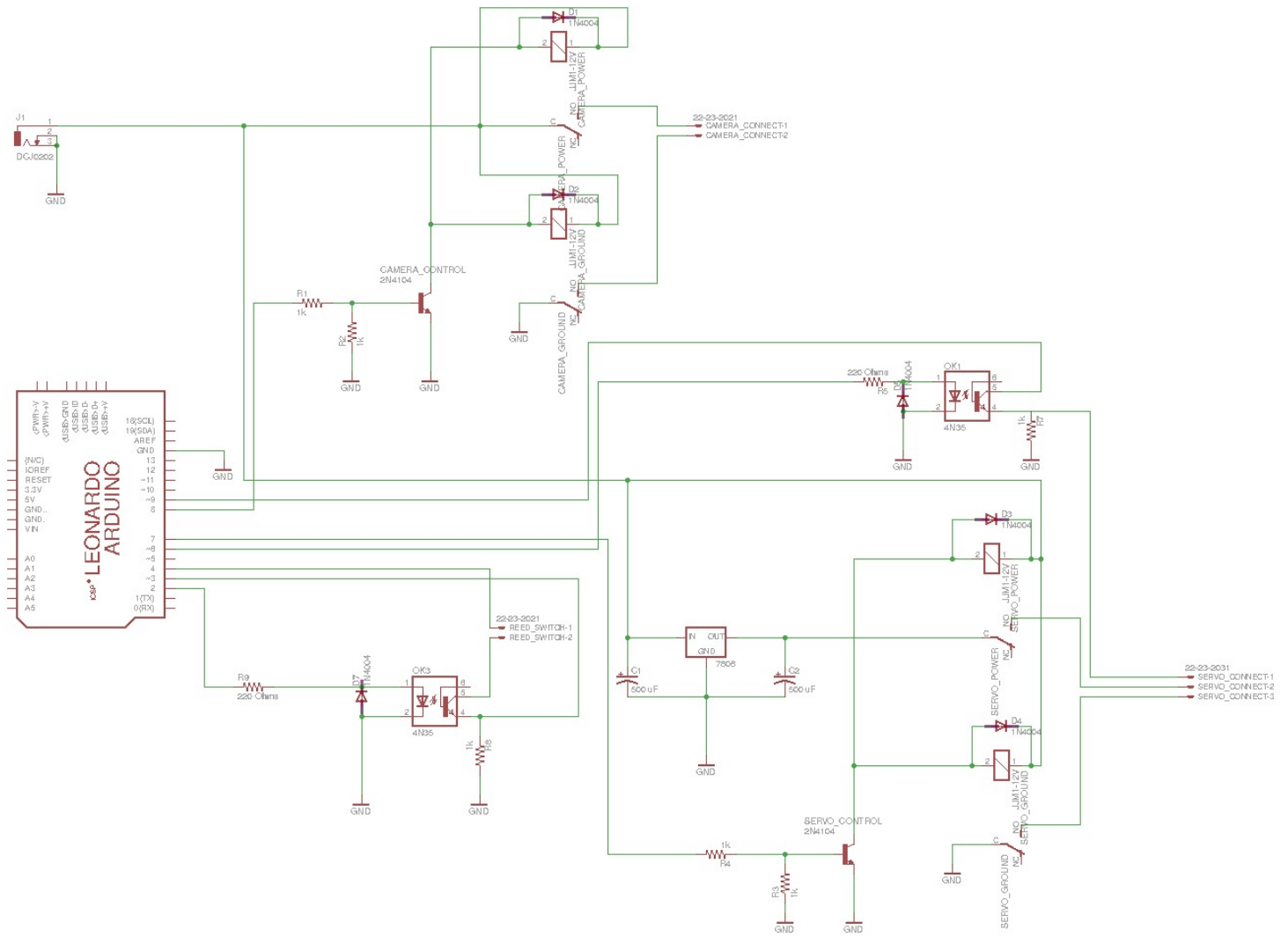


Figure 5.9: Schematic circuit diagram of the remote optical pointing control system.

### 5.1.2.2 Optical Pointing Strategy

The process of developing an optical pointing model for C-BASS North had been automated to a large degree by Stephen Muchovej, a collaboration member. This process was adapted for the southern instrument and re-used. The optical pointing model was developed over a series of observations with the following procedure: First, the telescope tracked a single source across the sky for several hours, taking several images every minute. The position of the source relative to the centre of the image was evaluated for each image and the antenna offset angle was calculated.

The antenna position was then corrected to centre the source and another image was taken. The offsets were recorded as a function of mean antenna position in azimuth and elevation and the process was repeated. The image was recorded as a FITS file with a time stamp for data analysis. Data from this observation run was used to produce the gross pointing model. Once the gross pointing model was uploaded to the telescope control system, an observation to develop the refined pointing model was employed. In this case, the telescope was given a list of optically bright sources to track. These sources were all fairly close together, allowing the telescope to track from one to the next across the sky with little risk of missing a source and getting lost. At each source, the centring process described previously was repeated. Data from this observation run was used to produce the refined pointing model. Once this was uploaded, the global pointing strategy was employed. This involved a much larger list of sources, arranged in such a way that consecutive sources were close together to avoid excessive slewing back and forth by the telescope. At each source, the camera took 15 images, repeating the centring process before moving on to the next one. Once all the sources on the list had been tracked, the data was analysed and the final global pointing model was uploaded.

### **5.1.2.3 Optical Pointing Data Analysis**

The optical pointing data analysis began by investigating the FITS images to determine which time stamps contained data which was not centred on source. This investigation was originally done by eye, but I automated it to ensure consistency and to speed up the process. The automated process identified when the telescope was pointing accurately by evaluating the peak brightness near the centre of the image and comparing it to the peak brightness of the entire image. If these values matched, then the telescope was centred on a source. This condition could fail under two circumstances: either there was no source at the centre of the image, or there was a source in the centre, but it was not the brightest source in the image. In order to account for the latter, when the two brightness values did not match, the brightness of the centre of the image was also compared with the area immediately surrounding the centre, thus eliminating the brighter off-centre source. The automated FITS analysis process produced a list of time stamps containing a bright source

near the centre of the image, and the data from this list was then analysed to produce a pointing model. Figure 5.10 (a) shows an image with a source at the centre and (b) shows the area around the centre of the image. Similarly, the images in (c) and (d) show the case where no source was present.

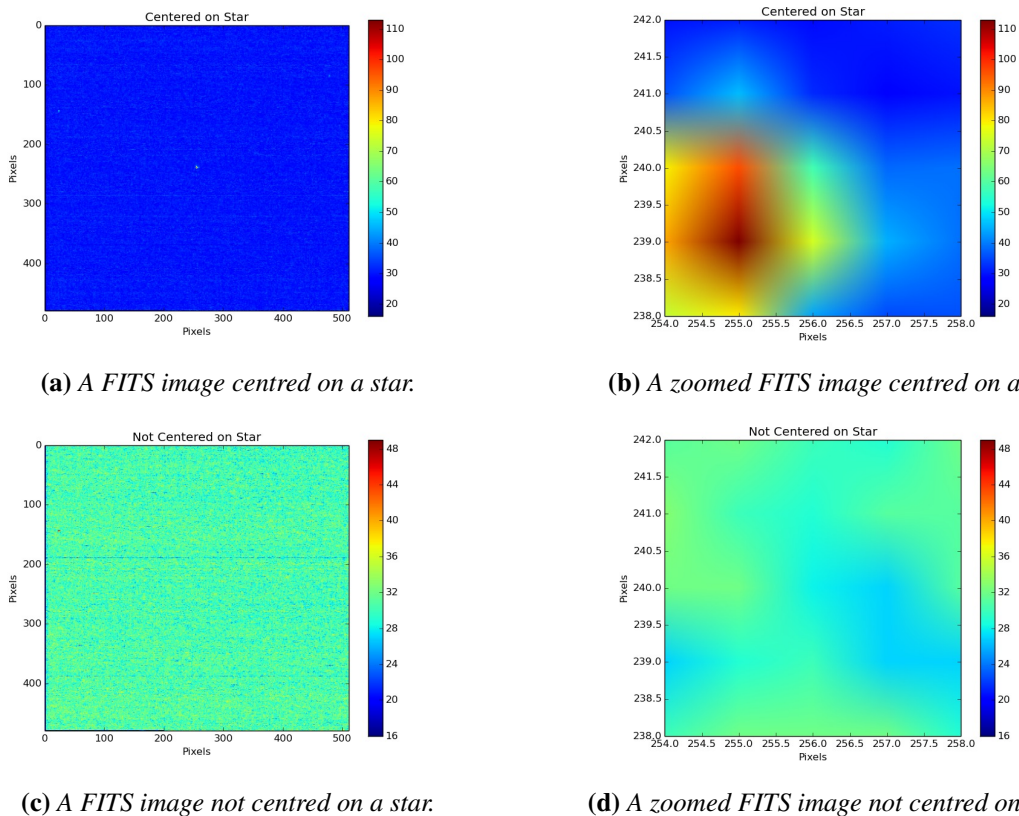


**Figure 5.10:** These are FITS images taken during optical pointing, where (a) and (b) are centred on a star, and (c) and (d) missed the source entirely.

The optical pointing model had 5 free parameters: encoder zeros, elevation tilt, collimation, azimuth tilt, and flexure. The encoder zeros parameter was applied individually to azimuth and elevation and accounted for the encoder reading at the position of zero degrees. The azimuth and elevation tilt accounted for the fact that the azimuth and elevation axes were not perfectly aligned while the collimation accounted for the lack of perfect alignment between the optical telescope and the radio telescope. The flexure parameter accounted for the fact that the primary reflector

shape changed at different positions due to its weight. Each parameter of the model was fitted to the data one by one, returning the list of pointing parameters required for the *pointing.init* file, which provided the antenna with its pointing model.

Figure 5.11 is an example of the final output of the pointing model analysis process. Of particular importance in this figure is the circle in the top right and the calculated RMS of the pointing error (denoted ‘spaceangle’ in the plot), in arcminutes. The circle shows the sky coverage, as every blue cross indicates the position of a source that was successfully tracked during the pointing run. The marks circled in red are ones where the pointing error was particularly bad, greater than 3 times the RMS of all the pointing errors. The final pointing error RMS shown in the bottom right of the figure shows the value calculated with these bad values (shown in red) and without them (shown in blue). Once the model has been fitted, the fitted parameters are then added to the *pointing.init* file and they become the online model.

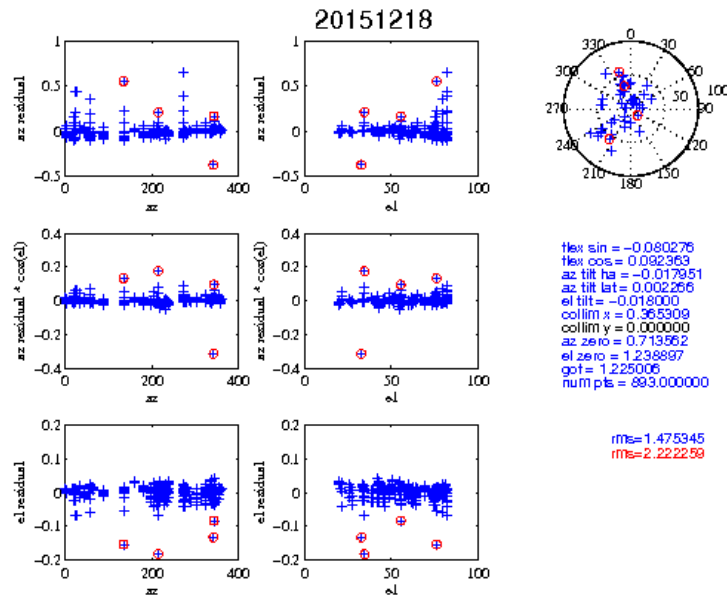


**Figure 5.11:** An example of the final output of the pointing model analysis. This plot shows the difference between the expected and actual position of each measured source in azimuth and elevation. It also shows the sky coverage, the values of the fitting parameters, and the rms of the pointing error (denoted ‘spaceangle’) in arcminutes. The values marked in red are outliers and are ignored.

### 5.1.3 Radio Pointing

Once the telescope was pointing reasonably accurately with optical pointing, we could move on to radio pointing. Once again, this was done by tracking a list of sources and comparing the measured position of each source to the expected position derived from the pointing model. For radio pointing, only very bright sources could be used because one needs a high signal to noise to find the peak. In order to know if the telescope was on source, one needed to compare measurements against off-source measurements. Therefore, the telescope performed a pointing cross, by slewing first in azimuth and then in elevation to either side of the expected source position. The offset of the source was determined by measuring the position of the peak in both azimuth and elevation, as shown in Figure 5.12, and then fitting for collimation and flexure. Once the telescope is in full survey mode, optical and radio pointing measurements will be taken once a month to ensure the continued accuracy of the pointing model.

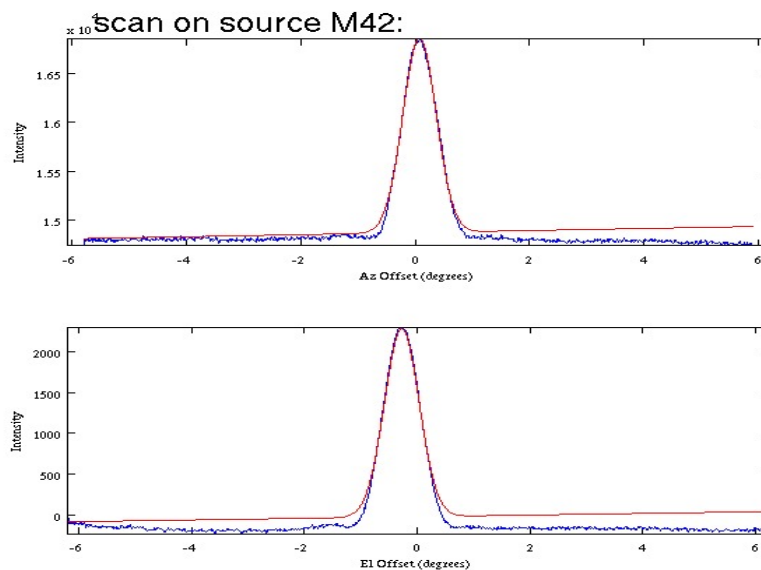


**Figure 5.12:** *Fitting the azimuth and elevation position for a radio pointing cross.*

### 5.1.4 The RFI Environment at Klerefontein

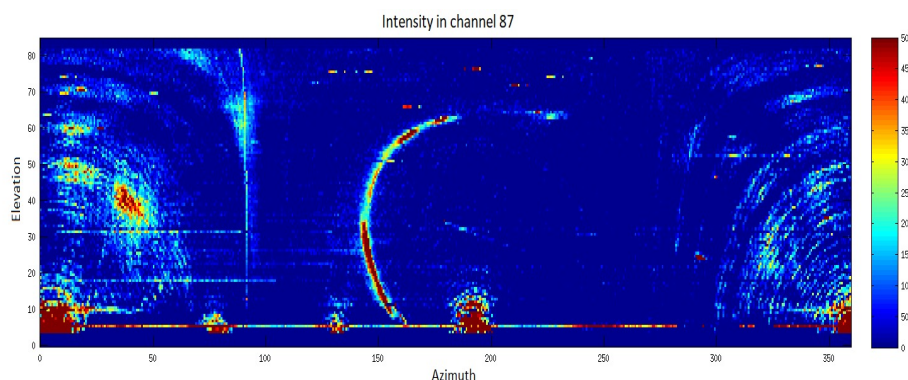
A primary reason for selecting the site at Klerefontein was that the remote location of the site would limit the prevalence of RFI. Unfortunately, there seems to still be rather a large amount of RFI on site, both on the ground and in the sky. In our efforts to conduct a thorough investigation of the RFI environment at Klerefontein, we ran multiple full sky scans that made full 360 degree sweeps in azimuth at speeds of 4 degrees per second, increasing the elevation by 0.5 degree increments after each azimuth scan. The noise diode was fired at the same point in azimuth for calibration purposes. These scans revealed four clear and persistent ground based RFI sources and several geostationary satellite sources. Table 5.2 lists the azimuth and elevation (where applicable) of the most persistent sources of RFI, as well as the channel numbers and affected bandwidth.

**Table 5.2:** *Summary of the most persistent RFI sources*

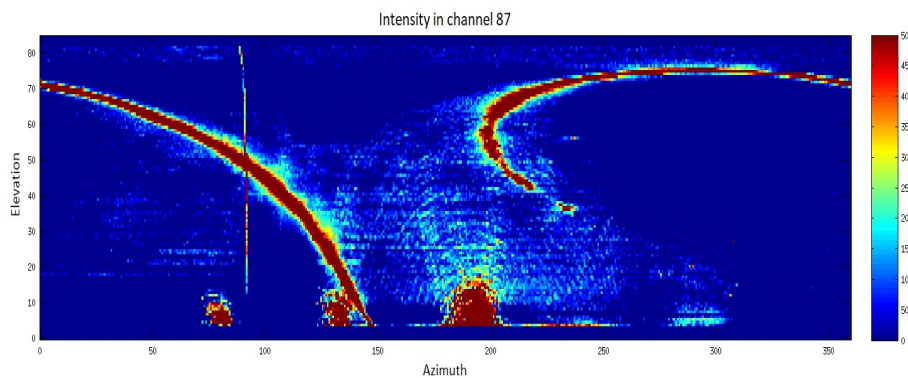
| Azimuth | Elevation | Channel No | Affected Bandwidth (MHz) |
|---------|-----------|------------|--------------------------|
| 5       | Ground    | 86,87,88   | 5164 to 5188             |
| 75      | Ground    | All        | 4555 to 5477             |
| 130     | Ground    | 86,87,88   | 5164 to 5188             |
| 290     | Ground    | 86,87,88   | 5164 to 5188             |
| 15      | 52        | 8 to 38    | 4555 to 4800             |
| 50      | 37        | 13 to 26   | 4594 to 4703             |
| 67      | 23        | 8 to 37    | 4555 to 4790             |
| 325     | 50        | 8 to 40    | 4555 to 4812             |

Figure 5.13 is an azimuth-elevation plot of a full RFI scan in channel 87. This scan was performed on 19 December 2015, and shows clear evidence of four ground based RFI sources around azimuths 5, 75, 130 and 290 degrees. During a site visit in February 2016, we realised that a wireless router had been installed at the accommodation on site. This corresponded to about 5 degrees in azimuth from the telescope, and indeed, after removing the router and running another full sky scan, we found that the source at azimuth of 5 degrees had disappeared. This is shown in Figure 5.14, an azimuth-elevation plot of the same channel as Figure 5.13, showing the same ground based RFI sources near 75, 130 and 290 degrees, but no RFI near 5 degrees. Figure

5.15 is a Google Earth satellite image of the C-BASS site with azimuth directions of the ground based RFI sources, in degrees, centred on the telescope. The three white buildings north of the telescope, on the 5 degree azimuth line are the accommodation buildings where the wireless router was found.



**Figure 5.13:** An azimuth-elevation plot of a full sky scan in channel 87, showing ground based RFI at 4 locations. The large vertical streak near azimuth 90 is the firing of the noise diode and can be ignored in this analysis.



**Figure 5.14:** An azimuth-elevation plot of a full sky scan in channel 87, showing ground based RFI at 3 locations. This data was taken after the WIFI router at the accommodation had been switched off and shows that the extremely bright source near 5 degrees in azimuth has disappeared. The large vertical streak near azimuth 90 is the firing of the noise diode and can be ignored in this analysis.



**Figure 5.15:** A Google Earth satellite image of the C-BASS site, showing the directions of the ground based RFI sources.

Figure 5.16 is an azimuth-elevation plot of a full sky scan performed on 06 February 2016, showing data from channel 31. This plot shows the four most persistent sky based RFI sources. The source near azimuth 325 degrees is particularly bright in channels 30 and 31, corresponding to a frequency range of 4727 to 7472 MHz. Given the consistency and brightness of these geostationary sources, it is possible that we could use them for beam mapping exercises.

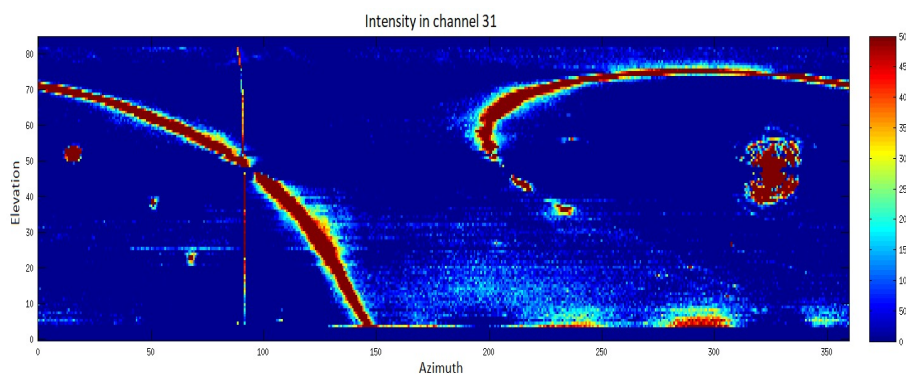


**Figure 5.16:** An azimuth-elevation plot of a full sky scan in channel 31, showing the four most persistent sky based RFI sources. The large vertical streak near azimuth 90 is the firing of the noise diode and can be ignored in this analysis.

The tremendous advantage of the southern system's digital back end, is that the spectral information allows us to be far more precise in removing RFI. Where, in the northern system, the entire bandwidth must be flagged when RFI is present, the southern system allows us to simply flag the affected channels. This is particularly relevant in the case of the ground based RFI which only affect three channels, as identified in Table 5.2. If we look at the three affected channels, as well as the channels on either side of them, shown in Figure 5.17, we can see that the channels on either side are completely unaffected by the RFI. If this were the northern system, the entire bandwidth would be lost, but with the southern system, we can simply flag the affected channels. Figure 5.18 (a) shows the average over the five channels shown in Figure 5.17, zoomed to the area of interest, while Figure 5.18 (b) shows the average over the same channels, with the affected channels flagged. This highlights the advantage of the southern system's digital back end.

Simply flagging channels affected by RFI is a crude and simple method, and will not be possible when attempting to remove broad band RFI. The plan for the southern RFI removal routine is to repeat the model fitting method used in the northern system, but applied to each individual channel, or perhaps a subset of channels averaged together. This will form a significant part of my post-doctoral work.

### **5.1.5 Investigating RFI Using the C-BASS Signal Band**

The signal band refers to the range in frequency space corresponding to signals of interest on the sky. The C-BASS telescopes scan at reasonably high speeds, around 4 degrees per second. With a beam size of order 0.7 degrees, this translates to a scan rate of 6 beams per second, and a 6 Hz sky signal. This means that the signal power rate of change for a true sky source is limited to 6 Hz, with a lower limit of 0.01 Hz. These limits are not exact, as the beam is not perfectly defined, but most of the sky signal is expected to drop off beyond these limits.

We can take advantage of this by binning the data up into 100 ms bins and investigating how much the signal changes in that time. A true sky signal would not change much, but a quick

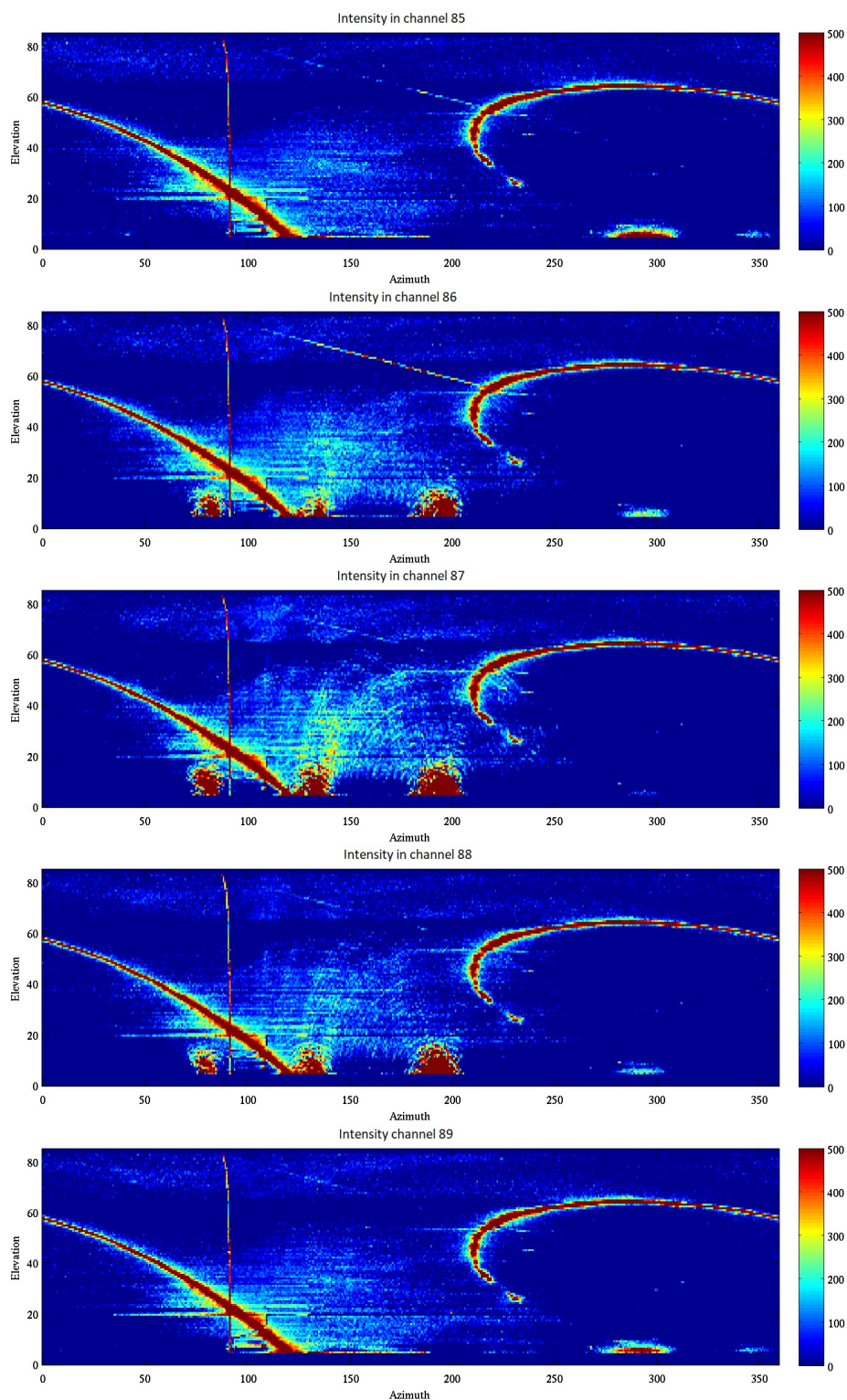
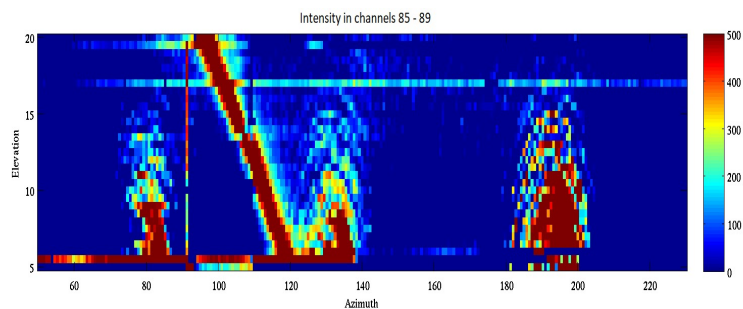
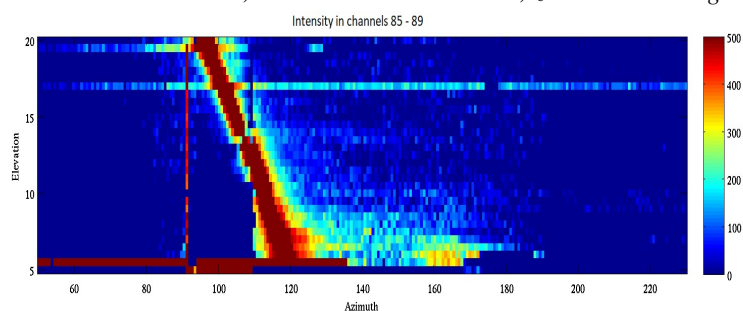


**Figure 5.17:** Three channels affected by ground based RFI, bordered by unaffected channels. The large vertical streak near azimuth 90 is the firing of the noise diode and can be ignored in this analysis.



(a) Average over channels 85 to 89, without channel excision, zoomed to the region of interest.



(b) Average over channels 85 to 89, with channel excision, zoomed to the region of interest.

**Figure 5.18:** Average over channels 85 to 89, with and without channel excision. The large vertical streak near azimuth 90 is the firing of the noise diode and can be ignored in this analysis.

burst of RFI would be identified by a large RMS relative to the typical RMS value of the other bins. Figure 5.19 shows RFI events detected using this method. In this figure, the events have been plotted across all channels from both ROACHes, with each separate RFI event represented by a single colour on the plot. The plot highlights that we have both broad- and narrowband RFI at Klerefontein. I plan to expand on this method and employ it in the data reduction pipeline for both the northern and southern data.

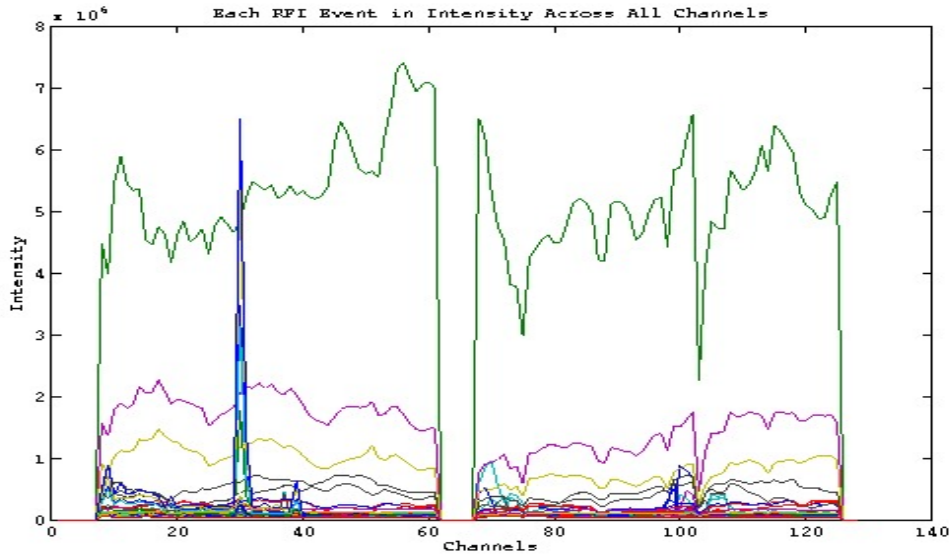


**Figure 5.19:** This plot shows the RFI events detected across all channels in southern data. Each colour represents an individual 100 ms bin of data, showing the intensity, measured in back end units, across every channel in the band. Some channels on either end of each ROACH’s spectrum are intentionally blanked in an attempt to prevent the detection of out-of-band signal. This plot shows that we have both broad- and narrowband RFI.

## 5.2 Summary and Conclusions

In this chapter I have discussed my work in commissioning the southern system. I have described the photogrammetry technique employed to align the panels of the primary reflector, and the method used to position the secondary mirror. I have provided details on the remote optical pointing system and described the methods used to calibrate both the optical and radio pointing of the telescope. Finally, I have provided an overview of the RFI environment at Klerefontein and discussed how the spectral resolution of the southern system can be exploited in identifying RFI.

The southern system is on the verge of beginning survey operations, and this is very exciting as we believe the maps from this instrument will have a tremendous impact on the CMB community, given that so many CMB experiments observe the southern sky. The conclusion of the

southern survey will also enable us to deliver full sky maps of Galactic foreground radiation at 5 GHz. Figure 5.20 is an example of what we hope to produce. This map is a very simple and uncalibrated mix of northern and southern data and serves simply as a proof of concept and an exciting foretaste of what is to come!

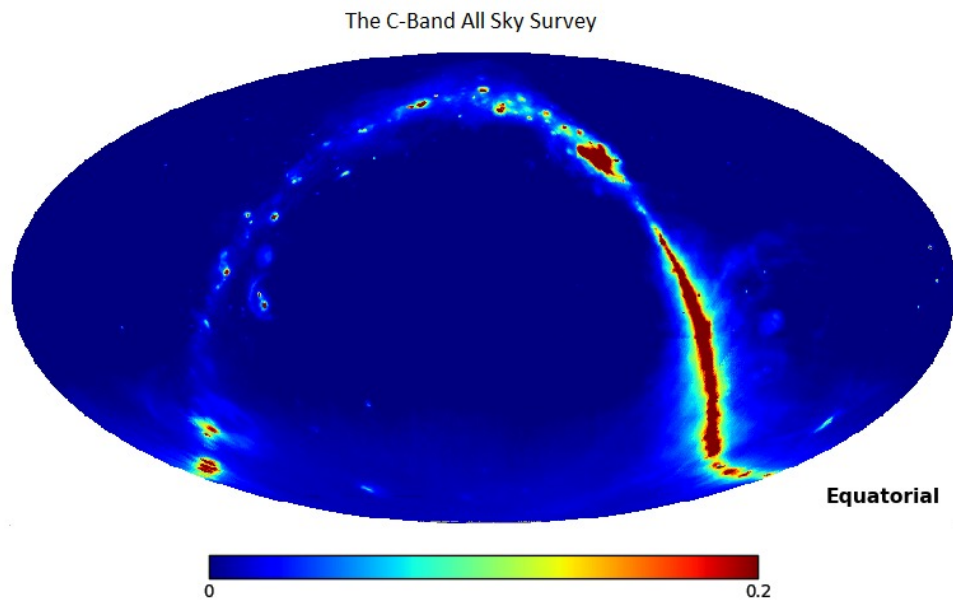


**Figure 5.20:** *An uncalibrated, naive sky map made from a combination of northern and southern data, which serves as a proof of concept for the C-Band All Sky Survey. This image was produced by collaboration member Angela Taylor and is presented with her permission.*

# Bibliography

Ade, P. A. R., Akiba, Y., Anthony, A. E., Arnold, K., Atlas, M., Barron, D., Boettger, D., Borrill, J., Chapman, S., Chinone, Y., Dobbs, M., Elleflot, T., Errard, J., Fabbian, G., Feng, C., Flanagan, D., Gilbert, A., Grainger, W., Halverson, N. W., Hasegawa, M., Hattori, K., Hazumi, M., Holzappel, W. L., Hori, Y., Howard, J., Hyland, P., Inoue, Y., Jaehnig, G. C., Jaffe, A., Keating, B., Kermish, Z., Keskitalo, R., Kisner, T., Le Jeune, M., Lee, A. T., Linder, E., Leitch, E. M., Lungu, M., Matsuda, F., Matsumura, T., Meng, X., Miller, N. J., Morii, H., Moyerman, S., Myers, M. J., Navaroli, M., Nishino, H., Paar, H., Peloton, J., Quealy, E., Rebeiz, G., Reichardt, C. L., Richards, P. L., Ross, C., Schanning, I., Schenck, D. E., Sherwin, B., Shimizu, A., Shimmin, C., Shimon, M., Siritanasak, P., Smecher, G., Spieler, H., Stebor, N., Steinbach, B., Stompor, R., Suzuki, A., Takakura, S., Tomaru, T., Wilson, B., Yadav, A., Zahn, O., and Polarbear Collaboration (2014). Measurement of the Cosmic Microwave Background Polarization Lensing Power Spectrum with the POLARBEAR Experiment. *Physical Review Letters*, 113(2):021301.

Alpher, R. A. and Herman, R. (1948). Evolution of the Universe. *Nature.*, 162:774–775.

Barkats, D., Bischoff, C., Farese, P., Fitzpatrick, L., Gaier, T., Gundersen, J. O., Hedman, M. M., Hyatt, L., McMahon, J. J., Samtleben, D., Staggs, S. T., Vanderlinde, K., and Winstein, B. (2005). First Measurements of the Polarization of the Cosmic Microwave Background Radiation at Small Angular Scales from CAPMAP. *Astrophys. J. Lett.*, 619:L127–L130.

Battye, R. A., Browne, I. W. A., Peel, M. W., Jackson, N. J., and Dickinson, C. (2011). Statistical properties of polarized radio sources at high frequency and their impact on cosmic microwave

background polarization measurements. *Mon. Not. R. Astron. Soc.*, 413:132–148.

Baumann, D., Jackson, M. G., Adshead, P., Amblard, A., Ashoorioon, A., Bartolo, N., Bean, R., Beltrán, M., de Bernardis, F., Bird, S., Chen, X., Chung, D. J. H., Colombo, L., Cooray, A., Creminelli, P., Dodelson, S., Dunkley, J., Dvorkin, C., Easther, R., Finelli, F., Flauger, R., Hertzberg, M. P., Jones-Smith, K., Kachru, S., Kadota, K., Khoury, J., Kinney, W. H., Komatsu, E., Krauss, L. M., Lesgourgues, J., Liddle, A., Liguori, M., Lim, E., Linde, A., Matarrese, S., Mathur, H., McAllister, L., Melchiorri, A., Nicolis, A., Pagano, L., Peiris, H. V., Peloso, M., Pogosian, L., Pierpaoli, E., Riotto, A., Seljak, U., Senatore, L., Shandera, S., Silverstein, E., Smith, T., Vaudrevange, P., Verde, L., Wandelt, B., Wands, D., Watson, S., Wyman, M., Yadav, A., Valkenburg, W., and Zaldarriaga, M. (2009). Probing Inflation with CMB Polarization. In Dodelson, S., Baumann, D., Cooray, A., Dunkley, J., Fraisse, A., Jackson, M. G., Kogut, A., Krauss, L., Zaldarriaga, M., and Smith, K., editors, *American Institute of Physics Conference Series*, volume 1141 of *American Institute of Physics Conference Series*, pages 10–120.

Bennett, C. L., Hill, R. S., Hinshaw, G., Nolta, M. R., Odegard, N., Page, L., Spergel, D. N., Weiland, J. L., Wright, E. L., Halpern, M., Jarosik, N., Kogut, A., Limon, M., Meyer, S. S., Tucker, G. S., and Wollack, E. (2003). First-Year Wilkinson Microwave Anisotropy Probe (WMAP) Observations: Foreground Emission. *Astrophys. J. Supp.*, 148:97–117.

Bennett, C. L., Larson, D., Weiland, J. L., Jarosik, N., Hinshaw, G., Odegard, N., Smith, K. M., Hill, R. S., Gold, B., Halpern, M., Komatsu, E., Nolta, M. R., Page, L., Spergel, D. N., Wollack, E., Dunkley, J., Kogut, A., Limon, M., Meyer, S. S., Tucker, G. S., and Wright, E. L. (2013). Nine-year Wilkinson Microwave Anisotropy Probe (WMAP) Observations: Final Maps and Results. *Astrophys. J. Supp.*, 208:20.

BICEP2 Collaboration, Ade, P. A. R., Aikin, R. W., Barkats, D., Benton, S. J., Bischoff, C. A., Bock, J. J., Brevik, J. A., Buder, I., Bullock, E., Dowell, C. D., Duband, L., Filippini, J. P., Fliescher, S., Golwala, S. R., Halpern, M., Hasselfield, M., Hildebrandt, S. R., Hilton, G. C., Hristov, V. V., Irwin, K. D., Karkare, K. S., Kaufman, J. P., Keating, B. G., Kernasovskiy,

- S. A., Kovac, J. M., Kuo, C. L., Leitch, E. M., Lueker, M., Mason, P., Netterfield, C. B., Nguyen, H. T., O'Brient, R., Ogburn, R. W., Orlando, A., Pryke, C., Reintsema, C. D., Richter, S., Schwarz, R., Sheehy, C. D., Staniszewski, Z. K., Sudiwala, R. V., Teply, G. P., Tolan, J. E., Turner, A. D., Vieregg, A. G., Wong, C. L., and Yoon, K. W. (2014). Detection of B-Mode Polarization at Degree Angular Scales by BICEP2. *Physical Review Letters*, 112(24):241101.
- BICEP2 Collaboration, Keck Array Collaboration, Ade, P. A. R., Ahmed, Z., Aikin, R. W., Alexander, K. D., Barkats, D., Benton, S. J., Bischoff, C. A., Bock, J. J., Bowens-Rubin, R., Brevik, J. A., Buder, I., Bullock, E., Buza, V., Connors, J., Crill, B. P., Duband, L., Dvorkin, C., Filippini, J. P., Fliescher, S., Grayson, J., Halpern, M., Harrison, S., Hilton, G. C., Hui, H., Irwin, K. D., Karkare, K. S., Karpel, E., Kaufman, J. P., Keating, B. G., Kefeli, S., Kernasovskiy, S. A., Kovac, J. M., Kuo, C. L., Leitch, E. M., Lueker, M., Megerian, K. G., Netterfield, C. B., Nguyen, H. T., O'Brient, R., Ogburn, R. W., Orlando, A., Pryke, C., Richter, S., Schwarz, R., Sheehy, C. D., Staniszewski, Z. K., Steinbach, B., Sudiwala, R. V., Teply, G. P., Thompson, K. L., Tolan, J. E., Tucker, C., Turner, A. D., Vieregg, A. G., Weber, A. C., Wiebe, D. V., Willmert, J., Wong, C. L., Wu, W. L. K., and Yoon, K. W. (2016). Improved Constraints on Cosmology and Foregrounds from BICEP2 and Keck Array Cosmic Microwave Background Data with Inclusion of 95 GHz Band. *Physical Review Letters*, 116(3):031302.
- Blumenthal, G. R., Faber, S. M., Primack, J. R., and Rees, M. J. (1984). Formation of galaxies and large-scale structure with cold dark matter. *Nature.*, 311:517–525.
- Bond, J. R. and Efstathiou, G. (1984). Cosmic background radiation anisotropies in universes dominated by nonbaryonic dark matter. *Astrophys. J. Lett.*, 285:L45–L48.
- Bond, J. R. and Efstathiou, G. (1987). The statistics of cosmic background radiation fluctuations. *Mon. Not. R. Astron. Soc.*, 226:655–687.
- Burbidge, G. R. (1956). On Synchrotron Radiation from Messier 87. *Astrophys. J.*, 124:416.

- Burigana, C., Malaspina, M., Mandolesi, N., Danse, L., Maino, D., Bersanelli, M., and Maltoni, M. (1999). A preliminary study on destriping techniques of PLANCK/LFI measurements versus observational strategy. *ArXiv Astrophysics e-prints*.
- Carretti, E. (2010). Galactic Foregrounds and CMB Polarization. In Kothes, R., Landecker, T. L., and Willis, A. G., editors, *The Dynamic Interstellar Medium: A Celebration of the Canadian Galactic Plane Survey*, volume 438 of *Astronomical Society of the Pacific Conference Series*, page 276.
- Copley, C. (2013). The C-Band All Sky Survey. PhD Thesis.
- Davies, R. D., Dickinson, C., Banday, A. J., Jaffe, T. R., Górski, K. M., and Davis, R. J. (2006). A determination of the spectra of Galactic components observed by the Wilkinson Microwave Anisotropy Probe. *Mon. Not. R. Astron. Soc.*, 370:1125–1139.
- Davies, R. D., Watson, R. A., and Gutierrez, C. M. (1996). Galactic synchrotron emission at high frequencies. *Mon. Not. R. Astron. Soc.*, 278:925–939.
- de Bernardis, P., Ade, P. A. R., Bock, J. J., Bond, J. R., Borrill, J., Boscaleri, A., Coble, K., Crill, B. P., De Gasperis, G., Farese, P. C., Ferreira, P. G., Ganga, K., Giacometti, M., Hivon, E., Hristov, V. V., Iacoangeli, A., Jaffe, A. H., Lange, A. E., Martinis, L., Masi, S., Mason, P. V., Mouskops, P. D., Melchiorri, A., Miglio, L., Montroy, T., Netterfield, C. B., Pascale, E., Piacentini, F., Pogosyan, D., Prunet, S., Rao, S., Romeo, G., Ruhl, J. E., Scaramuzzi, F., Sforna, D., and Vittorio, N. (2000). A flat Universe from high-resolution maps of the cosmic microwave background radiation. *Nature.*, 404:955–959.
- de Gasperis, G., Balbi, A., Cabella, P., Natoli, P., and Vittorio, N. (2005). ROMA: A map-making algorithm for polarised CMB data sets. *Astron. Astrophys.*, 436:1159–1165.
- de Oliveira-Costa, A., Tegmark, M., Davies, R. D., Gutiérrez, C. M., Lasenby, A. N., Rebolo, R., and Watson, R. A. (2004). The Quest for Microwave Foreground X. *Astrophys. J. Lett.*, 606:L89–L92.

- Delabrouille, J. (1998). Analysis of the accuracy of a destripping method for future cosmic microwave background mapping with the PLANCK SURVEYOR satellite. *Astron. Astrophys. Supp.*, 127:555–567.
- Dicke, R. H. (1946). The measurement of thermal radiation at microwave frequencies. *Review of Scientific Instruments*, 17:268.
- Dicke, R. H., Peebles, P. J. E., Roll, P. G., and Wilkinson, D. T. (1965). Cosmic Black-Body Radiation. *Astrophys. J.*, 142:414–419.
- Dickinson, C., Davies, R. D., and Davis, R. J. (2003). Towards a free-free template for CMB foregrounds. *Mon. Not. R. Astron. Soc.*, 341:369–384.
- Dickinson, C., Eriksen, H. K., Banday, A. J., Jewell, J. B., Górski, K. M., Huey, G., Lawrence, C. R., O’Dwyer, I. J., and Wandelt, B. D. (2009). Bayesian Component Separation and Cosmic Microwave Background Estimation for the Five-Year WMAP Temperature Data. *Astrophys. J.*, 705:1607–1623.
- Dickinson, C., Peel, M., and Vidal, M. (2011). New constraints on the polarization of anomalous microwave emission in nearby molecular clouds. *Mon. Not. R. Astron. Soc.*, 418:L35–L39.
- Doré, O., Teyssier, R., Bouchet, F. R., Vibert, D., and Prunet, S. (2001). MAPCUMBA: A fast iterative multi-grid map-making algorithm for CMB experiments. *Astron. Astrophys.*, 374:358–370.
- Draine, B. T. (2011). Physics of the Interstellar and Intergalactic Medium. In *Physics of the Interstellar and Intergalactic Medium by Bruce T. Draine*. Princeton University Press, 2011. ISBN: 978-0-691-12214-4.
- Draine, B. T. and Lazarian, A. (1998a). Diffuse Galactic Emission from Spinning Dust Grains. *Astrophys. J. Lett.*, 494:L19–L22.
- Draine, B. T. and Lazarian, A. (1998b). Electric Dipole Radiation from Spinning Dust Grains. *Astrophys. J.*, 508:157–179.

- Draine, B. T. and Lazarian, A. (1999). Magnetic Dipole Microwave Emission from Dust Grains. *Astrophys. J.*, 512:740–754.
- Dunkley, J., Amblard, A., Baccigalupi, C., Betoule, M., Chuss, D., Cooray, A., Delabrouille, J., Dickinson, C., Dobler, G., Dotson, J., Eriksen, H. K., Finkbeiner, D., Fixsen, D., Fosalba, P., Fraisse, A., Hirata, C., Kogut, A., Kristiansen, J., Lawrence, C., Magalhaães, A. M., Miville-Deschenes, M. A., Meyer, S., Miller, A., Naess, S. K., Page, L., Peiris, H. V., Phillips, N., Pierpaoli, E., Rocha, G., Vaillancourt, J. E., and Verde, L. (2009). Prospects for polarized foreground removal. In Dodelson, S., Baumann, D., Cooray, A., Dunkley, J., Fraisse, A., Jackson, M. G., Kogut, A., Krauss, L., Zaldarriaga, M., and Smith, K., editors, *American Institute of Physics Conference Series*, volume 1141 of *American Institute of Physics Conference Series*, pages 222–264.
- Dünner, R., Hasselfield, M., Marriage, T. A., Sievers, J., Acquaviva, V., Addison, G. E., Ade, P. A. R., Aguirre, P., Amiri, M., Appel, J. W., Barrientos, L. F., Battistelli, E. S., Bond, J. R., Brown, B., Burger, B., Calabrese, E., Chervenak, J., Das, S., Devlin, M. J., Dicker, S. R., Bertrand Doriese, W., Dunkley, J., Essinger-Hileman, T., Fisher, R. P., Gralla, M. B., Fowler, J. W., Hajian, A., Halpern, M., Hernández-Monteagudo, C., Hilton, G. C., Hilton, M., Hincks, A. D., Hlozek, R., Huffenberger, K. M., Hughes, D. H., Hughes, J. P., Infante, L., Irwin, K. D., Baptiste Juin, J., Kaul, M., Klein, J., Kosowsky, A., Lau, J. M., Limon, M., Lin, Y.-T., Louis, T., Lupton, R. H., Marsden, D., Martocci, K., Mausekopf, P., Menanteau, F., Moodley, K., Moseley, H., Netterfield, C. B., Niemack, M. D., Nolta, M. R., Page, L. A., Parker, L., Partridge, B., Quintana, H., Reid, B., Sehgal, N., Sherwin, B. D., Spergel, D. N., Staggs, S. T., Swetz, D. S., Switzer, E. R., Thornton, R., Trac, H., Tucker, C., Warne, R., Wilson, G., Wollack, E., and Zhao, Y. (2013). The Atacama Cosmology Telescope: Data Characterization and Mapmaking. *Astrophys. J.*, 762:10.
- Efstathiou, G., Sutherland, W. J., and Maddox, S. J. (1990). The cosmological constant and cold dark matter. *Nature.*, 348:705–707.

- Einstein, A. (1916). Die Grundlage der allgemeinen Relativitätstheorie. *Annalen der Physik*, 354:769–822.
- Elder, F. R., Gurewitsch, A. M., Langmuir, R. V., and Pollock, H. C. (1947). Radiation from electrons in a synchrotron. *Phys. Rev.*, 71:829–830.
- Finkbeiner, D. P. (2003). A Full-Sky H $\alpha$  Template for Microwave Foreground Prediction. *Astrophys. J. Supp.*, 146:407–415.
- Flauger, R., Hill, J. C., and Spergel, D. N. (2014). Toward an understanding of foreground emission in the BICEP2 region. *Journal of Cosmology and Astroparticle Physics.*, 8:039.
- Fowler, J. W., Acquaviva, V., Ade, P. A. R., Aguirre, P., Amiri, M., Appel, J. W., Barrientos, L. F., Battistelli, E. S., Bond, J. R., Brown, B., Burger, B., Chervenak, J., Das, S., Devlin, M. J., Dicker, S. R., Doriese, W. B., Dunkley, J., Dünner, R., Essinger-Hileman, T., Fisher, R. P., Hajian, A., Halpern, M., Hasselfield, M., Hernández-Montenegro, C., Hilton, G. C., Hilton, M., Hincks, A. D., Hlozek, R., Huppenberger, K. M., Hughes, D. H., Hughes, J. P., Infante, L., Irwin, K. D., Jimenez, R., Juin, J. B., Kaul, M., Klein, J., Kosowsky, A., Lau, J. M., Limon, M., Lin, Y.-T., Lupton, R. H., Marriage, T. A., Marsden, D., Martocci, K., Mauskopf, P., Menanteau, F., Moodley, K., Moseley, H., Netterfield, C. B., Niemack, M. D., Nolte, M. R., Page, L. A., Parker, L., Partridge, B., Quintana, H., Reid, B., Sehgal, N., Sievers, J., Spergel, D. N., Staggs, S. T., Swetz, D. S., Switzer, E. R., Thornton, R., Trac, H., Tucker, C., Verde, L., Warne, R., Wilson, G., Wollack, E., and Zhao, Y. (2010). The Atacama Cosmology Telescope: A Measurement of the 600–8000 Cosmic Microwave Background Power Spectrum at 148 GHz. *Astrophys. J.*, 722:1148–1161.
- Friedmann, A. (1922). Über die Krümmung des Raumes. *Zeitschrift für Physik*, 10:377–386.
- Fuskeland, U., Wehus, I. K., Eriksen, H. K., and Næss, S. K. (2014). Spatial Variations in the Spectral Index of Polarized Synchrotron Emission in the 9 yr WMAP Sky Maps. *Astrophys. J.*, 790:104.

- Génova-Santos, R., Rubiño-Martín, J. A., Rebolo, R., Aguiar, M., Gómez-Reñasco, F., Gutiérrez, C., Hoyland, R. J., López-Caraballo, C., Peláez-Santos, A. E., Pérez-de-Taoro, M. R., Poidevin, F., Sánchez de la Rosa, V., Tramonte, D., Vega-Moreno, A., Viera-Curbelo, T., Vignasa, R., Martínez-González, E., Barreiro, R. B., Casaponsa, B., Casas, F. J., Diego, J. M., Fernández-Cobos, R., Herranz, D., López-Caniego, M., Ortiz, D., Vielva, P., Artal, E., Aja, B., Cagigas, J., Cano, J. L., de la Fuente, L., Mediavilla, A., Terán, J. V., Villa, E., Piccirillo, L., Davies, R., Davis, R. J., Dickinson, C., Grainge, K., Harper, S., Maffei, B., McCulloch, M., Melhuish, S., Pisano, G., Watson, R. A., Lasenby, A., Ashdown, M., Hobson, M., Perrott, Y., Razavi-Ghods, N., Saunders, R., Titterington, D., and Scott, P. (2015a). The QUIJOTE experiment: project overview and first results. In Cenarro, A. J., Figueras, F., Hernández-Monteagudo, C., Trujillo Bueno, J., and Valdivielso, L., editors, *Highlights of Spanish Astrophysics VIII*, pages 207–212.
- Génova-Santos, R., Rubiño-Martín, J. A., Rebolo, R., Peláez-Santos, A., López-Caraballo, C. H., Harper, S., Watson, R. A., Ashdown, M., Barreiro, R. B., Casaponsa, B., Dickinson, C., Diego, J. M., Fernández-Cobos, R., Grainge, K. J. B., Gutiérrez, C. M., Herranz, D., Hoyland, R., Lasenby, A., López-Caniego, M., Martínez-González, E., McCulloch, M., Melhuish, S., Piccirillo, L., Perrott, Y. C., Poidevin, F., Razavi-Ghods, N., Scott, P. F., Titterington, D., Tramonte, D., Vielva, P., and Vignaga, R. (2015b). QUIJOTE scientific results - I. Measurements of the intensity and polarisation of the anomalous microwave emission in the Perseus molecular complex. *Mon. Not. R. Astron. Soc.*, 452:4169–4182.
- Ghosh, T., Banday, A. J., Jaffe, T., Dickinson, C., Davies, R., Davis, R., and Gorski, K. (2012). Foreground analysis using cross-correlations of external templates on the 7-year Wilkinson Microwave Anisotropy Probe data. *Mon. Not. R. Astron. Soc.*, 422:3617–3642.
- Gold, B., Odegard, N., Weiland, J. L., Hill, R. S., Kogut, A., Bennett, C. L., Hinshaw, G., Chen, X., Dunkley, J., Halpern, M., Jarosik, N., Komatsu, E., Larson, D., Limon, M., Meyer, S. S., Nolta, M. R., Page, L., Smith, K. M., Spergel, D. N., Tucker, G. S., Wollack, E., and Wright,

- E. L. (2011). Seven-year Wilkinson Microwave Anisotropy Probe (WMAP) Observations: Galactic Foreground Emission. *Astrophys. J. Supp.*, 192:15.
- Górski, K. M., Hivon, E., Banday, A. J., Wandelt, B. D., Hansen, F. K., Reinecke, M., and Bartelmann, M. (2005). HEALPix: A Framework for High-Resolution Discretization and Fast Analysis of Data Distributed on the Sphere. *Astrophys. J.*, 622:759–771.
- Gorski, K. M., Wandelt, B. D., Hansen, F. K., Hivon, E., and Banday, A. J. (1999). The HEALPix Primer. *ArXiv Astrophysics e-prints*.
- Guth, A. H. (1981). Inflationary universe: A possible solution to the horizon and flatness problems. *Physical Review D.*, 23:347–356.
- Hanany, S., Ade, P., Balbi, A., Bock, J., Borrill, J., Boscaleri, A., de Bernardis, P., Ferreira, P. G., Hristov, V. V., Jaffe, A. H., Lange, A. E., Lee, A. T., Mauskopf, P. D., Netterfield, C. B., Oh, S., Pascale, E., Rabii, B., Richards, P. L., Smoot, G. F., Stompor, R., Winant, C. D., and Wu, J. H. P. (2000). MAXIMA-1: A Measurement of the Cosmic Microwave Background Anisotropy on Angular Scales of  $10' - 5\text{deg}$ . *Astrophys. J. Lett.*, 545 : L5 – –L9.
- Hanson, D., Hoover, S., Crites, A., Ade, P. A. R., Aird, K. A., Austermann, J. E., Beall, J. A., Bender, A. N., Benson, B. A., Bleem, L. E., Bock, J. J., Carlstrom, J. E., Chang, C. L., Chiang, H. C., Cho, H.-M., Conley, A., Crawford, T. M., de Haan, T., Dobbs, M. A., Everett, W., Gallicchio, J., Gao, J., George, E. M., Halverson, N. W., Harrington, N., Henning, J. W., Hilton, G. C., Holder, G. P., Holzzapfel, W. L., Hrubes, J. D., Huang, N., Hubmayr, J., Irwin, K. D., Keisler, R., Knox, L., Lee, A. T., Leitch, E., Li, D., Liang, C., Luong-Van, D., Marsden, G., McMahon, J. J., Mehl, J., Meyer, S. S., Mocuano, L., Montroy, T. E., Natoli, T., Nibarger, J. P., Novosad, V., Padin, S., Pryke, C., Reichardt, C. L., Ruhl, J. E., Saliwanchik, B. R., Sayre, J. T., Schaffer, K. K., Schulz, B., Smecher, G., Stark, A. A., Story, K. T., Tucker, C., Vanderlinde, K., Vieira, J. D., Viero, M. P., Wang, G., Yefremenko, V., Zahn, O., and Zemcov, M. (2013). Detection of B-Mode Polarization in the Cosmic Microwave Background with Data from the South Pole Telescope. *Physical Review Letters*, 111(14):141301.

- Harrington, K., Marriage, T., Ali, A., Appel, J. W., Bennett, C. L., Boone, F., Brewer, M., Chan, M., Chuss, D. T., Colazo, F., Dahal, S., Denis, K., Dünner, R., Eimer, J., Essinger-Hileman, T., Fluxa, P., Halpern, M., Hilton, G., Hinshaw, G. F., Hubmayr, J., Iuliano, J., Karakla, J., McMahan, J., Miller, N. T., Moseley, S. H., Palma, G., Parker, L., Petroff, M., Pradenas, B., Rostem, K., Sagliocca, M., Valle, D., Watts, D., Wollack, E., Xu, Z., and Zeng, L. (2016). The Cosmology Large Angular Scale Surveyor. In *Millimeter, Submillimeter, and Far-Infrared Detectors and Instrumentation for Astronomy VIII*, volume 9914 of , page 99141K.
- Haslam, C. G. T., Klein, U., Salter, C. J., Stoffel, H., Wilson, W. E., Cleary, M. N., Cooke, D. J., and Thomasson, P. (1981). A 408 MHz all-sky continuum survey. I - Observations at southern declinations and for the North Polar region. *Astron. Astrophys.*, 100:209–219.
- Hinshaw, G., Barnes, C., Bennett, C. L., Greason, M. R., Halpern, M., Hill, R. S., Jarosik, N., Kogut, A., Limon, M., Meyer, S. S., Odegard, N., Page, L., Spergel, D. N., Tucker, G. S., Weiland, J. L., Wollack, E., and Wright, E. L. (2003). First-Year Wilkinson Microwave Anisotropy Probe (WMAP) Observations: Data Processing Methods and Systematic Error Limits. *Astrophys. J. Supp.*, 148:63–95.
- Hinshaw, G., Larson, D., Komatsu, E., Spergel, D. N., Bennett, C. L., Dunkley, J., Nolta, M. R., Halpern, M., Hill, R. S., Odegard, N., Page, L., Smith, K. M., Weiland, J. L., Gold, B., Jarosik, N., Kogut, A., Limon, M., Meyer, S. S., Tucker, G. S., Wollack, E., and Wright, E. L. (2013). Nine-year Wilkinson Microwave Anisotropy Probe (WMAP) Observations: Cosmological Parameter Results. *Astrophys. J. Supp.*, 208:19.
- Hivon, E., Górski, K. M., Netterfield, C. B., Crill, B. P., Prunet, S., and Hansen, F. (2002). MASTER of the Cosmic Microwave Background Anisotropy Power Spectrum: A Fast Method for Statistical Analysis of Large and Complex Cosmic Microwave Background Data Sets. *Astrophys. J.*, 567:2–17.
- Hoang, T., Lazarian, A., and Martin, P. G. (2013). Constraint on the Polarization of Electric Dipole Emission from Spinning Dust. *Astrophys. J.*, 779:152.

- Holler, C. M., Taylor, A. C., Jones, M. E., King, O. G., Muchovej, S. J. C., Stevenson, M. A., Wylde, R. J., Copley, C. J., Davis, R. J., Pearson, T. J., and Readhead, A. C. S. (2013). A Circularly Symmetric Antenna Design With High Polarization Purity and Low Spillover. *IEEE Transactions on Antennas and Propagation*, 61:117–124.
- Holtzman, J. A. (1989). Microwave background anisotropies and large-scale structure in universes with cold dark matter, baryons, radiation, and massive and massless neutrinos. *Astrophys. J. Supp.*, 71:1–24.
- Hu, W. and Dodelson, S. (2002). Cosmic Microwave Background Anisotropies. *Annu. Rev. Astron. Astrophys.*, 40:171–216.
- Hu, W., Sugiyama, N., and Silk, J. (1997). The physics of microwave background anisotropies. *Nature.*, 386:37–43.
- Hu, W. and White, M. (1996). Acoustic Signatures in the Cosmic Microwave Background. *Astrophys. J.*, 471:30.
- Hu, W. and White, M. (1997). A CMB polarization primer. *New Astron.*, 2:323–344.
- Hubble, E. (1929). A Relation between Distance and Radial Velocity among Extra-Galactic Nebulae. *Proceedings of the National Academy of Science*, 15:168–173.
- Huterer, D. and Turner, M. S. (2001). Probing dark energy: Methods and strategies. *Physical Review D.*, 64(12):123527.
- Imbriale, W. A. and Abraham, R. (2004). Radio Frequency Optics Design of the Deep Space Network Large Array 6-Meter Breadboard Antenna. *Interplanetary Network Progress Report*, 157:1–8.
- Kamionkowski, M., Kosowsky, A., and Stebbins, A. (1997). A Probe of Primordial Gravity Waves and Vorticity. *Physical Review Letters*, 78:2058–2061.

- Keihänen, E., Keskitalo, R., Kurki-Suonio, H., Poutanen, T., and Sirviö, A.-S. (2010). Making cosmic microwave background temperature and polarization maps with MADAM. *Astron. Astrophys.*, 510:A57.
- Keihänen, E., Kurki-Suonio, H., and Poutanen, T. (2005). MADAM- a map-making method for CMB experiments. *Mon. Not. R. Astron. Soc.*, 360:390–400.
- Keihänen, E., Kurki-Suonio, H., Poutanen, T., Maino, D., and Burigana, C. (2004). A maximum likelihood approach to the destripping technique. *Astron. Astrophys.*, 428:287–298.
- King, O. G., Copley, C., Davies, R., Davis, R., Dickinson, C., Hafez, Y. A., Holler, C., John, J. J., Jonas, J. L., Jones, M. E., Leahy, J. P., Muchovej, S. J. C., Pearson, T. J., Readhead, A. C. S., Stevenson, M. A., and Taylor, A. C. (2010). The C-Band All-Sky Survey: instrument design, status, and first-look data. In *Millimeter, Submillimeter, and Far-Infrared Detectors and Instrumentation for Astronomy V*, volume 7741 of , page 77411I.
- King, O. G., Jones, M. E., Blackhurst, E. J., Copley, C., Davis, R. J., Dickinson, C., Holler, C. M., Irfan, M. O., John, J. J., Leahy, J. P., Leech, J., Muchovej, S. J. C., Pearson, T. J., Stevenson, M. A., and Taylor, A. C. (2014). The C-Band All-Sky Survey (C-BASS): design and implementation of the northern receiver. *Mon. Not. R. Astron. Soc.*, 438:2426–2439.
- Kogut, A. (2012). Synchrotron Spectral Curvature from 22 MHz to 23 GHz. *Astrophys. J.*, 753:110.
- Kogut, A., Dunkley, J., Bennett, C. L., Doré, O., Gold, B., Halpern, M., Hinshaw, G., Jarosik, N., Komatsu, E., Nolte, M. R., Odegard, N., Page, L., Spergel, D. N., Tucker, G. S., Weiland, J. L., Wollack, E., and Wright, E. L. (2007). Three-Year Wilkinson Microwave Anisotropy Probe (WMAP) Observations: Foreground Polarization. *Astrophys. J.*, 665:355–362.
- Krachmalnicoff, N., Baccigalupi, C., Aumont, J., Bersanelli, M., and Mennella, A. (2016). Characterization of foreground emission on degree angular scales for CMB B-mode observations . Thermal dust and synchrotron signal from Planck and WMAP data. *Astron. Astrophys.*, 588:A65.

- Krauss, L. M. and Turner, M. S. (1995). The cosmological constant is back. *General Relativity and Gravitation*, 27:1137–1144.
- Kurki-Suonio, H., Keihänen, E., Keskitalo, R., Poutanen, T., Sirviö, A.-S., Maino, D., and Burigana, C. (2009). Destriping CMB temperature and polarization maps. *Astron. Astrophys.*, 506:1511–1539.
- Lawson, K. D., Mayer, C. J., Osborne, J. L., and Parkinson, M. L. (1987). Variations in the Spectral Index of the Galactic Radio Continuum Emission in the Northern Hemisphere. *Mon. Not. R. Astron. Soc.*, 225:307.
- Leavitt, H. S. and Pickering, E. C. (1912). Periods of 25 Variable Stars in the Small Magellanic Cloud. *Harvard College Observatory Circular*, 173:1–3.
- Leitch, E. M., Kovac, J. M., Halverson, N. W., Carlstrom, J. E., Pryke, C., and Smith, M. W. E. (2005). Degree Angular Scale Interferometer 3 Year Cosmic Microwave Background Polarization Results. *Astrophys. J.*, 624:10–20.
- Leitch, E. M., Readhead, A. C. S., Pearson, T. J., and Myers, S. T. (1997). An Anomalous Component of Galactic Emission. *Astrophys. J. Lett.*, 486:L23–L26.
- Lemaître, G. (1927). Un Univers homogène de masse constante et de rayon croissant rendant compte de la vitesse radiale des nébuleuses extra-galactiques. *Annales de la Société Scientifique de Bruxelles*, 47:49–59.
- Lemaître, G. (1931a). Expansion of the universe, A homogeneous universe of constant mass and increasing radius accounting for the radial velocity of extra-galactic nebulae. *Mon. Not. R. Astron. Soc.*, 91:483–490.
- Lemaître, G. (1931b). The Beginning of the World from the Point of View of Quantum Theory. *Nature.*, 127:706.

- López-Caraballo, C. H., Rubiño-Martín, J. A., Rebolo, R., and Génova-Santos, R. (2011). Constraints on the Polarization of the Anomalous Microwave Emission in the Perseus Molecular Complex from Seven-year WMAP Data. *Astrophys. J.*, 729:25.
- Louis, T., Grace, E., Hasselfield, M., Lungu, M., Maurin, L., Addison, G. E., Ade, P. A. R., Aiola, S., Allison, R., Amiri, M., Angile, E., Battaglia, N., Beall, J. A., de Bernardis, F., Bond, J. R., Britton, J., Calabrese, E., Cho, H.-m., Choi, S. K., Coughlin, K., Crichton, D., Crowley, K., Datta, R., Devlin, M. J., Dicker, S. R., Dunkley, J., Dünner, R., Ferraro, S., Fox, A. E., Gallardo, P., Gralla, M., Halpern, M., Henderson, S., Hill, J. C., Hilton, G. C., Hilton, M., Hincks, A. D., Hlozek, R., Ho, S. P. P., Huang, Z., Hubmayr, J., Huffenberger, K. M., Hughes, J. P., Infante, L., Irwin, K., Muya Kasanda, S., Klein, J., Koopman, B., Kosowsky, A., Li, D., Madhavacheril, M., Marriage, T. A., McMahon, J., Menanteau, F., Moodley, K., Munson, C., Naess, S., Nati, F., Newburgh, L., Nibarger, J., Niemack, M. D., Nolta, M. R., Nuñez, C., Page, L. A., Pappas, C., Partridge, B., Rojas, F., Schaan, E., Schmitt, B. L., Sehgal, N., Sherwin, B. D., Sievers, J., Simon, S., Spergel, D. N., Staggs, S. T., Switzer, E. R., Thornton, R., Trac, H., Treu, J., Tucker, C., Van Engelen, A., Ward, J. T., and Wollack, E. J. (2017). The Atacama Cosmology Telescope: two-season ACTPol spectra and parameters. *Journal of Cosmology and Astroparticle Physics.*, 6:031.
- Macellari, N., Pierpaoli, E., Dickinson, C., and Vaillancourt, J. E. (2011). Galactic foreground contributions to the 5-year Wilkinson Microwave Anisotropy Probe maps. *Mon. Not. R. Astron. Soc.*, 418:888–905.
- MacTavish, C. J., Ade, P. A. R., Battistelli, E. S., Benton, S., Bihary, R., Bock, J. J., Bond, J. R., Brevik, J., Bryan, S., Contaldi, C. R., Crill, B. P., Doré, O., Fissel, L., Golwala, S. R., Halpern, M., Hilton, G., Holmes, W., Hristov, V. V., Irwin, K., Jones, W. C., Kuo, C. L., Lange, A. E., Lawrie, C., Martin, T. G., Mason, P., Montroy, T. E., Netterfield, C. B., Riley, D., Ruhl, J. E., Runyan, M., Trangsrud, A., Tucker, C., Turner, A., Viero, M., and Wiebe, D. (2008). Spider Optimization: Probing the Systematics of a Large-Scale B-Mode Experiment. *Astrophys. J.*, 689:655–665.

- Maino, D., Burigana, C., Maltoni, M., Wandelt, B. D., Górski, K. M., Malaspina, M., Bersanelli, M., Mandolesi, N., Banday, A. J., and Hivon, E. (1999). The Planck-LFI instrument: Analysis of the  $1/f$  noise and implications for the scanning strategy. *Astron. Astrophys. Supp.*, 140:383–391.
- Mason, B. S., Robishaw, T., Heiles, C., Finkbeiner, D., and Dickinson, C. (2009). A Limit on the Polarized Anomalous Microwave Emission of Lynds 1622. *Astrophys. J.*, 697:1187–1193.
- Mortonson, M. J. and Seljak, U. (2014). A joint analysis of Planck and BICEP2 B modes including dust polarization uncertainty. *Journal of Cosmology and Astroparticle Physics.*, 10:035.
- Nguyen, H. T., Kovac, J., Ade, P., Aikin, R., Benton, S., Bock, J., Brevik, J., Carlstrom, J., Dowell, D., Duband, L., Golwala, S., Halpern, M., Hasslefield, M., Irwin, K., Jones, W., Kaufman, J., Keating, B., Kuo, C.-L., Lange, A., Matsumura, T., Netterfield, B., Pryke, C., Ruhl, J., Sheehy, C., and Sudiwala, R. (2008). BICEP2/SPUD: searching for inflation with degree scale polarimetry from the South Pole. In *Millimeter and Submillimeter Detectors and Instrumentation for Astronomy IV*, volume 7020 of , page 70201F.
- North, C. E., Johnson, B. R., Ade, P. A. R., Audley, M. D., Baines, C., Battye, R. A., Brown, M. L., Cabella, P., Calisse, P. G., Challinor, A. D., Duncan, W. D., Ferreira, P. G., Gear, W. K., Glowacka, D., Goldie, D. J., Grimes, P. K., Halpern, M., Haynes, V., Hilton, G. C., Irwin, K. D., Jones, M. E., Lasenby, A. N., Leahy, P. J., Leech, J., Maffei, B., Mauskopf, P., Melhuish, S. J., O’Dea, D., Parsley, S. M., Piccirillo, L., Pisano, G., Reintsema, C. D., Savini, G., Sudiwala, R., Sutton, D., Taylor, A. C., Teleberg, G., Titterington, D., Tsaneva, V., Tucker, C., Watson, R., Withington, S., Yassin, G., and Zhang, J. (2008). Detecting the B-mode Polarisation of the CMB with Clover. *ArXiv e-prints*.
- Oxley, P., Ade, P. A., Baccigalupi, C., deBernardis, P., Cho, H.-M., Devlin, M. J., Hanany, S., Johnson, B. R., Jones, T., Lee, A. T., Matsumura, T., Miller, A. D., Milligan, M., Renbarger, T., Spieler, H. G., Stompor, R., Tucker, G. S., and Zaldarriaga, M. (2004). The EBEX experiment.

- In Strojnik, M., editor, *Infrared Spaceborne Remote Sensing XII*, volume 5543 of , pages 320–331.
- Page, L., Hinshaw, G., Komatsu, E., Nolta, M. R., Spergel, D. N., Bennett, C. L., Barnes, C., Bean, R., Doré, O., Dunkley, J., Halpern, M., Hill, R. S., Jarosik, N., Kogut, A., Limon, M., Meyer, S. S., Odegard, N., Peiris, H. V., Tucker, G. S., Verde, L., Weiland, J. L., Wollack, E., and Wright, E. L. (2007). Three-Year Wilkinson Microwave Anisotropy Probe (WMAP) Observations: Polarization Analysis. *Astrophys. J. Supp.*, 170:335–376.
- Peebles, P. J. E. (1984). Tests of cosmological models constrained by inflation. *Astrophys. J.*, 284:439–444.
- Peebles, P. J. E., Page, Jr., L. A., and Partridge, R. B. (2009). Finding the Big Bang. In *Finding the Big Bang*, by P. James E. Peebles , Lyman A. Page, Jr. , R. Bruce Partridge, Cambridge, UK: Cambridge University Press, 2009.
- Penzias, A. A. and Wilson, R. W. (1965). A Measurement of Excess Antenna Temperature at 4080 Mc/s. *Astrophys. J.*, 142:419–421.
- Perlmutter, S., Turner, M. S., and White, M. (1999). Constraining Dark Energy with Type Ia Supernovae and Large-Scale Structure. *Physical Review Letters*, 83:670–673.
- Planck Collaboration, Adam, R., Ade, P. A. R., Aghanim, N., Akrami, Y., Alves, M. I. R., Argüeso, F., Arnaud, M., Arroja, F., Ashdown, M., and et al. (2016a). Planck 2015 results. I. Overview of products and scientific results. *Astron. Astrophys.*, 594:A1.
- Planck Collaboration, Adam, R., Ade, P. A. R., Aghanim, N., Alves, M. I. R., Arnaud, M., Ashdown, M., Aumont, J., Baccigalupi, C., Banday, A. J., and et al. (2015a). Planck 2015 results. X. Diffuse component separation: Foreground maps. *ArXiv e-prints*.
- Planck Collaboration, Adam, R., Ade, P. A. R., Aghanim, N., Arnaud, M., Aumont, J., Baccigalupi, C., Banday, A. J., Barreiro, R. B., Bartlett, J. G., and et al. (2016b). Planck intermediate results. XXX. The angular power spectrum of polarized dust emission at intermediate and high Galactic latitudes. *Astron. Astrophys.*, 586:A133.

Planck Collaboration, Ade, P. A. R., Aghanim, N., Alina, D., Alves, M. I. R., Armitage-Caplan, C., Arnaud, M., Arzoumanian, D., Ashdown, M., Atrio-Barandela, F., and et al. (2015b). Planck intermediate results. XIX. An overview of the polarized thermal emission from Galactic dust. *Astron. Astrophys.*, 576:A104.

Planck Collaboration, Ade, P. A. R., Aghanim, N., Alves, M. I. R., Arnaud, M., Ashdown, M., Atrio-Barandela, F., Aumont, J., Baccigalupi, C., Banday, A. J., Barreiro, R. B., Bartlett, J. G., Battaner, E., Benabed, K., Benoit-Lévy, A., Bernard, J.-P., Bersanelli, M., Bielewicz, P., Bobin, J., Bonaldi, A., Bond, J. R., Borrill, J., Bouchet, F. R., Boulanger, F., Bucher, M., Burigana, C., Butler, R. C., Cardoso, J.-F., Catalano, A., Chamballu, A., Chiang, H. C., Chiang, L.-Y., Christensen, P. R., Clements, D. L., Colombi, S., Colombo, L. P. L., Couchot, F., Crill, B. P., Curto, A., Cuttaia, F., Danese, L., Davies, R. D., Davis, R. J., de Bernardis, P., de Rosa, A., de Zotti, G., Delabrouille, J., Dickinson, C., Diego, J. M., Dole, H., Donzelli, S., Doré, O., Douspis, M., Dupac, X., Enßlin, T. A., Eriksen, H. K., Falgarone, E., Finelli, F., Forni, O., Frailis, M., Franceschi, E., Galeotta, S., Ganga, K., Ghosh, T., Giard, M., Giardino, G., González-Nuevo, J., Górski, K. M., Gregorio, A., Gruppuso, A., Hansen, F. K., Harrison, D. L., Hernández-Monteagudo, C., Herranz, D., Hildebrandt, S. R., Hivon, E., Holmes, W. A., Hornstrup, A., Hovest, W., Jaffe, A. H., Jones, W. C., Juvela, M., Keihänen, E., Keskitalo, R., Kisner, T. S., Kneissl, R., Knoche, J., Kunz, M., Kurki-Suonio, H., Lagache, G., Lähteenmäki, A., Lamarre, J.-M., Lasenby, A., Laureijs, R. J., Lawrence, C. R., Leonardi, R., Levrier, F., Liguori, M., Lilje, P. B., Linden-Vørnle, M., López-Caniego, M., Macías-Pérez, J. F., Maffei, B., Maino, D., Mandolesi, N., Maris, M., Marshall, D. J., Martin, P. G., Martínez-González, E., Masi, S., Matarrese, S., Mazzotta, P., Melchiorri, A., Mendes, L., Mennella, A., Migliaccio, M., Mitra, S., Miville-Deschênes, M.-A., Moneti, A., Montier, L., Morgante, G., Mortlock, D., Munshi, D., Murphy, J. A., Naselsky, P., Nati, F., Natoli, P., Nørgaard-Nielsen, H. U., Noviello, F., Novikov, D., Novikov, I., Oxborrow, C. A., Pagano, L., Pajot, F., Paladini, R., Paoletti, D., Pasian, F., Patanchon, G., Peel, M., Perdereau, O., Perrotta, F., Piacentini, F., Piat, M., Pierpaoli, E., Pietrobon, D., Plaszczynski, S., Pointecouteau, E., Polenta, G., Ponthieu, N., Popa, L., Pratt, G. W., Prunet, S., Puget, J.-L., Rachen, J. P., Reach, W. T., Rebolo, R., Reinecke,

M., Remazeilles, M., Renault, C., Ricciardi, S., Riller, T., Ristorcelli, I., Rocha, G., Rosset, C., Rubiño-Martín, J. A., Rusholme, B., Sandri, M., Savini, G., Scott, D., Spencer, L. D., Starck, J.-L., Stolyarov, V., Sureau, F., Sutton, D., Suur-Uski, A.-S., Sygnet, J.-F., Tauber, J. A., Tavagnacco, D., Terenzi, L., Toffolatti, L., Tomasi, M., Tristram, M., Tucci, M., Valenziano, L., Valiviita, J., Van Tent, B., Verstraete, L., Vielva, P., Villa, F., Vittorio, N., Wade, L. A., Wandelt, B. D., Yvon, D., Zacchei, A., and Zonca, A. (2014a). Planck intermediate results. XIV. Dust emission at millimetre wavelengths in the Galactic plane. *Astron. Astrophys.*, 564:A45.

Planck Collaboration, Ade, P. A. R., Aghanim, N., Alves, M. I. R., Arnaud, M., Ashdown, M., Aumont, J., Baccigalupi, C., Banday, A. J., Barreiro, R. B., and et al. (2016c). Planck 2015 results. XXV. Diffuse low-frequency Galactic foregrounds. *Astron. Astrophys.*, 594:A25.

Planck Collaboration, Ade, P. A. R., Aghanim, N., Alves, M. I. R., Arnaud, M., Atrio-Barandela, F., Aumont, J., Baccigalupi, C., Banday, A. J., Barreiro, R. B., Battaner, E., Benabed, K., Benoit-Lévy, A., Bernard, J.-P., Bersanelli, M., Bielewicz, P., Bobin, J., Bonaldi, A., Bond, J. R., Borrill, J., Bouchet, F. R., Boulanger, F., Burigana, C., Cardoso, J.-F., Casassus, S., Catalano, A., Chamballu, A., Chen, X., Chiang, H. C., Chiang, L.-Y., Christensen, P. R., Clements, D. L., Colombi, S., Colombo, L. P. L., Couchot, F., Crill, B. P., Cuttaia, F., Danese, L., Davies, R. D., Davis, R. J., de Bernardis, P., de Rosa, A., de Zotti, G., Delabrouille, J., Désert, F.-X., Dickinson, C., Diego, J. M., Donzelli, S., Doré, O., Dupac, X., Enßlin, T. A., Eriksen, H. K., Finelli, F., Forni, O., Franceschi, E., Galeotta, S., Ganga, K., Génova-Santos, R. T., Ghosh, T., Giard, M., González-Nuevo, J., Górski, K. M., Gregorio, A., Gruppuso, A., Hansen, F. K., Harrison, D. L., Helou, G., Hernández-Monteagudo, C., Hildebrandt, S. R., Hivon, E., Hobson, M., Hornstrup, A., Jaffe, A. H., Jaffe, T. R., Jones, W. C., Keihänen, E., Keskitalo, R., Kneissl, R., Knoche, J., Kunz, M., Kurki-Suonio, H., Lähteenmäki, A., Lamarre, J.-M., Lasenby, A., Lawrence, C. R., Leonardi, R., Liguori, M., Lilje, P. B., Linden-Vørnle, M., López-Caniego, M., Macías-Pérez, J. F., Maffei, B., Maino, D., Mandolesi, N., Marshall, D. J., Martin, P. G., Martínez-González, E., Masi, S., Massardi, M., Matarrese, S., Mazzotta, P., Meinhold, P. R., Melchiorri, A., Mendes, L., Mennella, A., Migliaccio, M.,

- Miville-Deschênes, M.-A., Moneti, A., Montier, L., Morgante, G., Mortlock, D., Munshi, D., Naselsky, P., Nati, F., Natoli, P., Nørgaard-Nielsen, H. U., Noviello, F., Novikov, D., Novikov, I., Oxborrow, C. A., Pagano, L., Pajot, F., Paladini, R., Paoletti, D., Patanchon, G., Pearson, T. J., Peel, M., Perdereau, O., Perrotta, F., Piacentini, F., Piat, M., Pierpaoli, E., Pietrobon, D., Plaszczynski, S., Pointecouteau, E., Polenta, G., Ponthieu, N., Popa, L., Pratt, G. W., Prunet, S., Puget, J.-L., Rachen, J. P., Rebolo, R., Reich, W., Reinecke, M., Remazeilles, M., Renault, C., Ricciardi, S., Riller, T., Ristorcelli, I., Rocha, G., Rosset, C., Roudier, G., Rubiño-Martín, J. A., Rusholme, B., Sandri, M., Savini, G., Scott, D., Spencer, L. D., Stolyarov, V., Sutton, D., Suur-Uski, A.-S., Sygnet, J.-F., Tauber, J. A., Tavagnacco, D., Terenzi, L., Tibbs, C. T., Toffolatti, L., Tomasi, M., Tristram, M., Tucci, M., Valenziano, L., Valiviita, J., Van Tent, B., Varis, J., Verstraete, L., Vielva, P., Villa, F., Wandelt, B. D., Watson, R., Wilkinson, A., Ysard, N., Yvon, D., Zacchei, A., and Zonca, A. (2014b). Planck intermediate results. XV. A study of anomalous microwave emission in Galactic clouds. *Astron. Astrophys.*, 565:A103.
- Planck Collaboration, Ade, P. A. R., Aghanim, N., Armitage-Caplan, C., Arnaud, M., Ashdown, M., Atrio-Barandela, F., Aumont, J., Baccigalupi, C., Banday, A. J., and et al. (2014c). Planck 2013 results. XVI. Cosmological parameters. *Astron. Astrophys.*, 571:A16.
- Planck Collaboration, Ade, P. A. R., Aghanim, N., Arnaud, M., Ashdown, M., Aumont, J., Baccigalupi, C., Balbi, A., Banday, A. J., Barreiro, R. B., and et al. (2011). Planck early results. XX. New light on anomalous microwave emission from spinning dust grains. *Astron. Astrophys.*, 536:A20.
- Planck Collaboration, Ade, P. A. R., Aghanim, N., Arnaud, M., Ashdown, M., Aumont, J., Baccigalupi, C., Banday, A. J., Barreiro, R. B., Bartlett, J. G., and et al. (2015c). Planck 2015 results. XIII. Cosmological parameters. *ArXiv e-prints*.
- Planck Collaboration, Ade, P. A. R., Alves, M. I. R., Aniano, G., Armitage-Caplan, C., Arnaud, M., Atrio-Barandela, F., Aumont, J., Baccigalupi, C., Banday, A. J., Barreiro, R. B., Battaner, E., Benabed, K., Benoit-Lévy, A., Bernard, J.-P., Bersanelli, M., Bielewicz, P., Bock, J. J., Bond, J. R., Borrill, J., Bouchet, F. R., Boulanger, F., Burigana, C., Cardoso, J.-F., Catalano,

A., Chamballu, A., Chiang, H. C., Colombo, L. P. L., Combet, C., Couchot, F., Coulais, A., Crill, B. P., Curto, A., Cuttaia, F., Danese, L., Davies, R. D., Davis, R. J., de Bernardis, P., de Zotti, G., Delabrouille, J., Désert, F.-X., Dickinson, C., Diego, J. M., Donzelli, S., Doré, O., Douspis, M., Dunkley, J., Dupac, X., Enßlin, T. A., Eriksen, H. K., Falgarone, E., Finelli, F., Forni, O., Frailis, M., Fraisse, A. A., Franceschi, E., Galeotta, S., Ganga, K., Ghosh, T., Girard, M., González-Nuevo, J., Górski, K. M., Gregorio, A., Gruppuso, A., Guillet, V., Hansen, F. K., Harrison, D. L., Helou, G., Hernández-Monteagudo, C., Hildebrandt, S. R., Hivon, E., Hobson, M., Holmes, W. A., Hornstrup, A., Jaffe, A. H., Jaffe, T. R., Jones, W. C., Keihänen, E., Keskitalo, R., Kisner, T. S., Kneissl, R., Knoche, J., Kunz, M., Kurki-Suonio, H., Lagache, G., Lamarre, J.-M., Lasenby, A., Lawrence, C. R., Leahy, J. P., Leonardi, R., Levrier, F., Liguori, M., Lilje, P. B., Linden-Vørnle, M., López-Caniego, M., Lubin, P. M., Macías-Pérez, J. F., Maffei, B., Magalhães, A. M., Maino, D., Mandolesi, N., Maris, M., Marshall, D. J., Martin, P. G., Martínez-González, E., Masi, S., Matarrese, S., Mazzotta, P., Melchiorri, A., Mendes, L., Mennella, A., Migliaccio, M., Miville-Deschênes, M.-A., Moneti, A., Montier, L., Morgante, G., Mortlock, D., Munshi, D., Murphy, J. A., Naselsky, P., Nati, F., Natoli, P., Netterfield, C. B., Noviello, F., Novikov, D., Novikov, I., Oppermann, N., Oxborrow, C. A., Pagano, L., Pajot, F., Paoletti, D., Pasian, F., Perdereau, O., Perotto, L., Perrotta, F., Piacentini, F., Pietrobon, D., Plaszczynski, S., Pointecouteau, E., Polenta, G., Popa, L., Pratt, G. W., Rachen, J. P., Reach, W. T., Reinecke, M., Remazeilles, M., Renault, C., Ricciardi, S., Riller, T., Ristorcelli, I., Rocha, G., Rosset, C., Roudier, G., Rubiño-Martín, J. A., Rusholme, B., Salerno, E., Sandri, M., Savini, G., Scott, D., Spencer, L. D., Stolyarov, V., Stompor, R., Sudiwala, R., Sutton, D., Suur-Uski, A.-S., Sygnet, J.-F., Tauber, J. A., Terenzi, L., Toffolatti, L., Tomasi, M., Tristram, M., Tucci, M., Valenziano, L., Valiviita, J., Van Tent, B., Vielva, P., Villa, F., Wandelt, B. D., Zacchei, A., and Zonca, A. (2015d). Planck intermediate results. XXII. Frequency dependence of thermal emission from Galactic dust in intensity and polarization. *Astron. Astrophys.*, 576:A107.

Platania, P., Bensadoun, M., Bersanelli, M., De Amici, G., Kogut, A., Levin, S., Maino, D., and Smoot, G. F. (1998). A Determination of the Spectral Index of Galactic Synchrotron Emission

in the 1-10 GHz Range. *Astrophys. J.*, 505:473–483.

Platania, P., Burigana, C., Maino, D., Caserini, E., Bersanelli, M., Cappellini, B., and Mennella, A. (2003). Full sky study of diffuse Galactic emission at decimeter wavelengths. *Astron. Astrophys.*, 410:847–863.

Readhead, A. C. S., Myers, S. T., Pearson, T. J., Sievers, J. L., Mason, B. S., Contaldi, C. R., Bond, J. R., Bustos, R., Altamirano, P., Achermann, C., Bronfman, L., Carlstrom, J. E., Cartwright, J. K., Casassus, S., Dickinson, C., Holzapfel, W. L., Kovac, J. M., Leitch, E. M., May, J., Padin, S., Pogosyan, D., Pospieszalski, M., Pryke, C., Reeves, R., Shepherd, M. C., and Torres, S. (2004). Polarization Observations with the Cosmic Background Imager. *Science*, 306:836–844.

Rees, M. J. (1968). Polarization and Spectrum of the Primeval Radiation in an Anisotropic Universe. *Astrophys. J. Lett.*, 153:L1.

Reich, P. and Reich, W. (1988). A map of spectral indices of the Galactic radio continuum emission between 408 MHz and 1420 MHz for the entire northern sky. *Astron. Astrophys. Supp.*, 74:7–23.

Remazeilles, M., Dickinson, C., Banday, A. J., Bigot-Sazy, M.-A., and Ghosh, T. (2015). An improved source-subtracted and destripped 408-MHz all-sky map. *Mon. Not. R. Astron. Soc.*, 451:4311–4327.

Remazeilles, M., Dickinson, C., Eriksen, H. K. K., and Wehus, I. K. (2016). Sensitivity and foreground modelling for large-scale cosmic microwave background B-mode polarization satellite missions. *Mon. Not. R. Astron. Soc.*, 458:2032–2050.

Riess, A. G., Filippenko, A. V., Challis, P., Clocchiatti, A., Diercks, A., Garnavich, P. M., Gilliland, R. L., Hogan, C. J., Jha, S., Kirshner, R. P., Leibundgut, B., Phillips, M. M., Reiss, D., Schmidt, B. P., Schommer, R. A., Smith, R. C., Spyromilio, J., Stubbs, C., Suntzeff, N. B., and Tonry, J. (1998). Observational Evidence from Supernovae for an Accelerating Universe and a Cosmological Constant. *Astron. J.*, 116:1009–1038.

- Rohlfs, K. and Wilson, T. L. (2004). Tools of radio astronomy. In *Tools of radio astronomy, 4th rev. and enl. ed.*, by K. Rohlfs and T.L. Wilson. Berlin: Springer, 2004.
- Rubiño-Martín, J. A., López-Caraballo, C. H., Génova-Santos, R., and Rebolo, R. (2012). Observations of the Polarisation of the Anomalous Microwave Emission: A Review. *Advances in Astronomy*, 2012:351836.
- Rybicki, G. B. and Lightman, A. P. (1986). Radiative Processes in Astrophysics. In *Radiative Processes in Astrophysics*, by George B. Rybicki, Alan P. Lightman, ISBN 0-471-82759-2. Wiley-VCH, June 1986.
- Sachs, R. K. and Wolfe, A. M. (1967). Perturbations of a Cosmological Model and Angular Variations of the Microwave Background. *Astrophys. J.*, 147:73.
- Schott, G. A. (1912). Electromagnetic radiation and the mechanical reactions arising from it. Cambridge University Press.
- Scott, D. (2006). The standard cosmological model. *Canadian Journal of Physics*, 84:419–435.
- Scott, D. and Smoot, G. F. (2010). Cosmic Microwave Background Mini-review. *ArXiv e-prints*.
- Seljak, U. and Zaldarriaga, M. (1997). Signature of Gravity Waves in the Polarization of the Microwave Background. *Physical Review Letters*, 78:2054–2057.
- Silk, J. (1968). Cosmic Black-Body Radiation and Galaxy Formation. *Astrophys. J.*, 151:459.
- Smoot, G., Bennett, C., Weber, R., Maruschak, J., Ratliff, R., Janssen, M., Chitwood, J., Hilliard, L., Lecha, M., Mills, R., Patschke, R., Richards, C., Backus, C., Mather, J., Hauser, M., Weiss, R., Wilkinson, D., Gulkis, S., Boggess, N., Cheng, E., Kelsall, T., Lubin, P., Meyer, S., Moseley, H., Murdock, T., Shafer, R., Silverberg, R., and Wright, E. (1990). COBE Differential Microwave Radiometers - Instrument design and implementation. *Astrophys. J.*, 360:685–695.
- Smoot, G. F. (1998). Galactic Free-free and H-alpha Emission. *ArXiv Astrophysics e-prints*.

- Smoot, G. F., Bennett, C. L., Kogut, A., Wright, E. L., Aymon, J., Boggess, N. W., Cheng, E. S., de Amici, G., Gulkis, S., Hauser, M. G., Hinshaw, G., Jackson, P. D., Janssen, M., Kaita, E., Kelsall, T., Keegstra, P., Lineweaver, C., Loewenstein, K., Lubin, P., Mather, J., Meyer, S. S., Moseley, S. H., Murdock, T., Rokke, L., Silverberg, R. F., Tenorio, L., Weiss, R., and Wilkinson, D. T. (1992). Structure in the COBE differential microwave radiometer first-year maps. *Astrophys. J. Lett.*, 396:L1–L5.
- Staniszewski, Z., Aikin, R. W., Amiri, M., Benton, S. J., Bischoff, C., Bock, J. J., Bonetti, J. A., Brevik, J. A., Burger, B., Dowell, C. D., Duband, L., Filippini, J. P., Golwala, S. R., Halpern, M., Hasselfield, M., Hilton, G., Hristov, V. V., Irwin, K., Kovac, J. M., Kuo, C. L., Lueker, M., Montroy, T., Nguyen, H. T., Ogburn, R. W., O’Brien, R., Orlando, A., Pryke, C., Reintsema, C., Ruhl, J. E., Schwarz, R., Sheehy, C., Stokes, S., Thompson, K. L., Teply, G., Tolán, J. E., Turner, A. D., Vieregg, A. G., Wilson, P., Wiebe, D., and Wong, C. L. (2012). The Keck Array: A Multi Camera CMB Polarimeter at the South Pole. *Journal of Low Temperature Physics*, 167:827–833.
- Stompor, R., Balbi, A., Borrill, J. D., Ferreira, P. G., Hanany, S., Jaffe, A. H., Lee, A. T., Oh, S., Rabbii, B., Richards, P. L., Smoot, G. F., Winant, C. D., and Wu, J.-H. P. (2002). Making maps of the cosmic microwave background: The MAXIMA example. *Physical Review D*, 65(2):022003.
- Sunyaev, R. A. and Zeldovich, Y. B. (1970). Small-Scale Fluctuations of Relic Radiation. *Astrophys. Space Sci.*, 7:3–19.
- Sutton, D., Johnson, B. R., Brown, M. L., Cabella, P., Ferreira, P. G., and Smith, K. M. (2009). Map making in small field modulated CMB polarization experiments: approximating the maximum likelihood method. *Mon. Not. R. Astron. Soc.*, 393:894–910.
- Sutton, D., Zuntz, J. A., Ferreira, P. G., Brown, M. L., Eriksen, H. K., Johnson, B. R., Kusaka, A., Naess, S. K., and Wehus, I. K. (2010). Fast and precise map-making for massively multi-detector CMB experiments. *Mon. Not. R. Astron. Soc.*, 407:1387–1402.

- Szapudi, I., Prunet, S., Pogosyan, D., Szalay, A. S., and Bond, J. R. (2001). Fast Cosmic Microwave Background Analyses via Correlation Functions. *Astrophys. J. Lett.*, 548:L115–L118.
- Taylor, A. R., Stil, J. M., and Sunstrum, C. (2009). A Rotation Measure Image of the Sky. *Astrophys. J.*, 702:1230–1236.
- Tegmark, M. (1997). How to Make Maps from Cosmic Microwave Background Data without Losing Information. *Astrophys. J. Lett.*, 480:L87–L90.
- Testori, J. C., Reich, P., and Reich, W. (2008). A fully sampled  $\lambda 21$  cm linear polarization survey of the southern sky. *Astron. Astrophys.*, 484:733–742.
- Tinbergen, J. (1996). Astronomical Polarimetry. In *Astronomical Polarimetry*, by Jaap Tinbergen, ISBN 0521475317. Cambridge, UK: Cambridge University Press, September 1996.
- Vidal, M., Dickinson, C., Davies, R. D., and Leahy, J. P. (2015). Polarized radio filaments outside the Galactic plane. *Mon. Not. R. Astron. Soc.*, 452:656–675.
- Vittorio, N. and Silk, J. (1985). Can a relic cosmological constant reconcile inflationary predictions with the observations? *Astrophys. J. Lett.*, 297:L1–L4.
- Watson, R. A., Rebolo, R., Rubiño-Martín, J. A., Hildebrandt, S., Gutiérrez, C. M., Fernández-Cerezo, S., Hoyland, R. J., and Battistelli, E. S. (2005). Detection of Anomalous Microwave Emission in the Perseus Molecular Cloud with the COSMOSOMAS Experiment. *Astrophys. J. Lett.*, 624:L89–L92.
- White, M., Scott, D., and Silk, J. (1994). Anisotropies in the Cosmic Microwave Background. *Annu. Rev. Astron. Astrophys.*, 32:319–370.
- Wolleben, M., Landecker, T. L., Reich, W., and Wielebinski, R. (2006). An absolutely calibrated survey of polarized emission from the northern sky at 1.4 GHz. Observations and data reduction. *Astron. Astrophys.*, 448:411–424.
- Wright, E. L., Hinshaw, G., and Bennett, C. L. (1996). Producing Megapixel Cosmic Microwave Background from Differential Radiometer Data. *Astrophys. J. Lett.*, 458:L53.

Zel'dovich, Y. B., Kurt, V. G., and Syunyaev, R. A. (1969). Recombination of Hydrogen in the Hot Model of the Universe. *Soviet Journal of Experimental and Theoretical Physics*, 28:146.